THREE DIMENSIONAL POLYMER SCAFFOLDS FOR HIGH THROUGHPUT CELL-BASED ASSAY SYSTEMS

by

KE CHENG

(Under the Direction of William Kisaalita)

ABSTRACT

This study has been carried out to better understand how cells behave in three dimensional polymer scaffolds for cell-based assay applications. Many whole cell-based assays in use today rely on flat, two-dimensional (2D) glass or plastic substrates that may not produce results characteristic of in vivo conditions. Ideal cell-based screening systems call for research efforts to create simple, robust and effective 3D cell-based platforms so that cellular responses will be more representative of those under *in vivo* conditions. Although 3-D cell culture systems are known to reflect the in vivo behavior of many cell types and are promising approaches for advanced drug screening, providing an appropriate environment in which to culture cells in three dimensions is no easy matter. A major reason that the 3-D culture systems have not entered the drug screening process to date is the lack of simple, controlled techniques and protocols for rapid, standardized 3-D cell-based assay systems.

The overall objective of this study is to design a more physiologically relevant cell-based assay system by integrating cells with synthetic polymer scaffolds. A technology was invented to

integrate 3D synthetic polymer scaffolds with standard cell culture vessels. This technology can be used to feasibly modify any traditional 2D cell-based assay vessels for 3D cell-based assay with currently used high throughput screening (HTS) systems. Extensive research has been conducted to compare cellular activities on polymer scaffolds (3-D), flat surfaces (2-D) and in vivo surrogates. To best mimic the natural extracellular matrix, nano-structures have been brought into the previous scaffold topography to form a nano-fibrous and micro-porous combination scaffolds.

Results obtained from this study supports conclusion that cells cultured on 3D scaffolds more closely emulates in-vivo surrogates such as fresh dissected tissue and neural spheres, in comparison to the cells on flat (2-D) controls. This new biomimetic cell-based assay platform may provide a broadly applicable 3D cell-based system for use in drug discovery programs and other research fields. Future studies could demonstrate the potential of this 3-D cell-based assay system in improving clinical efficacy and drug safety prediction in early stages of drug discovery programs.

INDEX WORDS: Polymer scaffolds, Cell-based assay, High throughput drug discovery, 3D Cell culture, Tissue engineering

THREE DIMENSIONAL POLYMER SCAFFOLDS FOR HIGH THROUGHPUT

CELL-BASED ASSAY SYSTEMS

by

Ke Cheng

B.S., Zhejiang University, China, 2004

A Dissertation Submitted to Graduate Faculty of The University of Georgia Presented in Partial

Fulfillment of the Requirements for the Degree

DOCTOR OF PHILOSOPHY

ATHENS, GEORGIA

2008

THREE DIMENSIONAL POLYMER SCAFFOLDS FOR HIGH THROUGHPUT

CELL-BASED ASSAY SYSTEMS

by

KE CHENG

Major Professor: William Kisaalita

Committee: Charles Keith
            Steve Stice
            Guigen Zhang

Electronic Version Approved:

Maureen Grasso
Dean of the Graduate School
The University of Georgia
August, 2008

DEDICATION

Dedicated to my parents, Baozhong Cheng & Qihua Zhou, and my wife, Dongmei Zhu for their love.

ACKNOWLEDGMENTS

The journey of pursuing a Ph.D. degree in the US is such an adventure which has not only trained me as a young researcher but also profoundly shaped my personality. My appreciation will go to all the persons who helped me during this process. My deepest appreciation goes to my advisor, Dr. William Kisaalita. I would like to thank him for his advice and timeless support of my researches and all other aspects of my life. His research mindsets as well as his attitude toward professionalism have influenced me a lot during my stay here, and will continue to influence me for the rest of my life.

I also would like to extend my sincere appreciation to my dissertation committee: Dr. Charles Keith, Dr. Steve Stice, and Dr. Guigen Zhang, for their insightful advice and tremendous support of my work. I appreciate their time, patience and help during this long process.

I thank the University of Georgia and the Department of Biological and Agricultural Engineering for admitting me as a doctoral student and providing me financial support. UGA is such a great place providing a wonderful atmosphere for academic accomplishments.

I would like to thank all my colleagues for their friendship. I thank Dr. Zezhi Wu for training me and helping me after I joined the Cellular Bioengineering Laboratory. I appreciate Ms. Yinzhi Lai, Ms. Lina Wang, Mr. Yanbin Guan, Mr. Rahul Singh, and Mr. Adam Sutherland for their insightful ideas on my researches and generous contribution to my experiments.

My thanks also go to Dr. John Shields, Ms. Kowser Hasneen, Dr. Dave Machacek, Ms. Liz Stitch for their technical assistance. I thank all departmental staff: Ms. Patsy Adams, Ms. Ellen King, Ms. Sherry Wrona, Ms. Kristin Brink, Ms. Pat James, Mr. Jarrod Buffington, and Mr. Pat Harrell for their friendly presence and help.

Last but not least, I am grateful to my family members, especially my wife Dongmei Zhu and my parents Mr. Baozhong Cheng and Ms. Qihua Zhou, for their solid support and belief in me throughout this process.

Finishing the Ph.D. program is just the beginning of a new journey, a life time journey. With the knowledge, experience, friendship and trust I got from here, I am ready for the challenge and opportunities in my career and professional life.

TABLE OF CONTENTS

CHAPTER 1

INTRODUCTION

1.1 Cell-based assays and HTS

Over the past few years, there has been a growing trend towards more frequent use of cell-based assays for drug discovery. Cell-based assays refer to any of a number of different assay experiments based on the use of live cells. This defines the assays that measure cell viability, proliferation, differentiation, motility, production of a measurable product, morphology, functionality and so on.

Cell-based assays are versatile assays and have certain advantages over conventional biochemical assays [1, 2]. Biochemical assays usually test compounds for activity against isolated proteins and ligands, searching for effects like enzyme inhibition or binding. However, the "hit" compounds from such a screen or assay ultimately have to function in the complex system of cells and tissues. Thus, a cell-based assay can be a good compromise between pure in vitro systems and whole organisms. Cell lines are relatively easy to handle compared to animal models. Because the cell is a highly regulated system, cell-based assays usually give robust and reproducible signals. Cell-based assays are enabled by advances in methods of cellular signal

detection. Many of the most popular and useful read-outs involve the use of fluorescent or bioluminescent probes or proteins to report the cellular activities.

Cell-based assay usage and spending have been growing alongside the use of high-throughput screening (HTS). In terms of definition, HTS can be considered the process in which batches of compounds are tested for binding or biological activity against target molecules. Over the past decade, HTS has become a cornerstone technology of pharmaceutical research. Investments in HTS have been, and continue to grow. A current estimate is that biological screening and preclinical pharmacological testing alone account for ~14% of the total research and development (R&D) expenditures of the pharmaceutical industry [3, 4].

Globally, the total cell-based assay market reached a figure of around $475 million in 2004. The global total cell-based assays market is expected to be valued at greater than $1.2 billion by 2011 [5]. The discovery and implementation of entirely new classes and types of potential drug targets in many drug discovery operations are driving much of the cell-based work; however, it should be acknowledged that cellular screening presents a variety of challenges.

1.2 ECM and physiological relevance of 3-D cell culture

It is well known that in the body cells are in contact not only with each other, but also with surrounding structure called the extracellular matrix (ECM). Figure 1.1 shows a cell embedded in a 3-D natural scaffold. ECM contains proteins, such as collagen, elastin and laminin that give

tissues their mechanical/topographical cues and help to organize communication between cells embedded within the matrix. Receptors on the surface of the cells, in particular a family of integrins, anchor their bearers to the ECM, and also determine how the cells interpret biochemical and topographical cues from their immediate surroundings. Given this complex mechanical and biochemical interplay, it is perhaps no surprise that researchers will miss biological information if the cells they are studying grow only in flat layers or so-called two dimensional (2-D) cultures [6].

This lack of predictability of commonly employed 2-D cellular assays is attributable to the fact that such systems do not mimic the response of cells in the 3-D microenvironment and the ECM present in vivo [7]. Currently, influential players in both industry and academia are already thinking along 3-D cell cultures and they predicted that "in 10 years, anyone trying to use 2-D analyses to get relevant and novel biological information will find it difficult to get funded." [7]. If 3-D culture can provide a better model for what happens in the body, it might allow researchers to accelerate drug discovery and reduce their use of experimental animals. The potential importance of 3-D cell cultures in the process of drug discovery is illustrated in Figure 1.2.

1.3 Synthetic polymer scaffolds

One influential 3-D cell culture method in use today is creating artificial ECMs to mimic the cellular microenvironments in vivo. Attempts have been made to culture cells in 3-D by using

porous or fibrous polymer scaffolds made from synthetic polymers and their copolymers. The main application of synthetic scaffold research so far has been either drug delivery or tissue engineering [8]. Synthetic polymer scaffolds for 3-D cell growth have included poly (lactid), poly(ethylene oxide), poly(vinyl alcohol), poly(acrylic acid), poly(propylene furmarate-co-ethylene glycol) or poly (styrene) [9]. The scaffold is a 3-D substrate for cells, and serves as a template for tissue regeneration. The rationale for use of synthetic polymer scaffolds as substrates for 3-D cell-based assay lies in the fact that these scaffolds provide cells with characteristic topographical cues and thus enable cells to differentiate into specific phenotypes and form multi-cellular aggregates that are usually impossible under 2-D cell culture conditions.

1.4 Research objectives

For economic and ethical reasons, cell-based assay systems that mimic the *in vivo* environment with increasing accuracy will soon need to be considered to optimize preclinical screening of "hits"from the large and growing pool of drug candidates [10]. Efforts to establish and optimize new systems for advanced 3-D cell-based in vitro screening are necessary and should be encouraged. Although 3-D cell culture systems are known to reflect the in vivo behavior of many cell types and are promising approaches for advanced drug screening, providing an appropriate environment in which to culture cells in three dimensions is no easy matter. A major reason that the 3-D culture systems have not entered the drug screening process

to date is the lack of simple, controlled techniques and protocols for rapid, standardized 3-D cell-based assay systems.

To address this need, the following specific objectives were pursued in this study:

1. To create a high throughput cell-based assay system by using synthetic polymer scaffolds as a 3-D cell culture format and to characterize the physical properties of the scaffolds, as well as the cellular activities cultured within.

2. To study the physiological relevance of the polymer scaffold as a 3-D cell culture model and cell-based assay format by comparing the cellular activities from polymer scaffolds and flat surfaces to these from in vivo surrogates.

3. To optimize the structure of polymer scaffolds to best mimic the morphology of natural ECM by introducing nano-textures into the traditional micro-porous polymer scaffolds.

1.5 Scope of study

In Chapter 3, a 3-D cell-based assay platform was established by integrating 3-D synthetic polymer scaffolds with standard cell culture dishes and multi-well plates. This technology can be used to feasibly modify any traditional 2-D cell-based assay vessels for 3-D cell-based assay with currently used high throughput screening (HTS) systems. We examined neural stem (NS) cells' growth profile, morphology, cell-matrix interaction, gene expression and calcium channel functionality of this novel 3-D assay platform. The results showed that unlike the NS cells cultured on traditional 2-D planar surfaces, cells in 3-D scaffolds are more

physiologically relevant with respect to in vivo characteristics exhibited by in-vivo surrogates (neural spheres). This new biomimetic cell-based assay platform may provide a broadly applicable 3-D cell-based system for use in drug discovery programs and other research fields.

In Chapter 4, we investigated how well mouse sympathetic neuronal cells in vitro model in vivo functionality with respect to voltage gated calcium channels (VGCC). VGCC were chosen because they are emerging drug targets — there is a link between diseases of the nervous and cardiovascular systems and channel dysfunction. Mouse superior cervical ganglion (SCG) cells were harvested and cultured on the 3-D scaffolds made from poly-l-lactic-acid (PLLA) and 2-D glass substrates, both coated with collagen. We found that the cell morphology and VGCC function from cells on 3-D scaffolds more closely modeled intact SCG tissues in comparison to cells on 2-D cover slips. Intracellular calcium increase in response to high potassium depolarization was identical between 3-D cultured and intact SCG tissue cells, but significantly different between 3-D and 2-D cultured cells. This result provides evidence in support of the hypothesis that some cellular responses under traditional 2-D environment may be exaggerated.

In Chapter 5, to best mimic the architecture of the natural extracellular matrix (ECM), a nano-fibrous/micro-porous combination (NFMP) scaffold was fabricated using phase separation and particulate leaching technique. The resulting scaffolds exhibited architectural features at two levels, including the micro-scale pores (60-300 microns) and nano-scale fibers (around 500 nm). To evaluate the unique advantages of NFMP scaffold in 3-D cell culture and tissue engineering, micro-pore and nano-fiber scaffolds were also fabricated. Human neural stem cells and fibroblast cells were seeded into these three types of scaffolds. The results indicated that the NFMP

scaffold inherited advantages from the other two scaffolds and was indeed superior to both of them. The NFMP scaffolds were able to accommodate a large cell population, promote cell differentiation, and induce a more "3-D" morphogenesis and cell-matrix adhesion. To the best of our knowledge, this is the first study to systematically compare the effects of micro, nano and micro/nano combination scaffolds on cellular behaviors.

1.6 References

1. Bousse L. Whole cell biosensors. Sensors and Actuators. 1996;34:270-275.

2. Durick K, Negulescu P. Cellular biosensors for drug discovery. Biosensors and Bioelectronics. 2001;16:587-592.

3. Handen JS. High-throughput screening — challenges for the future. Drug Discovery World. 2002;47–50.

4. Bajorath J. Integration of virtual and high-throughput screening. Nature Reviews Drug Discovery. 2002;**1**:882-894.

5. Source: http://www.frost.com accessed on June 20, 2008

6. Abbott A. Biology's new dimension. Nature. 2003;424:870–872.

7. Bhadriraju K, Chen CS. Engineering cellular microenvironments to improve cell-based drug testing. Drug Discovery Today. 2002;7(11):612-620.

8. Langer R, Vacanti JP. Tissue engineering. Science.1993;260:920-926.

9. Lozinsky VI, Plieva FM. Poly(vinyl alcohol) cryogels employed as matrices for cell immobilization. 3. Overview of recent research and developments. Enzyme and Microbial Technology. 1998;23:227-242.

10. Kunz-Schughart LA, Kreutz M, Knuechel R. Multicellular spheroids: a three-dimensional in vitro culture system to study tumor biology. International Journal of Experimental Pathology. 1998;79:1-23.
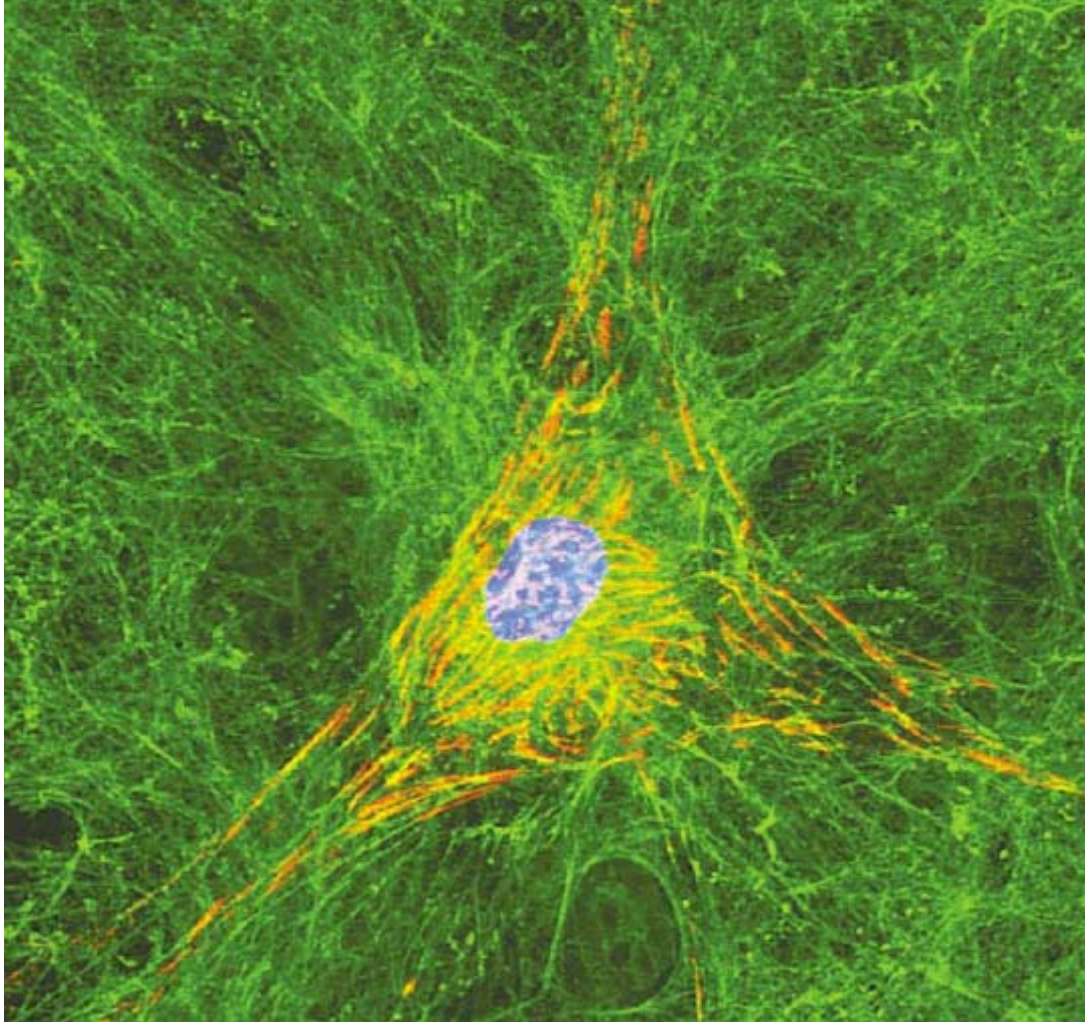
Figure 1.1: A cell in a 3-D culture forming links by means of beta-integrin (orange) with the ECM scaffolding [7].
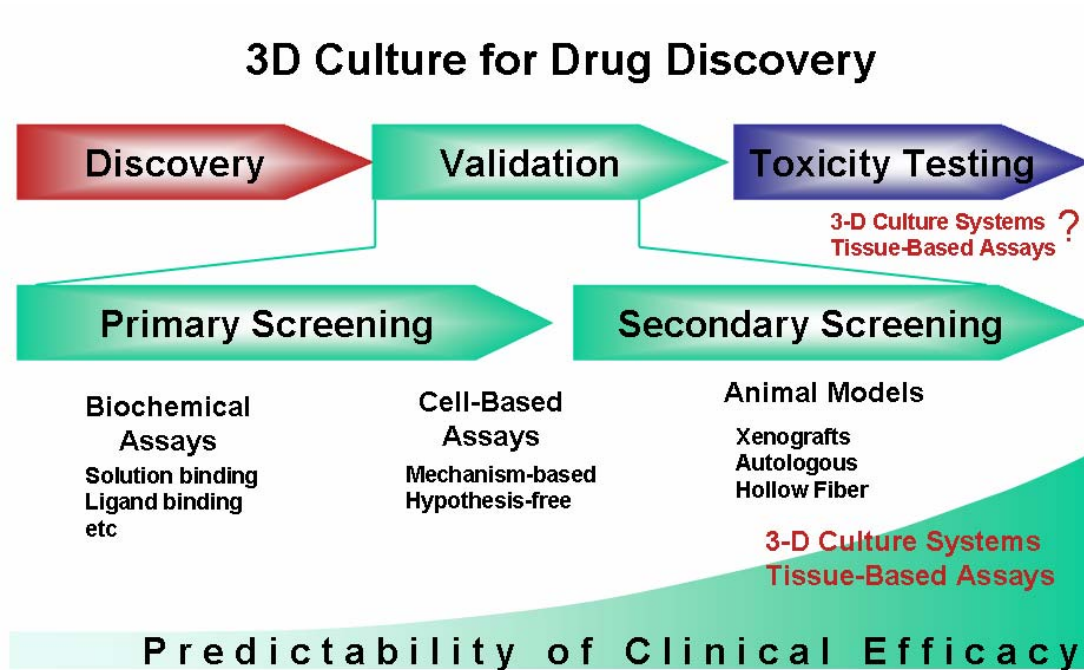
Figure 1.2. Potential values of 3-D cell culture in the drug discovery process.

CHAPTER 2

LITERATURE REVIEW

2.1 ECM and physiological relevance of 3D cell culture

2.1.1 Introduction

Extracellular matrix (ECM) is a group of proteins and polysaccharides that encapsulate the cells. ECM includes the interstitial matrix and the basement membrane [1]. They mediate the cellular functionalities and signal transduction. Collagen, hyaluronic acid, alginate, and chitosan are the commonly used natural polymers in cell culture application. Collagen is the main protein of ECM in animal connective tissues and makes up about 25% of the total protein content in mammals. The research in ECM began in 1966 when it was first discovered that ECM provided a structural support for cells. Later, it was confirmed that the ECM mediated all the signal transduction form the cell exterior to the cytoplasm regions of the cells.

2.1.2 Functions of extracellular matrix

The extracellular matrix (ECM) is composed of a 3-D scaffold of collagen, fibronectin (FN), and other proteins, interlaced with proteoglycans. Their functions are summarized in Table 2.1. These proteins form a very complex network and were found to be receptors of various growth

factors and enzymes. Different cells have different compositions of ECM and will adapt to the

change in environment by changing the composition of their ECM. The organization of ECM

also varies according to different cell types. ECM composition and organization are critical to

the overall cellular functionality *in vivo*. The ECM promotes signaling and provides structural

support to the cells and tissues of the body. It also serves as a reservoir for growth factors,

cytokines, enzymes, and other diffusible molecules.

2.1.3 Cell-matrix interactions

It is well known that the matrix to which the cells are attaching are critical to cell adhesion,

proliferation, differentiation and other consequential cellular behaviors. ECM interacts with cells

through a group of integrins on the cell membrane. At least three major classes of ECM factors

affect cellular behavior (Figure 2.1). They are: the biochemical composition of the ECM (e.g. its

content of collagen versus other molecules), physical parameters of the matrix particularly its

pliability, spatial cues (e.g. its three dimensionality, nano-scale structures). Each of these classes

of ECM factors can affect cellular activities such as migration [2], proliferation [3], or

differentiation [4]. For example, the presence of a certain peptide sequence on surfaces increases

cell attachment [5]. Matrix mechanical properties such as elastic modulus influence cell activities

such as proliferation. Cells grown on soft surfaces were shown to be different from those grown

on hard surfaces [6, 7]. Spatial cures are also shown to fundamentally affect cellular behaviors

both *in vivo* and *in vitro*. Currently, nano-scale structures have been widely applied by biologists

and bioengineers to direct cell morphology, proliferation, differentiation, and other cellular

functionalities [8].Understanding the biology behind the cell-ECM interaction is critical to

understanding how cells function in a cell-based drug testing.

2.1.4 Physiological relevance of 3-D culture

2-D cell-based drug testing early in discovery has been practiced by many pharmaceutical

and biotech labs since the early 90's. In the oncology area, screens for either a general effect,

such as cytotoxicity, or a specific molecular target, such as mitogen-activated protein (MAP)

kinase, have resulted in poor chances of therapeutic success when such screens ignored the

signaling cellular microenvironments of the assay [9]. The fact that cell-based screens give

different results than later *in vivo* responses suggests that the pathways regulating proliferation

and apoptosis are different in different cellular contexts. In another instance, *in vitro* absorption

assays of Caco-2 cells have not faithfully predicted *in vivo* bioavailability [10], partly because

these cultures exhibit significant differences from the *in vivo* normal intestine phenotype in

protein expression and cell morphology. In addition, it is well-known that even genetically

normal primary cells placed in flat (2-D) cell culture quickly lose their differentiated gene

expression pattern and phenotype [11].

Due the lack of physiological relevance of traditional cell culture, more and more

biologists have turned to 3-D cell culture for potential answers. Weaver et al. [12] showed that

beta1-integrin antibodies completely changed the behavior of cancerous breast cells grown in

3-D culture to become non-cancerous, losing their abnormal shapes and patterns of growth. This result had never been observed in traditional 2-D cultures. The same group has also demonstrated further important differences in the behavior of cells grown in 2-D and 3-D cultures. In the same breast-cancer system, they have shown that beta1-integrin antibodies also decrease signaling by receptors for epidermal growth factor (EGF); antibodies against EGF receptors similarly depress the activity of beta1-integrin.Again, this reciprocal interaction does not happen in 2-D cultures [13]. Wolf et al. [14] transplanted metastasizing cells into mice and used imaging techniques to track their development. They underwent the same amoeba-like morphological changes seen in 3-D cultures abut not seen in 2-D cultures. Anders et al. [15] reported that in 2-D cultures both normal and malignant breast cells had similar high levels of the receptors. But in 3-D cultures, only malignant cells carried large numbers of the receptors.

Cukierman et al. [16] directly compared the growth and development of fibroblasts, collagen-secreting cells that are found in many tissues, in 2-D and 3-D cultures. In three dimensions, the cells moved and divided more quickly, and assumed the characteristic asymmetric shape that fibroblasts have in living tissues.

Moreover, some researchers are now trying to make systematic comparisons of gene activity in 2-D and 3-D cultures. In unpublished work, Dr. Linda Griffith's group at MIT is using DNA microarrays to look at profiles of gene expression in liver cells. Their preliminary analysis shows that the expression profile in 3-D is much closer to in vivo expression profiles than the profile observed in 2-D. In another unpublished work, Dr. William Kisaalita's group at the University of Georgia is utilizing whole genome microarrays to systematically compare the gene

expression of neuronal cells on 2-D, 3-D and in vivo surrogate. They are in search of "3-D bio-markers". Although the physiological relevance of 3-D cell culture is widely known, the direct comparison of 2-D and 3-D cellular functionality to that from an *in vivo* surrogate will be very desirable to investigate the importance of 3-D cell culture in drug screening.

2.2 3-D cell culture

2.2.1 Introduction

The history of cell culture started in 1885 when Wilhelm Roux removed a portion of the medullary plate of an embryonic chicken and maintained it in a warm saline solution for several days, establishing the basic principle of tissue culture. In 1907 the zoologist Ross Granville Harrison demonstrated the growth of frog nerve cell processes in a medium of clotted lymph, establishing the methodology of tissue culture. This probably marked as the first establishment of 3-D culture *in vitro*. Conventional three dimensional cell culture systems were systematically developed in the 1970's for prolonged and large scale biosynthesis such as monoclonal antibody production [17-19]. The potential promise of 3-D cell culture models has led to publications for either new 3-D cell culture systems or for means to overcome limitations in existing formats. Moreover, various influential players in the biotech industry have developed and marketed their 3-D cell culture products (Table 2.2).

There are two general classes of *in vitro* 3D cell culture supporting architecture systems: 1) 3-D architecture resulting primarily from fabricated material physical form (scaffolds) and 2)

3-D architecture resulting primarily from cellular-self organization in response to the imposed biochemical and/or fluid mechanical forces. In the first category, scaffolds have been fabricated from natural [20, 21] and synthetic [22] polymers, or as nano/micro patterned structures [23]. In the second category, cell culture media has been formulated [24] and microgravity environment has been used [25-27] to support cellular spheroid and tissue formation, respectively. Figure 2.2 illustrates different 3-D cell culture formats.

Obviously, each of the above-mentioned approaches to 3-D culture *in vitro* has its pros and cons making each suitable for some applications. For instance, natural polymer hydrogels have very good optical properties making them ideal for optical detection methods. However, due to its low mechanical strength, natural polymer hydrogels are unsuitable for applications that require load bearing. To select a proper cell culture format for 3-D cell-based assay for drug discovery, several aspects need to be taken into consideration. First, the 3-D cell culture should have high physiological relevance to the in vivo environments; second, it should have certain mechanical and optical properties; third, it should be easily scalable for incorporation into HTS drug discovery systems in use today. In the following sections, different types of 3-D cell culture formats are introduced separately.

2.2.2 Microgravity bioreactor

Approximation of micro-gravitational conditions at ground level has been achieved in specialized cell culture systems using a rotating-wall vessel (RWV) bioreactors developed at

NASA's Johnson Space Center [28-31]. The scientists designed a horizontally-disposed cylinder with end caps which can rotate about an approximate horizontal axis. The vessels are designed to approximate the extremely quiescent low shear environment obtainable in space where it would be unnecessary for a lifting mechanism to oppose particle sedimentation. Scientists hypothesized that the gentle culture environment will allow cells to achieve and maintain a three dimensional orientation according to cellular derived forces, and thus form higher order tissue structures (aggregates). The possibility of creating three-dimensional differentiated tissue-like assemblies by culturing cells in microgravity, either in space or on the ground, offers research opportunities that may lead to the generation of replacement organs for transplantation, and for studying multicellular responses in toxicology, radiation biology, tumorigenesis, and embryogenesis. Successful growth and differentiation of 3D cellular aggregates RWV has been observed in colon cancer cell cultures [32], ovarian tumor cells [33], skeletal tissue [34], salivary gland cell culture [33], and neuroblastoma cells. Unfortunately, the preparation of this kind of 3D cell culture is extremely time consuming and is not amenable to scaling-down for HTS applications in drug discovery.

2.2.3 Multicellular spheroid

Multicellular spheroids (MCS) as a 3D cellular construct have been widely used in biomedical research since the early decades of 20th century. Holtfreter [35] and later Moscona [36] pioneered the field by their systematic research on morphogenesis using spherical

re-aggregated cultures of embryonic or malignant cells. Later, Sutherland [37] and Kaaijk [38] inaugurated multicellular tumor spheroids (MCTS) as an *in vitro* model for systematic studies on tumor cell response to therapy. A systematical review can be found in [39]. As a consequence, therapeutically-oriented studies became the major domain of research with cell spheroids, although such investigations also triggered a number of studies on basic biological mechanisms such as the regulation of proliferation, differentiation, cell death, invasion, angiogenesis and immune response [40-42]. The major advantage of 3D MCS cultures is their well-defined geometry which makes it possible to directly relate structure to function and enables theoretical analyses, e.g., of diffusion fields. Consequently, the most promising data on these cultures may be obtained with techniques allowing for spatial resolution. Combining such approaches with molecular and genomic analysis has clearly demonstrated that, in comparison with conventional 2-D cultures, cells in 3-D cultures more closely resemble the *in vivo* situation with regard to cell shape and cellular environment, and shape and environment can determine gene expression and the biological behavior of the cells. However, similar to the microgravity bioreactor, the preparation of MCSs with controlled sizes are time consuming and not easy to scale-down for 3-D cell-based assay applications in current HTS platforms. In addition, due to the gradient diffusion, there is huge difference between cells located in the core of the MCSs and those at the periphery.

2.2.4 Natural polymer scaffolds

Naturally derived polymers such as collagen and hyaluronic acid have been frequently used in 3D cell culture applications because of their similarity to natural ECM with respect to composition and topographical properties. Collagen is the main protein of ECM in animal connective tissues and makes up about 25% of the total protein content in mammals. It has been applied as scaffolds to study cell growth, proliferation, differentiation as well as cell function in a 3D environment [25, 43-45]. Gelatin, derived from partial hydrolysis of collagen, is another naturally derived polymer for cell culture systems [46]. Usala [47, 48] introduced a matrix comprising of a mixture of gelatin and an effective amount of polar amino acids selected from arginine, lysine, histidine, glutamic acid, and aspartic acid. Apparently, this matrix is able to sustain cells and complex clusters of cells such as islets. Hydrophilic polysaccharides such as chitosan, hyaluronic acid and alginate are also used as 3D matrices for cell culture [49-53]. For example, in Tsuzuki [54], a water-containing gel of chitosan carrier for cell culture was reported. The sugar chain of hyaluronic acid or alginate has a specific recognition for cells. Based on this, Goto [55] proposed hyaluronic acid and alginate as well as their derivatives as biocompatible and degradable 3D matrix for cell culture. When the cells are incubated using hyaluronic acid or alginate or their derivatives, it is possible to maintain and improve the proliferation, morphology and function of the cells and to retain the cells in an *in vivo*-like form due to a specific interaction between the cell and the sugar chain.

Although the composition of these natural polymers are similar to the ECM *in vivo*, as

scaffolds for cell culture *in vitro* they are not as reproducible and versatile as synthetic polymers,

especially in controlling pore formation and mechanical properties to meet the need for

cell-based biosensor and tissue engineering applications. Another major limitation of natural

polymer scaffolds such as collagen hydrogel is mass transport. The stiffness of hydrogel

seriously restricts nutrients, dye and wastes to be transported into and out of the cells. As a

matter of fact, to stain the cells entrapped in the collagen hydrogel, one might use a dye

concentration 60 times as higher as the normal working concentration [21].

2.2.5 Micro- and nano-patterned structures

Powers et al. [56, 57] described a 3-D scaffold created by deep reactive ion etching of

silicon wafers to create an array of channels with cell-adhesive walls and revealed significantly

greater functional activity and morphological stability in comparison to 2-D primary rat liver cell

cultures. The effect of different patterned microstructures such as hexagonal microstructure and

micropillar arrays on the neurite outgrowth have been successfully conducted by a group headed

by Drs. Craighead and Turner [58-60]. Hockberger et al. [61] found that, by morphologically or

chemically introducing regular microstructured patterns on the substrate, the cell-substrate

interaction can be manipulated. In addition, other guided cell growth and cell-surface interaction

on microstructured patterns have been intensively studied [62-65]. Culturing nerve cells on

nanostructured substrates has not presented any problems; Mattson et al. [66] have successfully

cultured neurons on carbon nanotubes. The fabrication of high aspect ratio microstructures is a

standard technique for micro-electrical-mechanical systems (MEMS) [67]. However, the major

problem of this 3-D cell culture format is its physiological relevance. Even with a high aspect

ratio, micro- and nano-patterned structures are not usually considered as 3-D cell cultures but

surface-modified structures.

2.2.6 Synthetic polymer scaffolds

Synthetic polymers exhibit wide ranges of properties and can be tailored to specific

applications with different features (e.g. shapes, porosities and pore sizes, rates of degradation,

mechanical properties). Unlike natural polymers, whose properties may vary from batch to batch,

synthetic polymers can be controlled to maintain the same required property. Because of their

versatility and reproducibility, synthetic polymers are some of the most widely used materials for

3-D scaffolds. Desirable properties include: 1) biocompatibility both in bulk and degraded form

if degradable, 2) mechanical strength, 3) amenable to form porous or fibrous matrices,

and 3) exhibit appropriate surface properties for cell adhesion. For cell-based assay applications,

light transmission is important for compatibility with optical detection devices used in

conventional High Throughput Screening (HTS) systems. Polymers frequently used include

polylactic acid (PLA), polyglycolic acid (PGA), poly (lactide-co-glycolide acid) (PLGA)

copolymers, poly (a-hydroxy acid), polydioxanone, poly(ethylene terephthalate) (PET) and

polystyrene. PGA, PLA, polydioxanone, and copolymers have been approved by U.S. Food and

Drug Administration (FDA) and have been in use for over 20 years in clinical applications [68]. Besides the bulk chemical and physical properties of synthetic polymers, the micro- and macrostructure play a crucial role in forming a 3D environment that mimics *in* vivo systems. Porous scaffolds or fibrous matrix are the most frequent encountered structures for synthetic polymers in the 3D cell culture field. When compared to other materials, synthetic polymers or composites have better controllable mechanical and structural properties, thus a numbers of investigators have utilized them as the basis of the 3D cell cultures. The rationale for use of synthetic polymer scaffolds as substrates for 3-D cell-based assay lies in the fact that these scaffolds provide cells with characteristic topographical cues and thus enable cells to differentiate into specific phenotypes and form multi-cellular aggregates that are usually impossible under 2-D cell culture conditions.

In comparison to other 3-D cell culture formats, synthetic polymer scaffolds offer several comparative advantages. First, in comparison to microgravity bioreactors and patterned substrates, polymer scaffolds are easier and faster to prepare and can be scaled down for incorporation into HTS systems. Second, in comparison to most hydrogels, polymer scaffolds offer less resistance to diffusion of nutrients and wastes to and from cells deeper into the scaffold. Third, in comparison to nano-scale pores and fibers associated with self-assembling peptide scaffolds, micro-scale pores on polymer scaffolds are large enough to host multi-cellular organisms which are observed in tissue engineering studies [69].

Although the advantages of polymer scaffolds as a 3-D cell culture format is clear, the difficulty in incorporating them with current HTS cell-based assay platforms (e.g. 96-well or

384-well plates) has prevented them from being widely used in bio/pharmaceutical laboratories. The industry is calling for a feasible and robust technology to incorporate polymer scaffolds with the current assay platforms.

2.3 Three dimensional synthetic polymer scaffolds

2.3.1 Fabrication of micro-porous polymer scaffolds

Porous scaffolds or fibrous matrix are the most frequent encountered structures for synthetic polymers in the 3D cell culture field. The most common techniques used to create porous biomaterial include phase separation [70, 71], emulsion freeze drying [72-74], gas foaming [75-77], fiber bonding [78, 79], particulate (i.e. salt) leaching [80, 81], sintering [82, 83], and 3-D printing [84] depending on the material to be used to fabricate the scaffolds. The comparison of these methods can be found in a review by Rezwan et al. [85]. Investigators have found that porosity, pore size, pore geometry, pore branching, pore connectivity and pore orientation can affect the function or behavior of cells grown in the 3D cell culture system [86]. Thus, one of the research focuses on 3D cell culture system is on developing new techniques to better control those parameters economically. Table 2.4 exemplifies methods for producing three-dimensional scaffolds. Different fabrication methods yielded different matrix and pore structures (Figure 2.3).

2.3.2 Scaffolds with nano- and micro- structures

The scaffolding foundations of an engineered tissue should possess similar dimensions as the natural ECM [87]. It has been suggested that the nano-fibrous architecture and the high surface-to-volume ratio provided by nano-scale fibers could improve cell adhesion, which consequently affects cell migration, proliferation, and differentiation [88, 89]. On a micro-scale, it has been suggested that pore shape, size, and interconnectivity between pores are important for cell seeding, mass transport, and 3-D tissue formation [90, 91].

Various studies have taken place to create nano and micro combination scaffolds and to study the cell-matrix interactions on these scaffolds. Dr. Ma's group at University of Michigan pioneered this field. They reported a 3-D micro-porous architectures built in the nano-fibrous matrices which is fabricated by a technique that combines phase-separation and particulate leaching [92-94] (Figure 2.4). Recently, Pham et al. [95] reported a multilayer of nano/microfiber scaffold by using a multiple layers of electrospun PCL on top micro-scaffolds. Another approach was conducted by combining electrospinning method with particulate leaching method [96]. Correa-Duarte et al. [97] demonstrated a very unique method to produce wells consisting of aligned carbon nano-tubes, with pore sizes ranging from 5 to 65 μm. In most of these studies, extensive scaffold morphology and mechanical properties have been characterized. However, the benefits of nano and micro combination scaffolds have not yet been systematically investigated. A study to demonstrate the unique advantages of nano and micro combination scaffolds will benefit tissue engineering as well as 3-D cell culture research.

2.4 Nano-structures

2.4.1 Introduction

Nanotechnology is being heralded as a new technological revolution, one so profound that it may touch all aspects of scientific research, including tissue engineering and cell-based assay. With the rationale to mimic the *in vivo* milieu of the cells [98], the topography of ECM was extensively studied and demonstrated to profoundly affect cellular behaviors [92]. As discussed in previous sections, ECM provides cells with biological, mechanical, and spatial "cues". As a very important spatial characteristic, natural ECM is made of nano-scale fibers and pores. To mimic the topography of natural ECM, various types of synthetic nano-topographies were fabricated and used to increase the cell affinity to the surface [99]. It is believed that surface roughness will affect cellular activities as high surface energy on tips of rough surfaces can adsorb proteins faster. Numerous studies have shown that surface topography profoundly affected cellular functions [100] and morphology [101].

Nowadays, most cell-based assays are conducted in Petri dishes or multi-well plates, which are 2-D flat surfaces. Moreover, for most tissue engineering scaffolds in use today, the pore walls are still considered smooth surfaces which do not emulate the topography of natural ECM. The current *in vitro* cell-based assay and tissue engineering, which lack the topographical features on nano-scales, often could not recreate the features and functionalities of the cells *in*

vivo. Thus, the best way to perform *in vitro* studies of cell-based assay and tissue engineering is growing the cells on a surface similar to the natural ECM topography.

2.4.2 Fabrication of nano-structures

Nano-structures can be obtained from either a synthetic or a natural material. Although a natural-derived material can be an ideal substrate to mimic the *in vivo* environment of the cells, synthetic polymers are preferred due to their stability, ease of fabrication, uniformity and the wide range of their properties.

Several methods can be used to fabricate synthetic nano-structures such as: electrospinning [102], phase separation [103], self-assembly [110], photo-immobilization [104], electron beam irradiated polymer grafting [105], and particulate leaching [92]. Each method has its own advantages and disadvantages [106] (Table 2.4 [107]). Micrographs of some nano-structured surfaces produced by several methods are illustrated in Figure 2.5.

Electrospinning is a method that uses an electrical charge to form nano-fibers. Electrospinning can be used to produce fiber structures which are similar to the features of natural ECM. Various types of synthetic polymers can be electrospun to nanofibers. In addition, some natural polymers, such as collagen, can also be electrospun into nanofibers [108]. The major disadvantages of electrospun nano-fibers include: relatively low porosity, weak mechanical properties, and lack of 3-D space for cells to migrate in. These drawbacks limit the applications of electrospun nano-fibers in tissue engineering and 3-D cell culture research.

Particulate leaching method requires the addition of porogen particles, such as sodium chloride or sugar. In particulate leaching, porogens are added to polymer solutions. The solution is then cast into a mold and evaporated to remove the organic solvent. The porogen containing-polymer is then immersed in water to dissolve (leach) the porogens. Due to the sizes of porogen, this method usually yields scaffolds with micro-scale pores.

Molecular self-assembly is another popular technology. Unlike other methods, it is a "bottom-up" fabrication method. Self-assembly is a natural process that occurs in many biological processes, such as protein and nucleic acid syntheses. Using the same principle, surfaces can also be tailored to possess certain moieties or features. This natural-driven orientation of molecules on surfaces will create controlled nano-sized patterns on surfaces [109]. However, the limitation of polymer types that undergo self-assembly restricted its applications in tissue engineering and 3-D cell culture.

In phase-separation technique, polymers are dissolved into organic solvent. Porous material is obtained by cooling down for gel formation. Then the organic solvent is substituted by another solvent. Phase separation usually yields nano-fibrous structures with fiber size ranging from 100 nm to 500 nm.

Phase-separation technique is relatively easy to handle. Most of synthetic polymers can be fabricated into nano-fibrous structures with this method. In addition, the combination of phase separation and particulate leaching can generate synthetic polymer scaffold structures with both nano-fibrous surface and a 3-D space for cell to migrate in.

2.4.3 Nano-structures' effects on cellular behaviors

The mechanisms on how nano-fibers or nano-topographical surfaces affect the cells were not yet fully understood. Table 2.5 illustrates some examples of the effects of nano-fibers on cell culture. The effects of nano-structures on cell behaviors can be categorized into cell morphology, attachment, cell-matrix adhesions, differentiation, proliferation and other cellular activities (e.g. ECM production).

Nano-topographies were shown to profoundly affect cell morphology. Ellis-Behnke et al. [110] reported that a designed self-assembling peptide nano-fiber scaffold creates a permissive environment for axons to regenerate through the site of an acute injury and to knit the brain tissue together. Yang et al. [103, 111] reported that aligned nano-fibers highly supported the mouse NS cell culture and improved the neurite outgrowth compared to the micro-fibers. Similar findings reported by Moxon et al. [112] showed increased extension of neurites from pheochromocytoma cells on nano-porous silicon surfaces compared to smooth silicon surfaces. While most of the references report that nano-structure promotes neural differentiation, Haq et al. [139] reported that by both morphological and biochemical criteria, nano-structured substrates inhibit PC12 differentiation and micro-structured substrates enhance it. This phenomenon might due to the functional nano-molecules the authors used to coat the structures. The authors coated poly-lysine on both nano and micro-structures thus the "micro-structure" was indeed a combination of micro and nano structures. Dalby et al. [113] reported that fibroblasts exhibited much smaller spread area and more circular body on an internal nano-topography than the traditional 3D micro-tube

structure controls. The cells on nano-topography revealed a smaller cell area and are more rounded/circular with stellate cell morphology.

Nano-topographies were shown to affect cytoskeleton aliment and cell-matrix interactions as well. It has been shown that whilst fibroblast cells on the planar controls have many stress fibers, and hence are flat, cells on the nano-columns have fewer stress fibers, and are thus less spread and more rounded [113]. A similar finding showed that cells in micro-structures had clearly defined actin fibers, with prominent stress fibers, and tubulin fibers radiating out for the centre of the cell, as opposed to the cells on nano-structures which exhibited poor actin organization. Recently, Schindler et al. [8] found the fibroblasts on a synthetic nano-fiber scaffolds (UltraWeb[TM]) exhibited punctuate patterns of focal adhesion kinase rather than a well-defined streaky pattern typically exhibited on flat controls. In another similar finding, Berry et al. [114] reported that the fibroblasts cultured in a nano-tube structure exhibited punctuate actin throughout the cell body, while cells in the micro-tube controls exhibit dash-shaped adhesions throughout the cell, reflecting their well spread morphology compared to the small adhesions and smaller sized morphology on nano-tubes.

Nano-topographies were also shown to affect cell activities/functionalities. The amount of ECM produced by cells grown on polyurethane nano-fibers was found to be different compared to flat controls [115]. At the intracellular level, the interaction of cellular cytoskeleton with the surface also can influence the signal transduction within the cell [116]. In addition, scientist have reported that interaction of the cell with nanostructures led to slower cell growth rate as the cell immobilization was increased [117, 118].

Efforts to study the effects of nanofibers on the differentiation of stem cells into specialized cells also have been reported. In one study, the scientists found that growing cells in 3-D nano-fibrous scaffolds supported the adipogenic, chondrogenic, and osteogenic differentiation of human mesenchymal stem cells [119]. In addition, the alignment of cells were found to promote change in cell functioning and differentiation [120]. In studies conducted by our lab and other groups, neural stem (NS) cells were shown to differentiate into neurons on polymer scaffolds with nano-texture on the surface [111].

2.5 Superior cervical ganglion (SCG) cells

In this study, sympathetic neurons from CD1 mice superior cervical ganglion (SCG) were used.The SCG, the largest of the cervical ganglia, is placed opposite the second and third cervical vertebræ. It contains neurons that supply sympathetic innervations to the face. It is of a reddish-gray color, and usually fusiform in shape; sometimes broad and flattened, and occasionally constricted at intervals; it is believed to be formed by the coalescence of four ganglia, corresponding to the upper four cervical nerves. The superior cervical ganglion lies anterior to the sheath of the internal carotid artery and internal jugular vein, and posterior to the Longus capitis muscle. It receives input from the ciliospinal center. Figure 2.6 illustrates the position of SCG in the nervous system.

The CD1 mouse strain was chosen because this strain has been extensively used in toxicological and functional studies as an acceptable model for human medicine applications. These sympathetic neurons arise from the neural crest. They are easily dissected and provide homogeneous cultures in vitro (Banker and Goslin et al., 1998). Figure 2.7 illustrates a group of CD1 mouse SCG cells cultured on 2-D collagen surface. Due to these advantages, sympathetic neurons have been used as robust systems for the study of neuronal development and physiology [121-125]. Most importantly, expression of functional voltage dependent L-type, N-type, P-type, P/Q-type, R-type, and T-type Ca^{2+} channels has been reported [123-125]. Use of SCG cells is necessary because these cells provide a model system with which 2-D, 3-D-in-vitro and 3-D-in-vivo cultures can be evaluated to conclusively determine if 3-D-in-vitro models intact tissue (in vivo) more closely than the 2-D cell cultures. However, beyond this utility, SCG cells are impractical in drug discovery programs because of ethical (animal source) and economic concerns.

2.6 Neural stem (NS) cells

The term "neural stem cell" is used loosely to describe cells that (1) can generate neural tissue or are derived from the nervous system, (2) have some capacity for self-renewal, and (3) can give rise to cells other than themselves through asymmetric cell division [126]. Whether stem cells from neural and other tissues are more defined by their tissue of origin or by their

multi-potentiality is at present unclear. Figure 2.8 illustrates the classes of mammalian stem cells that can give rise to neurons, presented as a hierarchy. The human neural stem cell line used in this study is H945RB.3. It was isolated and developed in Dr. Steve Stice's lab at the Regenerative Bioscience Center of University of Georgia [127] and also available as ENStem-A^{TM} from Millipore (Billerica, MA). Figure 2.9 illustrates human neural stem cells culture on flat surface. The derivation of neural progenitor cells from human embryonic stem (ES) cells is of value both in the study of early human neurogenesis and in the creation of an unlimited source of donor cells for neural transplantation therapy. Neural progenitors are the precursors of the three neural lineages—astrocytes, oligodendrocytes, and mature neurons. Unlike SCG cells, the potential of self-renew capability make neural stem a unlimited cell source for cell-based assay applications. Neural progenitor cells provide a renewable source of cells with the capacity to differentiate into electrically active neurons that could be utilized in a cell-based assay. Most importantly, maintaining neural precursor cells in a proliferative state in culture does not appear to corrupt their natural ability to respond to environmental signals [128, 129] potentially increasing the utility of these cells for cell-based assay applications.

2.7 Voltage gated calcium channel (VGCC) assays

2.7.1 Introduction

Voltage gated calcium channels (VGCCs) play a critical role in shaping the electrical activity of neuronal and muscle cells. VGCCs are popular drug targets because they are

physiologically important and pharmacologically accessible [130, 131]. VGCCs have been defined using electrophysiological, pharmacological and molecular techniques [132] (Table 2.6). A summary of VGCC types and disease targets for their blockers or activators (e.g. hypertension, pain, stroke, Alzheimer's) have been published [133, 134].

The elements in a common VGCC are presented in Figure 2.10. Generally, the channels are trans-membrane proteins with an ion-selective aqueous pore (α_1 subunit) that, when open, extends across the membrane. Channel opening and closing (gating) is controlled by a voltage sensitive region of the protein containing charged amino acids that move within the electric field. The movement of these charged groups leads to conformational changes in the channel resulting in conducting (open/activated) or non-conducting (closed/inactivated) states. These ion channel states provide unique opportunities for drug discovery, enabling drug molecules to be developed that only bind to non-conducting channels. The desired outcome in drug discovery is to find compounds that target tissues exhibiting abnormal electrical activity, while leaving normal channels in active tissue unaffected.

2.7.2 Techniques for VGCC assays

Emerging cell-based ion-channel assay technologies in 96-well plates have been reviewed by Xu et al. [135]. The main automated recording VGCC measurement methods include fluorescence/radiotracer or patch clamping measurement.

Cell-based fluorescence assays is one of the most popular VGCC assay methods in use in today's pharmaceutical industry. The rationale is that VGCC function may be monitored through the measurement of changes in intracellular concentration of calcium ions by using fluorescent indicators or radio-labeled ions. These cell-based assays can be conducted as 96-well formats. In these assays, ion channels are generally activated using compounds that promote prolonged channel opening such as high K^+ depolarization. Fluorescence readout is widely used for Ca^{2+} channels, as influx of Ca^{2+} through open channels causes large transient changes in intracellular Ca^{2+} levels that can be detected using a range of commercially available fluorescent Ca^{2+} dyes such as Fluo-4, Fluo-3 and Calcium Green-AM (Molecular Probes, Eugene, OR, USA). The measurement of rapid kinetic changes in fluorescence for HTS purposes has recently become possible with the availability of a fluorescence plate reader equipped with integral 96-well pipettes, such as a FLIPR® or Flexstation® system (Molecular Devices, Sunnyvale, CA, USA). Figure 2.11 shows assay scheme and Figure 2.12 shows the kinetic data.

As another powerful VGCC assay technology, electrophysiological voltage-clamping techniques encompass the most powerful approach for detailed biophysical analysis of ion-channel function through measurement of current flowing through one or many ion channels. Patch clamping uses a single microelectrode for controlling the membrane voltage whilst measuring the current flow through a single cell or membrane patch (Figure 2.13). However, compared to fluorescence assay, patch clamping has not yet evolved into a high-throughput process for compound screening. Further automation of the patch clamping process would further improve throughput capacities.

2.7.3 HTS instrumentation of VGCC assays

In a HTS program, cell-based assays are usually used as primary or secondary assays to determine functionality of compounds. As cell-based assays are typically more labor intensive, screening of around one sample cellular assay is in an equivalent time-frame to four biochemical assays. However, cell-based assays are information rich and therefore potentially offer greater rewards to scientists. On-going developments in cell-based assay automation and compatibility with multi-well plates are expected to increase the throughput of cellular assays to match the speed of biochemical assays.

In most of the cell-based assay facilities today, the HTS operation is based on integrated robotic systems that handle assays in 96-well and 384-well plates. The challenges for VGCC screening using this type of automation are the design of robot-compatible assays and integration of readers like FlexStation® into these robotic systems. Once achieved, full automation will enable 24×7 continuous operation and allowing assays to be performed more efficiently and economically. For example, the calcium channel assay will be automated for screening in-house using the Beckman (Fullerton, CA, USA) Biomek NX^p plus side-loader fully integrated to Beckman DTX fluorescence plate reader. This approach will significantly increase the throughput of the assay, while reducing the degree of practical work involved.

2.8 References

1.   Kumar, Abbas, Fausto. Robbins and Cotran: Pathologic Basis of Disease; Elsevier; 7th edition (2004).

2.   Palecek SP, Loftus JC, Ginsberg MH, Lauffenburger DA, Horwitz AF. Integrin -ligand binding prosperities govern cell migration speed through cell-substratum adhesiveness. Nature.1997;385:537-540.

3.   Chen CS, Mrksich M, Huang S, Whitesides GM, Ingber DE. Geometric control of cell life and death. Science 1997;276:1425-1428.

4.   Dike LE, Chen CS, Mrksich M, Tien J, Whitesides GM, Ingber DE. Geometric control of switching between growth, apoptosis and differentiation during angiogenesis using micropatterned substrates. In vitro Cell Dev. Bio. Anim. 1999;35:441-448.

5.   Bourdon MA Rouslahti E. Tenascin mediates cell attachment through an RGD dependent receptor. Journal of Cell Biology. 1989;108:1149-1155.

6.   Pelham RJ, Wang Y. Cell locomotion and focal adhesions are regulated by substrate flexibility. PNAS. 1997;94:13661-13665.

7.   Discher DE, Janmey P, Wang Y-L. Tissue cells feel and respond to the stiffness of their substrate. Science. 2005;310:1139-1143.

8.   Schindler M, Ahmed I, Kamal J, Nur-E-Kamal A, Grafe TH, Chung HY, Meiners S. A synthetic nanofibrillar matrix promotes in vivo-like organization and morphogenesis for cells in culture. Biomaterials. 2005;26:5624–5631

9.   Balis FM. Evolution of anticancer drug discovery and the role of cell-based screening. Journal National Cancer Institute. 2002;94:78–79.

10.   Stenberg P, Luthman K, Artursson P. Virtual screening of intestinal drug permeability. Journal of Control Release. 2002;65:231–243.

11.   Mooney DJ, Hansen L, Vacanti J, Langer R, Farmer S, Ingber DE. Switching from differentiation to growth in hepatocytes: control by extracellular matrix. Journal of Cellular Physiology. 1992;151:497–505.

12.   Weaver VM, Petersen OW, Wang F, Larabell CA, Briand P, Damsky C, Bissell MJ. Reversion of the malignant phenotype of human breast cells in three-dimensional culture and in vivo by integrin blocking antibodies. Journal of Cell Biology.1997;137:231-245.

13.   Wang F, Weaver VM, Peterson OM, Larabell CA, Dedhar S, Briand P, Lupu R, Bissell MJ. Reciprocal interactions between b1-integrin and epidermal growth factor receptor in three-dimensional basement membrane breast cultures: A different perspective in epithelial biology. PNAS. 1998;95:14821–14826.

14.   Wolf K, Mazo I, Leung H, Engelke K, von Andrian UH, Deryugina EI, Strongin AY, Bröcker EB, Friedl P. Compensation mechanism in tumor cell migration : mesenchymal–amoeboid transition after blocking of pericellular proteolysis. Journal of Cell Biology. 2003;160:267–277.

15.   Anders M, Hansen R, Ding RX, Rauen KA, Bissell MJ, Korn WM. Disruption of 3D tissue integrity facilitates adenovirus infection by deregulating the coxsackie virus and adenovirus receptor. PNAS. 2003;100:1943–1948.

16.   Cukierman E, Pankov R, Stevens DR, Yamada KM. Taking cell-matrix adhesions to the third dimension. Science. 2001;294:1708-383.

17.   Marinkovich MP, Rocha V. Collagen synthesis and deposition during mammary epithelial cell spreading on collagen gels. Journal of Cellular Physiology. 1986; 128(1): 61-70.

18.   McGrath MF. A novel system for mammary epithelial cell culture. Journal of Dairy Sciences. 1987; 70(9): 1967-1980.

19.   Vournakis JN, Runstadler PW Jr. Optimization of the microenvironment for mammalian cell culture in flexible collagen microspheres in a fluidized-bed bioreactor. Biotechnology. 1991;17: 305-326

20.   Sweeney TM, Kibbey MC, Zain M, Fridman R, and Kleinman HK. Basement membrane and the SIKVAV laminin-derived peptide promote tumor growth and metastases. Cancer Metastasis Review. 1991; 10(3): 245-254.

21.   Mao C and Kisaalita WS. Characterization of 3-D collagen hydrogels for functional cell-based biosensing. Biosensor and Bioelectronics. 2004; 19(9): 1075-1088.

22.   Willerth SM, Arendas KJ, Gottlieb DI, and Sakiyama-Elbert SE. Optimization of fibrin scaffolds for differentiation of murine embryonic stem cells into neural lineage cells. Biomaterials. 2006;27(36):5990-6003.

23.   Wu ZZ, Zhao, YP, Kisaalita WS. Interfacing SH-SY5Y human neuroblastoma cells with SU-8 microstructures. Colloids and Surfaces B: Biointerfaces.2006;52:14–21.

24.   Widera D, Mikenberg I, Kaus A, Kaltschmidt C, and Kaltschmidt B. Nuclear

Factor-kappaB controls the reaggregation of 3D neurosphere cultures in vitro. European Cells

and Materials. 2006; 11: 76-84.

25.   Lin HJ, O'Shaughnessy TJ, Kelly J, and Ma W. Neural stem cell differentiation in a

cell-collagen-bioreactor culture system. Developmental Brain Researches. 2004; 153(2):

163-173.

26.   Griffith L. Microfabricated bioreactors for 3D liver culture. 2002. Atlanta, GA, United

States: Smith and Nephew - GIT, United States.

27.   Wen Y and Yang S-T. Building a tissue engineered microfluidic bioreactor array for

high-throughput assays. 2005. Cincinnati, OH, United States: American Institute of Chemical

Engineers, New York, NY 10016-5991, United States.

28.   Schwarz RP,Wolf DA. US Patent No. 4988623 (1991).

29.   Schwarz RP, Wolf DA, Trinh TT. US Patent No.5153133 (1992).

30.   Wolf DA, Shwarz RP, Lewis ML, Cross JH, Huls MH. US Patent No.5155034 (1992).

31.   Schwarz RP, Wolf DA. US Patent No.5155035 (1992).

32.   Jessup JM, Goodwin TJ, and Spaulding G. Prospects for use of microgravity-based

bioreactors to study three-dimensional host tumor interactions in human neoplasia. Journal of

Cell Biochemistry. 1993;51(3): 290-300.

33.   Becker JL, Prewett TL, Spaulding GF, and Goodwin TJ. Three dimensional growth and

differentiation of ovarian tumor cell line in high aspect rotating-wall vessel: morphologic and

embryologic considerations. Journal of Cell Biochemistry. 1993; 51(3): 283-289.

34.   Freed LE, Langer R, Martin I, Pellis NR, Vunjak-Novakovic G. Tissue engineering of cartilage in space. PNAS. 1997; 94(25): 13885-13890.

35.   Holtfreter J. A study of the mechanism of gastrulation. Journal of Experimental Zoology. 1944; 95:171-212.

36.   Moscona A. Cell suspensions from organ rudiments of chick embryos. Experimental Cell Researches. 1952;3:535-539.

37.   Sutherland RM. Cell and environment interactions in tumor microregions: the multicell spheroid model. Science 1988; 240(4849): 177-184.

38.   Kaaijk P, Troost D, Dast PK, van den Berg F, Leenstra S, Bosch DA. Cytolytic effects of autologous lymphokine-activated killer cells on organotypic multicellular spheroids of gliomas in vitro. Neuropathology and applied neurobiology. 1995;21(5):392-398.

39.   Kunz-Schughart LA, Kreutz M, Knuechel R. Multicellular spheroids: a three-dimensional in vitro culture system to study tumor biology. International Journal of Experimental Pathology. 1998;79:1-23.

40.   Bjerkvig R. Spheroid Culture in Cancer Research, in CRC. 1992: Boca Raton, FL.

41.   Knuechel R, Sutherland. RM. Recent developments in research with human tumor spheroids. Cancer Journal. 1990; 3: 234-243.

42.   Mueller-Klieser W. Multicellular spheroids: A review on cellular aggregates in cancer research. Journal Cancer Research and Clinical Oncology. 1987; 113(2): 101-122.

43. O'Connor SM, Stenger DA, Shaffer KM, Maric D, Barker JL, Ma W. Primary neural precursor cell expansion, differentiation and cytosolic Ca2+ response in three-dimensional collagen gel. Journal of Neuroscience Methods. 2000; 102(2): 187-195.

44. Ma W, Fitzgerald W, Liu QY. CNS stem and progenitor cell differentiation into functional neuronal circuits in three dimensional collagen gels. Experimental Neurology. 2004; 190(2): 276-288.

45. Desai A, Kisaalita WS, Keith C, Wu ZZ. Human neuroblastoma (SH-SY5Y) cell culture and differentiation in 3-D collagen hydrogels for cell-based biosensing. Biosensors and Bioelectronics. 2006; 21(8): 1483-1492.

46. Schagemann JC, Mrosek EH, Landers R, Kurz H, Erggelet C. Morphology and function of ovine articular cartilage chondrocytes in 3-D hydrogel culture. Cells Tissues Organs. 2006; 182(2): 89-97.

47. Usala AL, Klann RC. US Patent No.20016231881 (2001).

48. Usala AL, Klann RC. US Patent No.20046730315 (2004).

49. Girotto D, Urbani S, Brun P, Renier D, Barbucci R, Abatangelo G. Tissue-specific gene expression in chondrocytes grown on three-dimensional hyaluronic acid scaffolds. Biomaterials 2003; 24(19): 3265-3275.

50. Delong L, Sheng M, Wei Z. Immobilization of biomacromolecules on poly-L-lactide surface via a layer-by-layer method for the improving of its cytocompatibility to bone marrow stromal cells. Chinese Science Bulletin. 2005; 50(24): 2809-2816

51.	Dhiman HK, Ray AR, Panda AK. Three-dimensional chitosan scaffold-based MCF-7 cell culture for the determination of the cytotoxicity of tamoxifen. Biomaterials. 2005; 26(9): 979-986.

52.	Yamane S, Iwasaki N, Majima T. Feasibility of chitosanbased hyaluronic acid hybrid biomaterial for a novel scaffold in cartilage tissue engineering. Biomaterials 2005; 26(6): 611-619.

53.	Seo SJ, Choi YJ, Akaike T, Higuchi A, Cho CS. Alginate/galactosylated chitosan/heparin scaffold as a new synthetic extracellular matrix for hepatocytes. Tissue Engineering. 2006; 12(1): 33-44.

54.	Tsuzuki H, Toda S, Kato M. US Patent No.20067022523 (2006).

55.	Goto M, Akaike T, Yang J. US Patent No.20036642050 (2003).

56.	Powers MJ, Domansky K, Kaazempur-Mofrad MR, Kalezi A, Capitano A, Upadhyaya A, Kurzawski P, Wack KE, Beer Stolz D, Kamm R, Griffith LG. A microfabricated array bioreactor for perfused 3D liver culture. Biotechnology and Bioengineering. 2002;78(3):257-269.

57.	Powers MJ, Janigian DM, Wack KE, Baker CS, Beer Stolz D, Griffith LG. Functional behavior of primary rat liver cells in a three-dimensional perfused microarray bioreactor. Tissue Engineering. 8(3):499-513.

58.	Dowell N, Turner AMP, Hong H, Rajan S, Craighead HG, Turner JN, Shain W. Role of microfabricated structures on attachment and growth of neurons and astrocytes. Molecular Biology of the Cell. 2000;11:2831.

59.   Kam L, Shain W, Turner JN, Bizios R. Correlation of astroglial cell function on micro-patterned surfaces with specific geometric parameters. Biomaterials. 1999;20:2343-2350.

60.   Turner AMP, Dowell N, Turner SWP, Kam L, Isaacson M, Turner JN, Craighead HG, Shain W. Attachment of astroglial cells to microfabricated pillar arrays of different geometries. Journal of Biomedical Materials Research. 2000;51:430-441.

61.   Hockberger PE, Lom B, Soekarno CH, Healy K. Cellular engineering: control of cell-substrate interactions. In Nanofabrication and Biosystems: integrating materials science, engineering, and biology. Cambridge University Press, New York. (1996)

62.   Hoch HC, Jelinski LW, Craighead GC. Nanofabrication and Biosystems: integrating materials science, engineering, and biology. Cambridge University Press, New York. (1996)

63.   Mrksich M. Tailored substrates for studies of attached cell culture. CMLS Cellular and Molecular Life Sciences. 1998;54:653-662.

64.   McFarland CD, Thomas CH, DeFilippis C, Steele JG, Healy KE. Protein adsorption and cell attachment to patterned surfaces. Journal Biomedical Materials Researches. 2000;49:200-210.

65.   Detrait E, Lhoest J–B, Knoops B, Bertrand P, Van den Bosch de Aguilar P. Orientation of cell adhesion and growth on patterned heterogeneous polystyrene surface. Journal of Neuroscience Methods. 1998;84:193-204.

66.   Mattson MP, Haddon RC, Rao AM. Molecular functionalization of carbon nanotubes and use as substrates for neuronal growth. Journal of Molecular Neuroscience. 2000;14:175-182.

67. Madou, MJ. Fundamentals of microfabrication – The science of miniaturization, 2nd Edition, CRC Press, Boca Raton, FL. (2000)

68. Yang S, Leong KF, Du Z, and Chua CK. The design of scaffolds for use in tissue engineering. Part I. Traditional factors. Tissue Engineering. 2001; 7(6): 679-689.

69. Freyman TM, Yannas IV, Gibson LJ. Cellular materials as porous scaffolds for tissue engineering. Progress in Material Science. 2001;46: 273-282.

70. Tkacik G, Bedford M. US Patent No.5444097 (1992).

71. Huang YX, Ren J, Chen C, Ren TB, Zhou XY. Preparation and Properties of Poly(lactide-co-glycolide) (PLGA)/Nano- Hydroxyapatite (NHA) Scaffolds by Thermally Induced Phase Separation and Rabbit MSCs Culture on Scaffolds. Journal of Biomaterials Applications.2008;22(5);409-432.

72. Healy KE, Whang K, Thomas CH. US Patent No.5723508 (1996).

73. Levene HB, Lhommeau CM, Kohn JB. US Patent No.20006103255 (2000).

74. Sultana N, Wang M. Fabrication of HA/PHBV composite scaffolds through the emulsion freezing/freeze-drying process and characterization of the scaffolds. Journal of Material Sciences: Materials in Medicine. 2007;19(7):2555-2561.

75. Kim TK, Yoon JJ, Lee DS, Park TG. Gas foamed open porous biodegradable polymeric microspheres. Biomaterials. 2006; 27(2): 152-159.

76. Montjovent MO, Mathieu L, Hinz B. Biocompatibility of bioresorbable poly(L-lactic acid) composite scaffolds obtained by supercritical gas foaming with human fetal bone cells. Tissue Engineering. 2005; 11(11-12): 1640-1649.

77.   Harris L, Mooney DJ, Shea L. US Patent No.6281256 (2000).

78.   Leidner J, Wong EW, MacGregor DC, Wilson GJ. A novel process for the manufacturing of porous grafts: process description and product evaluation. J Biomed Mater Res 1983; 17(2): 229-247.

79.   Shastri VR, Martin I, Langer RS, Seidel J. US Patent No.6471993 (2002).

80.   Gorna K, Gogolewski S. Biodegradable porous polyurethane scaffolds for tissue repair and regeneration. Journal of Biomedical Materials Research A. 2006; 79(1): 128-138.

81.   Chen R, Chen H, Han J, Zhou D, Zheng C. Manufacture and study of porous poly(l-lactic acid) (PLLA)/beta-tricalcium phosphate (beta-TCP) composite. Sheng Wu Yi Xue Gong Cheng Xue Za Zhi. 2001; 18(2): 177-180.

82.   Itoh H, Wakisaka Y, Ohnuma Y, Kuboki Y. A new porous hydroxyapatite ceramic prepared by cold isostatic pressing and sintering synthesized flaky powder. Dental Materials Journal. 1994;13(1):25-35.

83.   Leong KF, Phua KK, Chua CK, Du ZH, and Teo KO, Fabrication of porous polymeric matrix drug delivery devices using the selective laser sintering technique. Proceedings of Institution of Mechanical Engineers. 2001; 215(2): 191-201.

84.   Xu T, Gregory CA, Molnar P, Cui X, Jalota S, Bhaduri SB, Boland T. Viability and electrophysiology of neural cell structures generated by the inkjet printing method. Biomaterials. 2006;27(19):3580-8.

85.   Rezwan K, Chen QZ, Blaker JJ, Boccaccini AR. Biodegradable and bioactive porous polymer/inorganic composite scaffolds for bone tissue engineering. Biomaterials 2006; 27(18):3413-3431.

86.   Hollister SJ. Porous scaffold design for tissue engineering. Nature Materials. 2005; 4(7): 518-524.

87.   Hartgerink JD, Beniash E, Stupp SI. Self-assembly and mineralization of peptide-amphiphile nanofibers. Science.2001;294: 1684-8.

88.   Kuntz RM, Saltzman WM. Neutrophil motility in extracellular matrix gels: mesh size and adhesion affect effect speed of migration. Biophysics Journal. 1997;72:1472-80.

89.   Benya PD, Shaffer JD. Dedifferentiated chondrocytes reexpress the differentiated collagen phenotype when cultured in agarose gels. Cell. 1982;30: 215-24.

90.   Ma PX, Zhang RY. Microtubular architecture of biodegradable polymer scaffolds. Journal of Biomedical Materials Research. 2001;56: 469-77.

91.   Hollister SJ, Maddox RD, Taboas JM. Optimal design and fabrication of scaffolds to mimic tissue properties and satisfy biological constraints. Biomaterials. 2002;23: 4095-103.

92.   Zhang RY, Ma PX. Synthetic nano-fibrillar extracellular matrices with predesigned macroporous architectures. Journal of Biomedical Materials Researches. 2000;52:430–8.

93.   Chen VJ, Ma PX. Nano-fibrous poly(l-lactic acid) scaffolds with interconnected spherical macropores. Biomaterials. 2004;25:2065–2073.

94.   Liu X, Won Y, Ma PX. Porogen-induced surface modification of nano-fibrous poly(L-lactic acid) scaffolds for tissue engineering. Biomaterials. 2006;27:3980–3987.

95.   Pham QP, Sharma U, Mikos AG. Electrospun poly(-caprolactone) microfiber and multilayer nanofiber/microfiber scaffolds: characterization of scaffolds and measurement of cellular infiltration. Biomacromolecules. 2006;7(10):2796-2805.

96.   Lee YH, Lee JH, An I-G, Kim C, Lee DS, Lee YK, Nam J-D. Electrospun dualporosity structure and biodegradation morphology of Montmorillonite reinforced PLLA nanocomposite scaffolds. Biomaterials. 2004;26(16):3165-3172.

97.   Correa-Duarte MA, Wagner N, Rojas-Chapana J, Morsczeck C, Thie M, Giersig M. Fabrication and biocompatibility of carbon nanotube-based 3D networks as scaffolds for cell seeding an growth. Nanoletters. 2004;4:2233-2236.

98.   Guan L, Davies JE. Preparation and characterization of a highly macroporous biodegradable composite tissue engineering scaffold. Journal of Biomedical Materials Researches. 2004;71(A):480-487.

99.   Woo KM, Chen VJ, Ma PX, Nano-fibrous scaffolding architecture selectively enhances protein adsorption contributing to cell attachment. Journal of Biomedical Materials Researches. 2003;67A(2):531-537.

100. McGrohon JB, Holder Jr. WD, Grimes LW, Thomas CB, Burg KJL. Evaluation of smooth muscle cell response using two types of porous polylactide scaffolds with different pore topography. Tissue Engineering. 2004;10(3/4):505-514.

101. Concini MT, Lora S, Baiguera S, Boscolo E, Folin M, Scienza R, Rebuffat P, Parnigotto PP, Nussdorfer GG. In vitro culture of rat neuromicrovascular endothelial cells on polymeric scaffolds. Journal of Biomedical Materials Researches. 2004;71(A):669-674.

102. Xu C, Inai R, Kotaki M, Ramakhrisna S. Electrospun nanofiber fabrication as synthetic extracellular matrix and its potential for vascular tissue engineering. Tissue Engineering. 2004;10(3/4):1160-1168.

103. Yang F, Murugan R, Ramakhrisna S, Wang X, Ma Y-X, Wang S. Fabrication of nano-structured porous PLLA scaffold intended for nerve tissue engineering. Biomaterials. 2004;25:1891-1900.

104. Barbucci R, Leone G. Formation of defined microporous 3D structures starting from cross-linked hydrogels. Journal of Biomedical Materials Researches. 2004;68(B):117-126.

105. Yamato M, Konno C, Koike S, Isoi Y, Shimizu T, Kikuchi A, Makino M, Okano T. Nanofabrication for micropatterned cell arrays by combining electron beam irradiated polymer grafting and localized laser ablation. Journal of Biomedical Materials Researches. 2003;67(A):1065-1071.

106. Smith LA, Ma PX. Nano-fibrous scaffolds for tissue engineering. Colloid and Surfaces. 2004;39(B):125-131

107. Norman JJ, Desai TA. Methods for Fabrication of Nanoscale Topography for Tissue Engineering Scaffolds. Annals of Biomedical Engineering .2006;34(1):89- 101.

108. Matthews JA, Wnek GE, Simpson DG, Bowlin GL. Electrospinning of collagen nanofibers. Biomacromolecules. 2002;3:232-238.

109. Creager SE, Hockett LA, Rowe GK. Consequences of microscopic surface roughness for molecular self-assembly. Langmuir. 1992;8:854-861.

110. Ellis-Behnke RG, Liang YX, You SW, Tay DKC, Zhang S, So K, Schneider GE. Nano neuro knitting: Peptide nanofiber scaffold for brain repair and axon regeneration with functional return of vision. PNAS. 2006;103(13): 5054-5059.

111. Yang F, Murugan S, Ramakrishna S, Wang X, Ma YX, Wang X. Fabrication of nano-structured porous PLLA scaffold intended for nerve tissue engineering. Biomaterials. 2004;25:1891–1900.

112. Moxon KA, Kalkhoran NM, Markert M, Sambito MA, McKenzie JL, Webster JT. Nanostructured surface modification of ceramic-based microelectrodes to enhance biocompatibility for a direct Brain-Machine Interface. IEEE transactions on biomedical engineering. 2004;51(6):881-889.

113. Dalby M, Riehlea MO, Sutherland DS, Agheli H, Curtis ASG. Changes in fibroblast morphology in response to nano-columns produced by colloidal lithography. Biomaterials. 2004;25:5415–5422.

114. Berry CC, Dalby MJ, McCloy D, Affrossman S. The fibroblast response to tubes exhibiting internal nanotopography. Biomaterials. 2005;26:4985–4992.

115. Lee CH, Shin HJ, Cho IH, Kang Y-M, Kim IA, Park K-D, Shin J-W. Nanofiber alignment and direction of mechanical strain affect the ECM production of human ACL fibroblast. Biomaterials. 2005;26:1261-70.

116. Yin L, Bien H, Entcheva E. Scaffold topography alters intracellular calcium dynamics in cultured cardiomyocyte networks. American Journal of Heart Circulatory Physiology. 2004;287:H1267-H1285.

117. Dalby MJ, Riehle MO, Sutherland DS, Agheli H, Curtis ASG. Fibroblast response to a controlled nanoenvironment produced by colloidal lithography. Journal Biomedical Materials Researches. 2004;69(A):314-322.

118. Vance RJ, Miller DC, Thapa A, Habersroth KM, Webster TJ. Decreased fibroblast cell density on chemically degraded poly-lactic-co-glycolic acid, polyurethane and polycaprolactone. Biomaterials 2004;25:2095-2103.

119. Li W-J, Tuli R, Huang X, Laquerriere P, Tuan RS. Multilineage differentiation of human mesenchymal stem cells in a three-dimensional nanofibrous scaffolds. Biomaterials. 2005;26(25):5158-5266.

120. Nagaoka S, Ashiba K, Kawakami H. Biomedical properties of nanofabricated fluorinated polyimide surface. Artificial Organs. 2002;26(8):670-675.

121. Martinez-Pinna J, Lamas JA, Gallego R. Calcium current components in intact and dissociated adult mouse sympathetic neurons. Brain Research 2002;951:227-236

122. Mahanthappa NK, Patterson PH. Culturing mammalian sympathoadrenal derivatives. In Banker, G. and Goslin K. Culturing nerve cells (2nd ed.). MIT Press. pp 289-307. (1998)

123. Martin DP, Schmidt RE, Distefano PS, Lowry OH, Carter JG, Johnson EM Jr. Inhibitors of protein synthesis and RNA synthesis prevent neuronal death caused by nerve growth factor deprivation. Journal of Cell Biology. 1988;106:829-844.

124. Carey MB, Matsumoto SG. Spontaneous calcium transients are required for neuronal differentiation of murine neural crest. Developmental Biology. 1999; 215(2):298-313.

125. Rittenhouse AR, Zigmond RE. Role of N- and L-type calcium channels in depolarization-induced activation of tyrosine hydroxylase and release of norepinephrine by sympathetic cell bodies and nerve terminals. Journal of Neurobiology. 1999;40(2):137-148.

126. Gage FH. Mammalian neural stem cells. Science. 2000;287:1433-1438.

127. Dhara SK, Hasneen K, Machacek DW, Boyd NL, Rao RR, Stice SL. Human neural progenitor cells derived from embryonic stem cells in feeder-free cultures. Differentiation. 2008;76(5):454-464.

128. Snyder, E.Y. Neural stem-like cells: developmental lessons with therapeutic potential. Neuroscientist. 1998;4:408–425.

129. McKay RDG. Stem cells in the CNS. Science. 1997;276:66–71.

130. Ackerman MJ, Clapham DE. Ion channels-basic science and clinical disease. New England Journal of Medicine. 1997;336(22):1575-1586.

131. Curran ME. Potassium ion channels and human disease: phenotypes to drug targets? Current Opinion in Biotechnology. 1998;9(6):565-572.

132. North RA. Editor. Ligand- and Voltage-gated Ion Channels. Boca Raton, FL: CRC Press. (1995)

133. Denyer J, Worley J, Cox B, Allenby G, Banks M. HTS approaches to voltage-gated ion channel drug discovery. Drug Discovery Today. 1998;3(7):323-332.

134. Hatta S, Sakamoto J, Horio Y. Ion channels and diseases. Medical Electron Microscopy. 2002;35:117-126.

135. Xu, J, Wang, X, Ensign, B, Li, M, Wu, L, Guia, A, Xu, J. Ion-channel assay technologies: quo vadis? Drug Discovery Today. 2001;6(24):1278-1287.

136. Banks M, Binnie A, Fogarty S. High throughput screening using fully integrated robotic screening. Journal of Bimolecular Screening. 1997;2:133–135.

137. Lai Y, Wang L, Cheng K, Kisaalita WS. Taking cell culture in drug discovery to the third dimension – a patent review. Recent Patents on Biomedical Engineering. (In press).

138. Green JA, Yamada KM. Three-dimensional microenvironments modulate fibroblast signaling responses. Advanced Drug Delivery Reviews. 2007;59(13):1293-8.

139. Haq F, Rao YL, Keith C, Zhao Y, Zhang G. Nano- and micro-structured substrates for neural cell development. Journal of Biomedical Nanotechnology. 2005;1(3):313-319.

Table 2.1. Components of extracellular matrix.

Components	Functions
Structural Proteins	
Collagen	25 % of all ECM
Elastin	elasticity of ECM
Specialized Proteins	
Fibrillin	connective tissue
Fibronectin	cell attachment
Laminin	other functions such like cell proliferation
Proteoglycans	
Hyaluronate	components of synovial fluid, vitreous humor, ECM of loose connective tissue
Chondroitin sulfate	cartilage, bone, heart valves
Heparan sulfate	basement membranes, cell surfaces
Heparin	component of intracellular granules of mast cells lining the arteries of the lungs, liver and skin
Keratan sulfate	components of skin, blood vessels, heart valves
Dermatan sulfate	components cornea, bone, cartilage aggregated with chondroitin sulfates

Table 2.2. Commercially available 3D cell culture products with potential for HTS applications [137].

Trade name	Matrigel	Geltrex	Extracel Hydrogels	AlgiMatrix
Company	BD	Invitrogen	Glycosan Biosystems	Invitrogen
Material	Laminin, Collagen, etc. (natural)	Laminin, Collagen, etc (natural)	Hyaluronic acid and denatured collagen (natural)	Alginate (natural)
Pore size	N/A	N/A	N/A	40-300 □m
Fiber size	N/A	N/A	N/A	N/A
Mechanical	low	low	low	med
Ready-to-use	No, preparation required	Yes	Yes	Yes
microscopy	Opaque	Transparent	Transparent	Opaque
Cell recovery	Recovery solution provided, easy	Enzymetic digestion of Collagen and Laminin, easy	Recovery solution provided, easy	Trypsin, hard
Biodegradable	Yes	Yes	Yes	No
96-well plate availability	No	No	Yes	Yes
Continued				
Trade name	PuraMatrix	3D Collagen Culture Kit	UltraWeb	
Company	3DM, Inc.	Millipore	Corning	
Material	16 mer peptide (synthetic)	Type I and Type III collagen	Polyamide(Nylon) (synthetic)	

		(natural)		
Pore size	50-400 nm	N/A	300-500 nm	
Fiber size	7-10 nm	N/A	280 nm	
Mechanical	low	low	Med	
Ready-to-use	No, time consuming	No, preparation required	Yes	
microscopy	Transparent	Transparent	Opaque	
Cell recovery	Spin, easy	Collagenase, easy	Trypsin, easy	
Biodegradable	Yes	Yes	No	
96-well plate availability	No	No	Yes	

Table 2.3. Comparison of methods for producing three-dimensional polymer scaffolds.

Fabrication methods	Matrix structures	Porosity	References
Gas foaming	Spongeous	0.93	[75], [76], [77]
Particulate leaching	Spongeous	0.9	[80], [81]
Sintering	Spongeous	0.9	[82], [83]
Three-dimensional printing	Controlled pores	0.5	[84]
Emulsion freeze drying	Spongeous	0.9	[72], [73], [74]
Phase separation	Fibrous	0.9	[70], [71]
Fiber bonding	Fibrous	0.81	[78], [79]

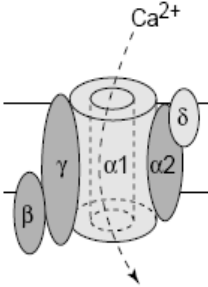Table 2.4. Comparison of some fabrication methods for generating nano-scale

Topographies [107].

Fabrication method	Sizes	Features
Photolithography	> 500 nm	Precise geometries, but low resolution
Electrospinning	> 30 nm	Fiber geometry only
Polymer demixing	> 15 nm	Simple, fast and inexpensive method
Chemical etching	> 1 nm	Uncontrollable geometries
Colloidal lithography	20-100 nm	Uncontrollable geometries
Phase separation	100-500 nm	Uncontrollable patterns
Self assembly	Depends	Limited to materials that will undergo self-assemby
E-beam lithography	10- 40 nm	Precise geometry and patterns, but expensive

Table 2.5. Effects of nanofibers on cell behaviors.

Nanofibers	Cell types	Observed effects	References
Self-assembly peptide nano fibers	Neural stem cells	differentiation	110
PCL nano fibers	human mesenchymal stem cells	differentiation	119
Nano-grooved surfaces	cardiomyocyte	Intracellular calcium level changes	116
Polyurethane Nano-fibers	Human ligament fibroblast	Increased ECM production	115
Polyamide nanofibers	NIH 3T3 fibroblasts and rat kidney cells	Cytoskeleton changes	8
Nano-columns	Fibroblast cells	Cell morphology and cytoskeleton aliment changes	114
nano-tubes	Fibroblast cells	Cell morphology and cytoskeleton aliment changes	113
Self-assembly peptide nano fibers	Neuronal cells in the young and adult brains	Axon outgrowth and neural regeneration	110
Nano-porous silicon surfaces	pheochromocytoma cells	Neurite outgrowth	112
PLLA nano fibers	Mouse neural stem cells	Neurite outgrowth	103

Table 2.6. Voltage gated calcium channel families [133].

| Subunit structure	Nomenclature and tissue distribution	Molecular identity	Disease targets
Ca²⁺ channel Subunits: α1, β, γ, α2–δ 		Of α1 subunit	For Ca²⁺-channel blockers
	P/Q-type (neuronal)	α1A	Angina, arrhythmia,
	N-type (neuronal)	α1B	hypertension, atherosclerosis,
	L-type (cardiac)	α1C	pain, neuroprotection,
	L-type (neuronal)	α1D	migraine, stroke, Alzheimer's,
	R-type (neuronal)	α1E?	cognitive enhancement and
	T-type (neuronal)	α1G	dementia
	L-type (skeletal)	α1S	
	T-type (cardiac)	?	
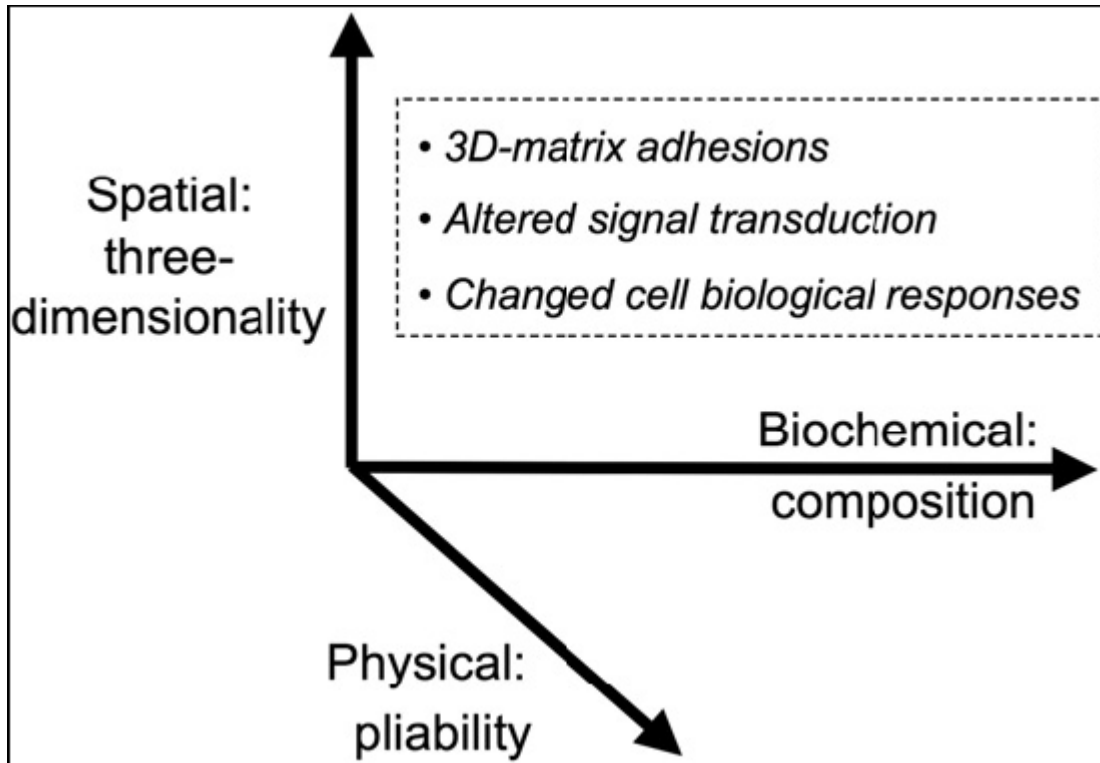
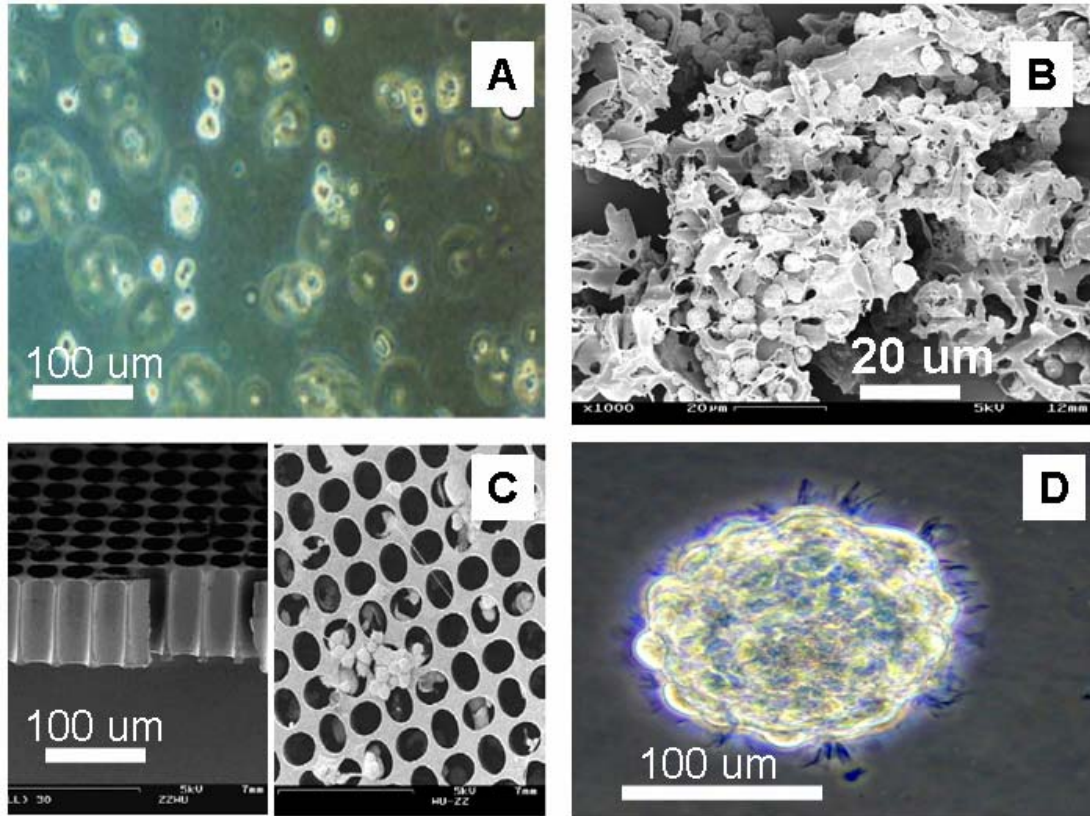Figure 2.1. Factors in the ECM that regulates cell responses. [138]

Figure 2.2. 3-D cell culture formats. (A): natural polymer scaffolds (collagen hydrogel) [21]; (B) synthetic polymer scaffolds; (C): SU-8 mciro-patterned structures [23]; (D): multi-cellular spheroids [24].
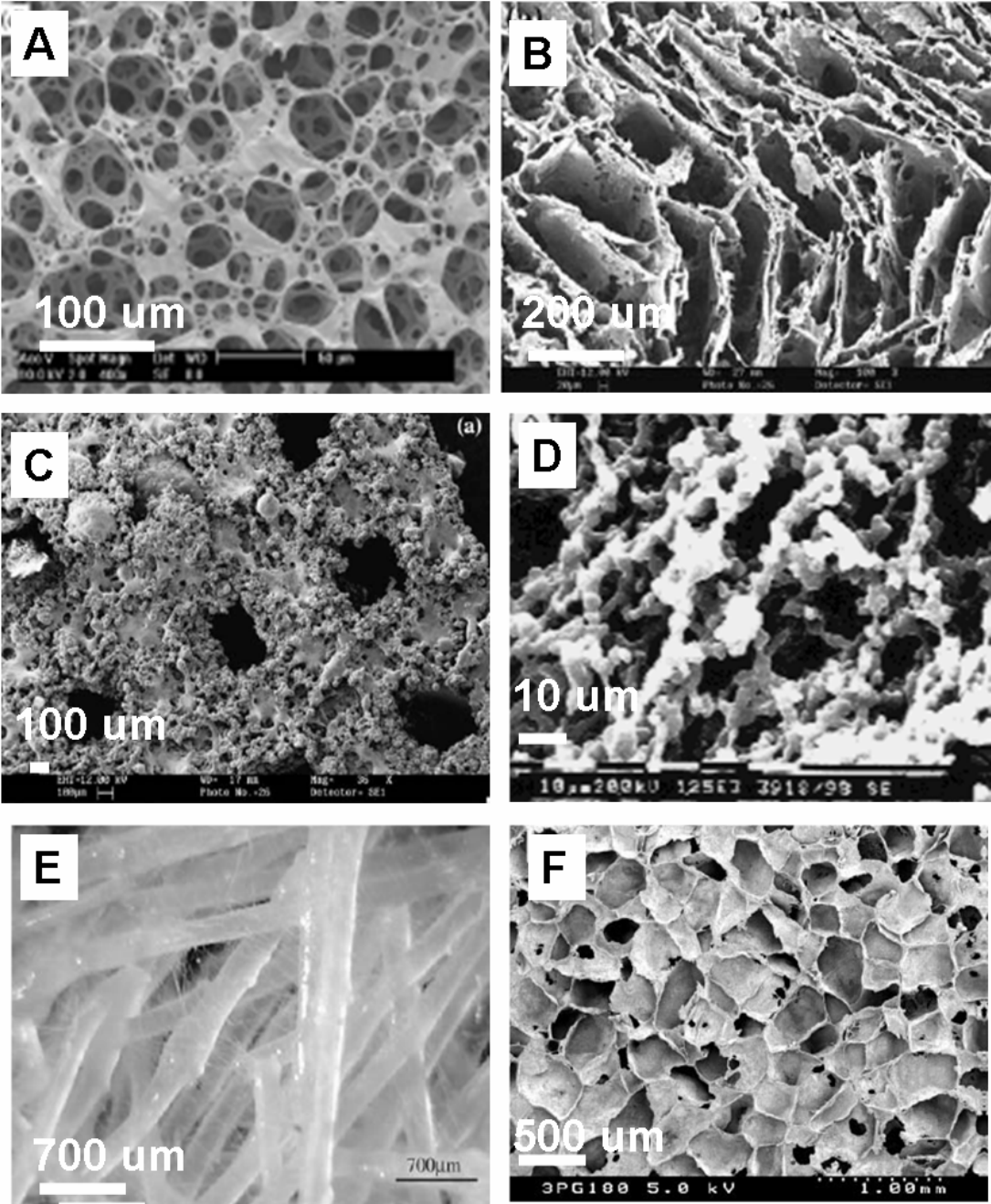
Figure 2.3. Micrographs of scaffolds fabricated using different methods: (A) gas forming [75],

(B) emulsion freeze drying [74], (C) sintering [83], (D) phase separation [71], (E) fiber bonding

[78], (F) particulate leaching [80].
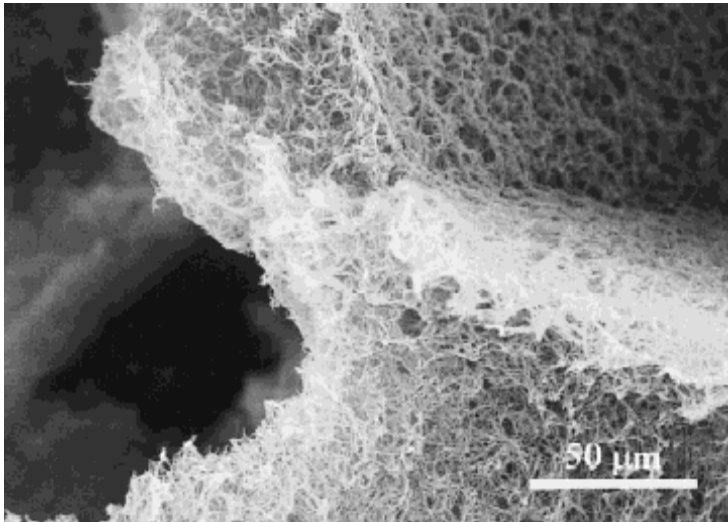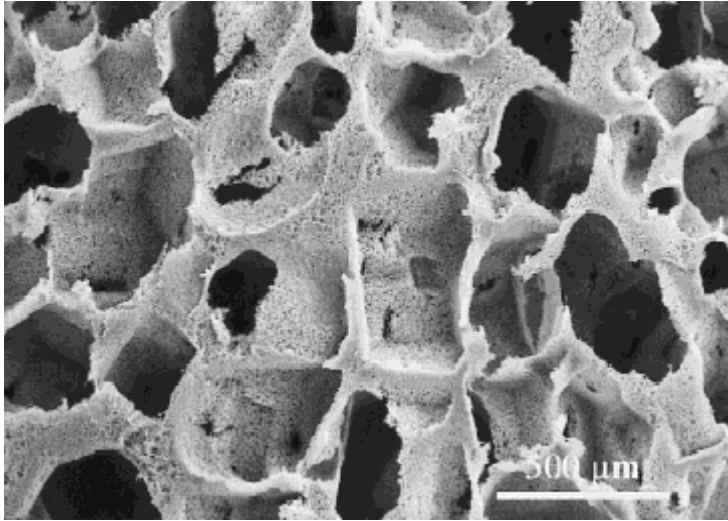
Figure 2.4. Combination scaffolds with micro-scale pores and nano-scale fibers [92].
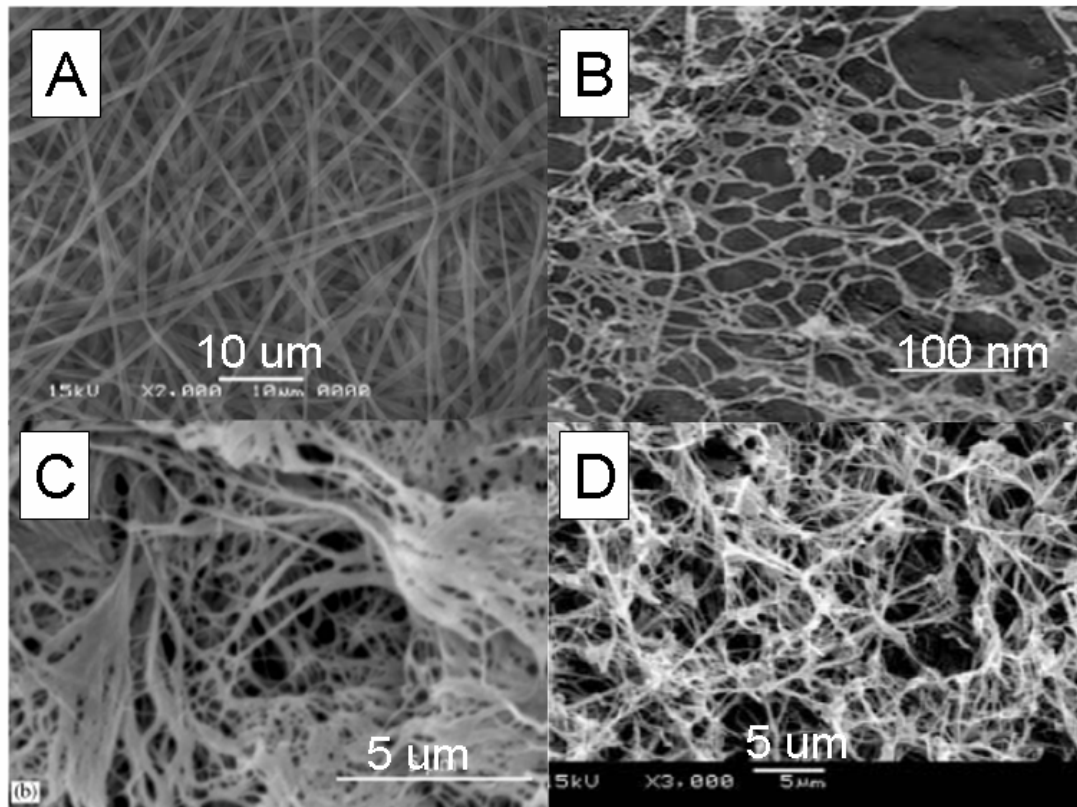
Figure 2.5. SEM images of nano-structures fabricated with different methods: (A)

Electrospinning [102], (B) molecular self-assembly [110], (C) particulate leaching [92], and (D)

phase separation [103].
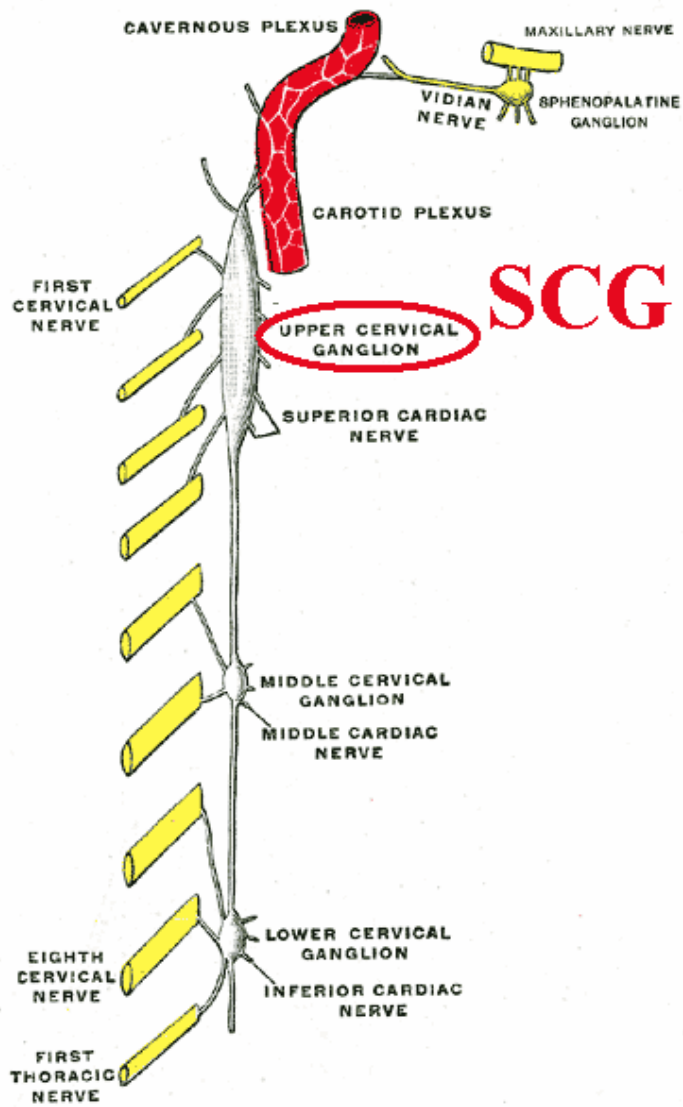
Figure 2.6. Location of SCG in the nervous system.

http://en.wikipedia.org/wiki/Superior_cervical_ganglion accessed on April 10, 2008
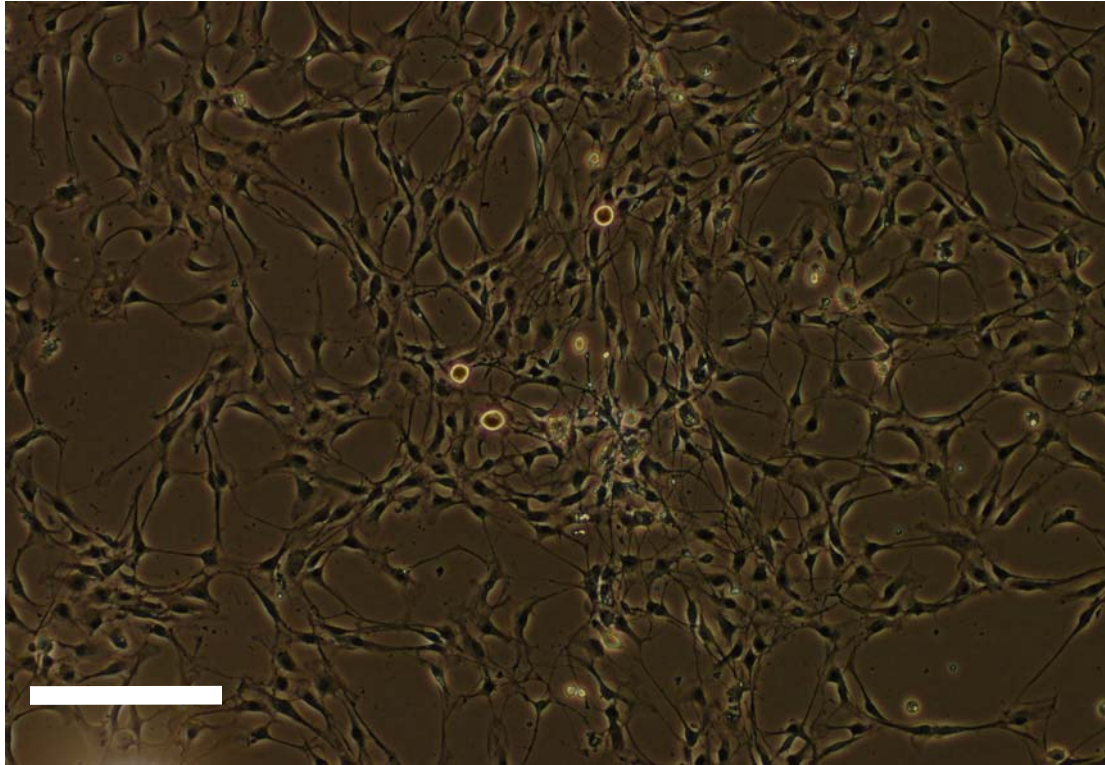
Figure 2.7. Phase contrast image of mouse SCG cells on flat surfaces coated with Type I collagen.

Bar represents 100 µm.

Potential Stem Cells with Neural Capability

Restriction		Cell	Source
totipotent non self-renewing		zygote	zygote
pluripotent self-renewing		embryonic stem cell	blastocyst
broad potential self-renewing		multipotent stem cells	embryo or adult brain, blood(?)
limited potential limited self-renewal		neural progenitor	brain or spinal cord
limited division non-functional		committed neural progenitor	brain subregion
	neuronal progenitor glial progenitor		
non-mitotic functional		differentiated	specific brain sites
	neuron glia		

Figure 2.8 An illustration proposing the classes of mammalian stem cells that can give rise to neurons, presented as a hierarchy beginning with the most primitive and multipotent stem cell and progressing to the most restricted [126].
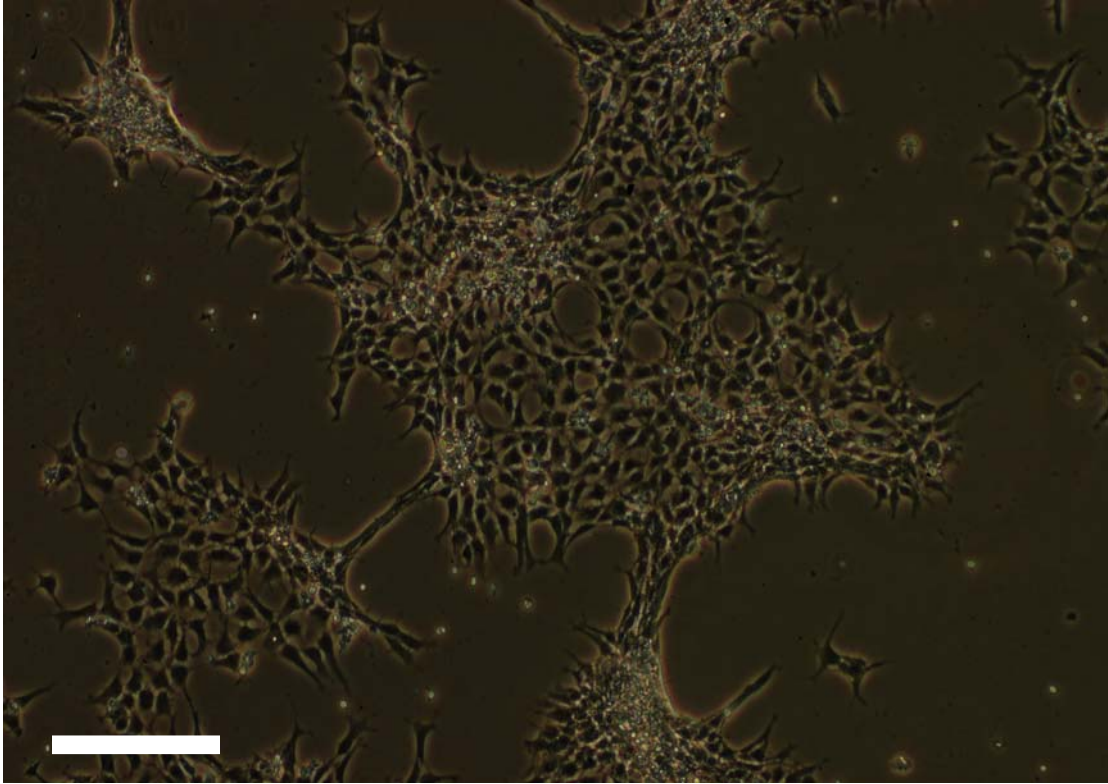
Figure 2.9. Human neural stem cells culture on flat surfaces. Bar represents 100 μm.
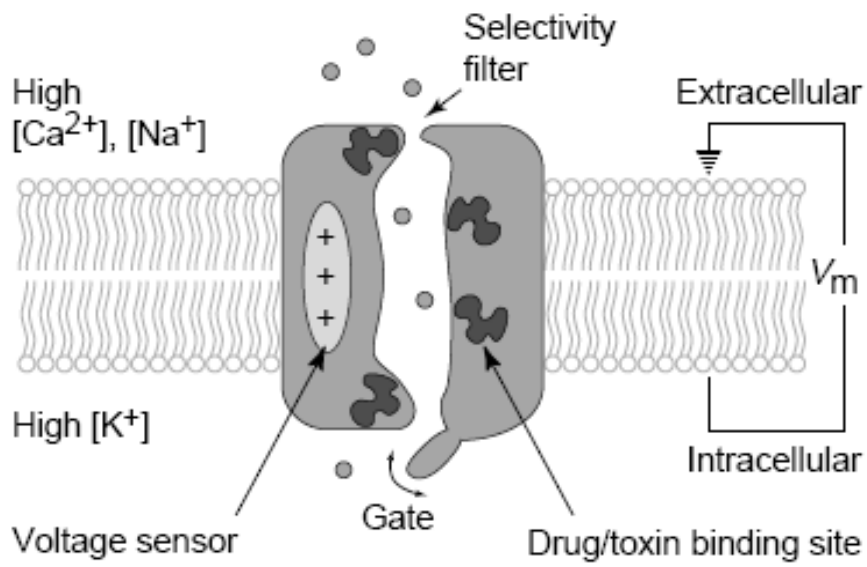
Figure 2.10. Schematic representation of a voltage-gated calcium channel. [133]
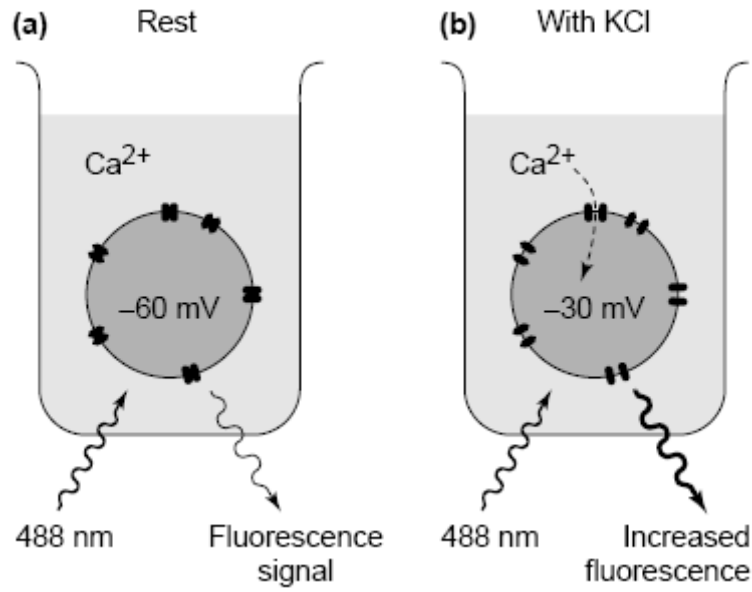
Figure 2.11. Schematic representation of a fluorescence-based 96-well calcium-channel assay [133].
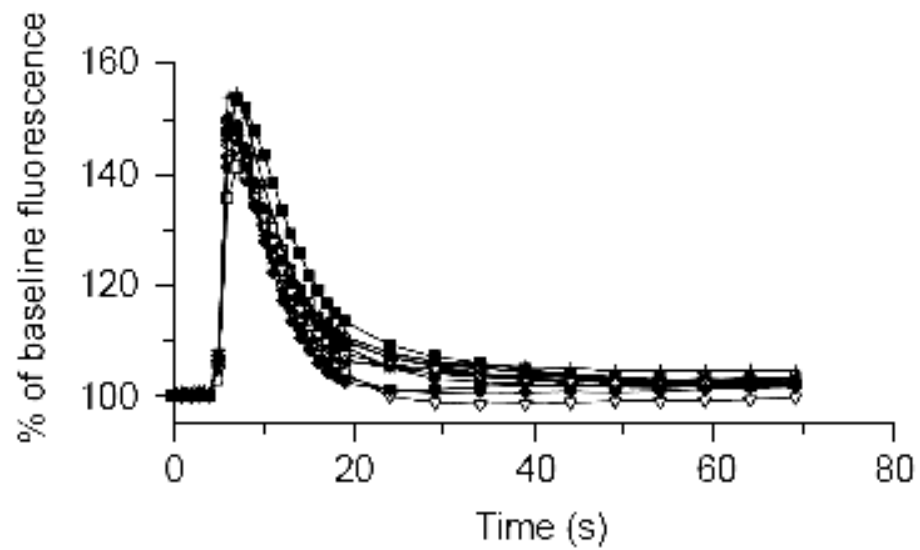
Figure 2.12. Fluorescence recording of Ca2+ responses in human neuroblastoma cells [133].
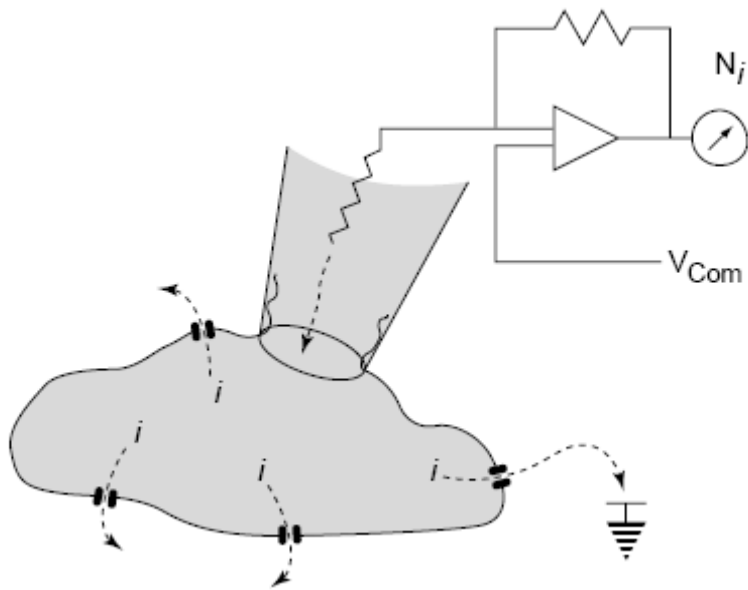
Figure 2.13. Illustration of patch clamp technique [133].

CHAPTER 3

THREE DIMENSIONAL POLYMER SCAFFOLDS FOR HIGH

THROUGHPUT CELL-BASED ASSAY SYSTEMS*

3.1 Abstract

Many whole cell-based assays in use today rely on flat, two-dimensional (2D) glass or

plastic substrates that may not produce results characteristic of in vivo conditions. In this study, a

three dimensional (3D) cell-based assay platform was established by integrating 3D synthetic

polymer scaffolds with standard cell culture dishes and multi-well plates. This technology can be

used to feasibly modify any traditional 2D cell-based assay vessels for 3D cell-based assay with

currently used high throughput screening (HTS) systems. We examined neural stem (NS) cells'

growth profile, morphology, cell-matrix interaction, gene expression and voltage gated calcium

channel (VGCC) functionality of this novel 3D assay platform. Our results showed that unlike

the NS cells cultured on traditional 2D planar surfaces, cells in 3D scaffolds are more

physiologically relevant with respect to in vivo characteristics exhibited by in-vivo surrogates

such as neural spheres. This new biomimetic cell-based assay platform may provide a broadly

applicable 3D cell-based system for use in drug discovery programs and other research fields.

3.2 Introduction

The common approaches used by the pharmaceutical industry to screen small molecule libraries and build new classes of lead compounds, frequently includes a series of in vitro functional and toxicity high throughput screening (HTS) assays [1]. A relatively new approach to drug discovery assay design is to use live cells as the bio-recognition elements for compound functional validation and toxicity testing [2]. Live cell assays are purposely considered to yield results that are more physiologically relevant when compared to biochemical assays. Although cell-based screening has been established in the drug discovery process, its value in accurately predicting clinical response to new agents is limited. This lack of predictability has been partially attributed to the fact that such systems commonly employed two-dimensional (2D) cellular assays, which do not mimic the response of cells in the three-dimensional (3D) milieu present in a tissue, or in vivo [3]. Ideal cell-based screening systems call for research efforts to create simple, robust and effective 3D cell-based platforms so that cellular responses will be more representative of those under in vivo conditions.

Various methods and materials have been studied for creating 3D microenvironments. Among them are microgravity bioreactors [4], natural polymers especially collagen hydrogels [5,6], photopolymerized hydrogels [7], synthetic polymer scaffolds [8, 9], self-assembling peptide scaffolds [10], micro/nano patterned substrates [11], 3D cellular structures generated by inkjet printing [12], and multi-cellular spheroid (MCS) such as neural spheres. With respect to the applications in HTS cell-based assays, synthetic polymer scaffolds offer several comparative

advantages. First, in comparison to microgravity bioreactors, patterned substrates and MCSs, polymer scaffolds are much easier and faster to prepare and can be scaled down for incorporation into 96-well plates for HTS, consistent with state of the art instrumentation. Second, in comparison to most natural polymer hydrogels, rigid polymer scaffolds offer less resistance to diffusion of nutrients and wastes to and from cells deeper in the scaffolds [6]. Third, in comparison to nanoscale pores and fibers associated with self-assembling peptide scaffolds, polymer scaffolds' micro-scale pores are large enough to host multi-cellular aggregates which are observed in tissue engineering studies [13].

We have established a novel process (U.S. patent pending) that incorporates 3D synthetic polymer scaffolds into standard cell culture dishes and multi-well plates in a precise and rapid manner that supports the formation of 3D cell cultures. These 3D cell-based assay vessels (hereafer refered to as 3D vessels) were fabricated by casting a thin layer of porous polymer scaffolds onto the glass bottom of a regular cell culture vessel. The 3D scaffolds were fixed on these vessels without using any adhesives. With the aid of liquid handling robots, this 3D vessel fabrication technology can be applied to modify most currently available 2D cell culture vessels (24-well, 96-well and 384-well plates) for 3D cell culture and cell-based assay usage. With this method, it is feasible to bring 3D cell cultures into most of the HTS cell-based assay systems used in pharmaceutical and biotechnology industry today.

After extensive physical characterization, human neural stem (NS) cells, also know as neural progenitors, were cultured in these 3D vessels to examine cellular growth profile, morphology, cell-matrix interaction, gene expression and voltage gated calcium channel (VGCC)

function. Our results showed that NS cells in 3D vessels are physiologically more relevant with respect to in vivo characteristics exhibited by the neural spheres (in vivo surrogates). Moreover, in comparison to available 3D cell culture technology and products, our 3D vessels provide ready-to-use convenience, and automated instrumentation compatibility. This new biomimetic cell-based assay platform provides a broadly applicable 3D cell-based system for use in drug discovery programs and other research fields such as toxicology, cancer and stem cell research, development and morphogenesis, and tissue/organ engineering.

3.3 Materials and methods

3.3.1 Scaffold Fabrication

Generally, a viscous polymer solution was prepared by dissolving polystyrene or poly-l lactic acid (PLLA) in chloroform. Sieved ammonium bicarbonate particles in the range of 40-60 µm were added to the polymer solution and mixed thoroughly. The paste mixture of polymer/salt/solvent was cast into the wells of a standard cell culture vessel with a single- or multi-channel pipette. The mixture was viscous and as such the vessels were gently rocked to obtain even layers. MatTek® glass bottom Petri dishes (Cat#: P35G-0-14; well diameter: 14 mm) and 96-well plates (Cat#: P96G-0-5-F; well diameter: 5 mm) were used for 3D vessel fabrication. The casting mixture was composed of 0.1 g polystyrene, 2 g ammonium bicarbonate and 4 ml chloroform. Usually, 70-150 µL and 10-30 µL of mixture were cast into each well of Petri dishes and 96-well plates, respectively. After casting, the vessel was immediately covered to control the

evaporation rate of chloroform. This step was crucial as chloroform also served as an adhesive to

"weld" the scaffold by partially dissolving the polystyrene wall of the well. After chloroform

was completely evaporated, the dishes and plates were baked in an oven overnight. At any

temperatures above 36 °C, ammonium bicarbonate decomposed to ammonia, carbon dioxide, and

water and left pores, creating a porous polymer scaffold. Although a higher temperature can

achieve removal of ammonium bicarbonate faster, the baking temperature can not exceed the

glass temperature (Tg) of the polymer in use, as well as the maximum temperature the cell

culture vessels can tolerate.

3.3.2 Scaffold characterization

The porosities of the polymer scaffolds were measured by a modified liquid displacement

method [14]. In our study, ethanol was used as the displacement liquid. Porosity was determined

for the scaffolds in Petri dishes. The scaffolds were carefully removed from the dishes with an

ultra-sharp blade and then submerged in ethanol. Scaffold mechanical strength was evaluated by

determining the capacity to absorb fluid-mechanical energy without damage [6]. A syringe pump

(Orion, Boston, MA), connected to a standard 200 µl pipette tip, was used. De-ionized water was

perpendicularly pumped onto the surface of polymer scaffolds for 5 s through the tip. The flow

rate inducing scaffolds rupture was recorded. The force, F, experienced by the scaffolds was

calculated as follows:

$F=\rho \cdot A \cdot v^2$

where ρ is the density of the de-ionized water, A the area of the opening of the pipette tip and v is the fluid flow rate just before impact, which depends on the rate of the syringe piston movement and the diameter of the nozzle tip. Light transmittances of polymer scaffolds were measured by an inverted microscope (TE3000, Nikon) coupled with a digital camera (D100, Nikon). Images taken with the same lamp power and exposure time were processed with SimplePCI 2000 software. The light transmittance ratio was calculated by dividing the sample mean grey level from three different spots by the control grey level (plain cover slips).

3.3.3 Scanning electron microscopy (SEM)

Cells on scaffolds were fixed with 2% glutaraldehyde in 0.1 M sodium cacodylate buffer (pH 7.2) for 1 h and then rinsed in cacodylate buffer three times (15 min each). This was followed by post-fixing with 1% OsO_4 in 0.1 M sodium cacodylate buffer for 1 h and rinsing in cacodylate buffer three times (5 min each). The samples were then dehydrated in 35, 50, 70, 80, 95 and 100% ethanol successively for 10 min each and dried in a SAMDRI-780A critical point drier (Tousimis Research Corporation, MD). Scaffolds were sputter-coated with gold for 60 s to achieve a thickness of about 15.3 nm. SEM images were captured with a LEO 982 scanning electron microscope (LEO Electronenmikroskopie GmbH Korporation, Germany). A similar protocol was followed for scaffold samples without cells, with the exception that the preparation started with sputter coating.

3.3.4 Neural stem cell culture

Human NS cells were isolated by the Regenerative Bioscience Center at the University of Georgia. These cells are now commercially available as ENStem-A[TM] from Millipore (Billerica, MA). The cells were maintained in neural basal media (Invitrogen, PA) supplemented with penicillin/streptomycin, L-glutamine, recombinant human leukemia inhibitory factor (hLIF), basic fibroblast growth factor (bFGF) and B-27 (a serum-free supplement). The composition of differentiation media was similar to the subculture media described above but without bFGF. The NS cells were incubated at 37 °C in a 5% CO_2 humidified atmosphere. Before cell seeding, both the scaffolds in Petri dishes and 96-well plates were pre-wetted and sterilized in 70% ethanol overnight. To achieve better cell attachment and rule out any difference caused by the polymer materials, both the scaffolds and flat cover slips were coated with poly-ornithine (Sigma-Aldrich, MO; molecular weight is 30,000-70,000) and laminin (Sigma-Aldrich, MO; from Engelbreth-Holm-Swarm murine sarcoma basement membrane). The scaffolds were submerged in 20 µg/ml poly-ornithine water solution overnight and then in 5 µg/ml laminin water solution overnight for achieving complete coating. Before cell seeding, the laminin solution was aspirated from the scaffolds. For both 2D and 3D cell culture, NS cells were seeded with a uniform density of 50,000 cells/cm^2. For neural sphere cell culture, 1×10^6 cells were seeded into a 35 mm Petri dish without coating of poly-ornithine and laminin. Uncoated surfaces prevented cells from adhesion but encouraged them to form neural spheres. In some experiments, NS cells were induced to differente by replacing the growth media with differentiation media.

3.3.5 Immuno-fluorescence staining

Rabbit (polyclonal) anti-FAK PY^{397} antibody was purchased from Biosource International, CA, USA. Polyclonal rabbit anti Cav1.2 alpha1C, L type antibody was purchased from Alomone Labs, Israel. Secondary antibody Alexa Fluor® 488 chicken anti-rabbit (H+L) was purchased from Molecular Probes, OR, USA. Normal chicken serum was purchased from Zymed Laboratories, CA. For immuno-fluorescence staining, cells were rinsed once with phosphate-buffered saline (PBS), fixed with 4% paraformaldehye in PBS (15 min), washed with PBS, treated with 0.5% Triton X-100 (5 min). After that, cells were washed with PBS, blocked with normal chicken serum (2% diluted with PBS/0.3% Tween-20) for 30 min at room temperature, washed with PBS (3×, 5 min per wash), incubated overnight with primary antibody (1:100), washed with PBS (3×, 5 min per wash) followed by incubation for 1 h with the secondary antibody (1:500), washed with PBS (3×, 5 min per wash), and then loaded with Dapi (1:5000) for 5 min at room temperature. After PBS wash, cells were ready for microscopy observation. Confocal imaging was performed with a Leica TCS SP2 microscope. Routine negative controls for staining were performed.

3.3.6 Western blot analysis

NS cells were lysed using CelLytic M Cell lysis reagent (Sigma, St Louis, MO) for 15 mins followed by 15 mins centrifugation at 12,000 x g to pellet the cellular debris. Supernatant was removed and protein concentrations were determined by the Bradford assay. Equivalent amounts (40 μg) of protein for each sample were resolved in 12.5% SDS-PAGE in duplicates. After electrophoresis, proteins were transferred to nitrocellulose membranes. Membranes were incubated in Tris-buffered saline, pH 7.4 with 0.5% Tween 20 (TBS-T), containing 5% nonfat milk, for 1 h at room temperature.   The blots were then reacted with rabbit anti-Ca$_v$1.2 (1:1000; Alomone) at 4 ℃ overnight. Biotinylated secondary anti-rabbit antibody, avidin-biotin complex solution (Vectastain Elite ABC kit) and DAB Substrate Kit (all from Vector Laboratories) were used to visualize antibody-antigen complex.   L type voltage- gated calcium channel alpha1C bands were detected at 75 kDa.

3.3.7 Microarray gene expression analysis

Total RNA was isolated from all samples using Qiagen RNeasy Kits (Qiagen, Valencia, CA) according to the manufacturer's standard protocol. The quantity of mRNA isolated from each sample was determined using the adsorption of each solution at 260 and 280 nm. The purity of each sample was monitored using the A_{260}/A_{280} ratio. A ratio of 1.8–2.1 was considered a "clean"

sample and could be used in microarray experiments. Samples were kept on dry ice and sent to the Affymetrix Core Facility at the Medical College of Georgia (MCG) for Human Whole Genome U133A 2.0 Plus GeneChip Expression Analysis (Affymetrix, Santa Clara, CA).

The expression value of each gene was obtained by Expression Console (Affymetrix) with the probe logarithmic intensity error (PLIER) algorithm. PLIER was chosen because it is designed to produce an improved signal (a summary value for each probe set) by accounting for experimentally observed patterns for feature behavior and handling error appropriately at low and high abundance. Expression values were then normalized using the Quartile Normalization technique as suggested by Affymetrix. Genes within the scope of this study were manually picked. Student *t* tests and ANOVA tests were carried out to compare the expression differences between 2D, 3D and neural sphere samples. More detailed microarray experimental results will be reported in a forth coming paper from our group.

3.3.8 VGCC functionality characterization

Intracellular calcium dynamics were recorded using the membrane-permeable dyes Calcium Green-1 AM or Fluo-4 (Molecular Probes Inc., Eugene, OR), with confocal laser scanning microscopy. Both 2D and 3D cultured cells were washed 3 times with Neural Basal Media and loaded with 5 µM dye in 1 ml of Neural Basal Media containing 3% FBS and 0.02% Pluronic F-127. The samples were incubated at 37 °C for 30 min. After dye loading, cells were

rinsed with Neural Basal Media twice and retuned to the incubator for another 30 min to allow complete dye de-esterification. Cells were depolarized by adding 10% (v/v) of high potassium buffer to a final concentration of 50 mM K^+ while imaging. The intracellular calcium dynamics were reflected by changes in intracellular Calcium Green-1 or Fluo-4 fluorescence intensity.

3.4 Results and discussion

3.4.1 Fabrication and characterization of 3D cell-based assay vessels

We started with MatTek® glass-bottom Petri dishes/96-well plates to produce 3D cell-based assay vessels. However as described in the Materials and Methods section, this process can be easily adapted to any other 2D cell-based assay vessels. The fabrication process is illustrated in Figure 3.1a. As shown, a viscous polymer solution was prepared by dissolving polystyrene in chloroform solution with ammonium bicarbonate particles. The paste mixture was then cast into the wells of a standard cell culture vessel. After chloroform was completely evaporated, the dishes and plates were baked to remove ammonium bicarbonate, creating a thin porous polymer scaffold. Figure 3.1b& c show pictures of the fabricated 3D cell culture/assay dishes and 96-well plates. These vessels were kept in desiccators until use.

The porosity of the 3D scaffolds was above 85% with average pore size in the range of 60-100 μm in diameter. The porosity and pore size of the scaffolds were determined by liquid displacement method and analysis of SEM images, respectively. The pore size range, which was a little bigger than the size range of salt particles used, was chosen in relation to the size of the

cells seeded onto the scaffolds. Smaller pores prevented cell intrusion, while larger pores made

cell-matrix interaction identical to 2D conditions [13]. The porosity of a scaffold was controlled

by the salt/polymer weight ratio. To get three different porosity groups, 20:1, 15:1 and 10:1

(wt/wt) salt/polymer ratio were used for scaffold fabrication. Accordingly, the thickness of a

scaffold was precisely controlled by the volume of paste mixture used for casting, given that the

bottom area of the vessels was fixed. To get three different thickness conditions, 20:1 porosity

group scaffolds were cast with three mixture volume of 150, 100 and 70 µl. The baking

temperature could be any point between the decomposition temperature of ammonium

bicarbonate (36 °C) and the glass transition temperature of the polystyrene (95 °C). Based on the

above fact, we baked the polystyrene scaffold at 85 °C for quick removal of ammonium

bicarbonate. Methods to remove ammonium bicarbonate particulates were not limited to baking.

Cold water rinsing also can remove the salts by dissolution while hot water rinsing achieves

removal much faster by combining dissolution and decomposition. We choose baking because it

is relatively economical and easy to scale up.

For applications in cell-based assay systems, ideal 3D scaffolds should have relatively higher

light transmittance and acceptable mechanical strength. By adjusting the salt/polymer weight

ratio and the amount of paste used for casting, polystyrene scaffolds with various porosities and

thicknesses were fabricated. For example, salt/polymer weight ratios of 20:1, 15:1 and 10:1

resulted in scaffold porosities of 95.3% (Figure 3.2 a), 89.6% (image not shown) and 86.9%

(Figure 3.2 b), respectively. As mentioned before, the 95.3% porosity groups was cast with three

different mixture volume of 70 µl, 100 µl and 150µl, which yielded three scaffold thicknesses of

160 µm (Figure 3.2 c), 200 µm (Figure 3.2 a) and 320 µm (Figure 3.2 d), respectively. The light

transmittance of polystyrene scaffolds under different porosities and thicknesses were

characterized (Figure 3.2 e & f). Scaffold mechanical strength was also evaluated by determining

the capacity to absorb fluid-mechanical energy without damage. The effect of polymer glass

transition was examined by baking the polystyrene scaffolds at a temperature of 100 °C which

was higher than its glass transition temperature. We have adapted the same procedure to

poly-l-lactic acid (PLLA) material and successfully fabricated PLLA scaffolds. For a detailed

comparison between PLLA and polystyrene scaffolds, see Supplemental Material I.

As expected, polystyrene scaffolds with higher porosity and lower thickness exhibited

higher light transmittance and lower mechanical strengths. However, all the samples' mechanical

strength was in the range of 5 mN to 700 mN, which were higher than the maximum possible

force a typical fluid transfer workstation like FlexStation® (Molecular Devices, Sunnyvale, CA)

could generate (0.11 mN). The FlexStation® is a benchtop scanning fluorometer with integrated

fluid transfer workstation, capable of conducting endpoint, kinetic, lambda scan and well scan

experiments in a multi-well plate format. Although the scaffold with 95.3% porosity and 160 µM

thickness had the highest light transmittance and acceptable mechanical strength, its structure

was not uniform; it exhibited abnormally large pores (Figure 3.2 c), suggesting that the paste

mixture was not enough to cover the bottom of the vessel. The scaffold with 95.3% porosity and

320 µm thickness had a porous structure similar to the 200 µm thickness scaffold (Figure 3.2 d).

Considering these factors, we followed the protocol to create scaffolds with 95.3% porosity and

200 µm thickness as the most ideal for cell seeding because they exhibited nearly 80% light

transmittance in wet conditions, acceptable mechanical strength as well as a uniform and intact

porous structure.

3.4.2 NS cell growth profile in 3D scaffolds

The human neural stem (NS) cell (H945RB.3), isolated and developed in Dr. Steve Stice's

lab at the Regenerative Bioscience Center, University of Georgia, was used. Before cell seeding,

both the 3D scaffolds and 2D substrates were coated with poly-ornithine and laminin to rule out

any differences caused by the polymer material itself. Neural spheres were formed by plating

cells into non-coated dishes and incubated under the same conditions as 3D and 2D cultures. As

a commonly studied 3D cellular model, neural spheres provided an in vivo surrogate to be

compared with [1]. Figure 3.3 (a)-(l) shows the images of cells cultured as 2D, 3D and neural

spheres taken on Day 0, Day 5 and Day 10 after plating. Data from Figure 3.3 m& n was fitted

with the growth curve below and the doubling time was calculated:

$$Y = A\, e^{kt}$$

where k is the growth rate, A the number of cells at the start of the experiment and Y is the

number of cells at any time t. It is worth noting that under the same growth conditions, 2D cell

cultures' doubling time was 4.1 days while the 3D and neural sphere cell cultures' doubling times

were 7.7 and 7.9 days, respectively. It is interesting that 3D cultures recreated growth profiles

(Figure 3.3 m empty box) similar to those detected in neural spheres (Figure 3.3 n), whereas NS

cells cultured on standard 2D conditions proliferated much more rapidly (Figure 3.3 m solid square).

3.4.3 Cell morphology

Cell morphology and spatial distribution was examined by Calcein acetoxymethyl ester live cell staining and SEM. After 14 days into culture, NS cells occupied the pores inside the scaffolds (Figure 3.4 a) and developed neurite connections (pink arrows in Figure 3.4 c) between two adjacent cells. Moreover, in the vertical direction, NS cells formed multi-cellular organization (yellow circles in Figure 3.4 d), which is very similar to neural sphere morphology. With the aid of confocal laser scanning microscopy, a color depth projection image (Figure 3.4 g) and a 3D reconstruction image (Figure 3.4 e) were created and confirmed that the NS cells after two days in culture penetrated as deep as 100 µm from the surface toward the inside of the scaffolds. Compared to traditional 2D cultures, cells cultured on 3D scaffolds exhibited lower neurite density (identified as number of neurites per cell) and shorter neurite length. The cell bodies were less spread (more round) than the 2D cultured cells. Moreover, the cells tended to form cell clusters which were not observed on the 2D flat surface. The differences between 2D versus 3D cultures described above suggest that 3D scaffolds may promote cell attachment and differentiation that differs from what was observed with 2D substrates, which is consistent with our previous study [15], in which Wu et al. observed a similar morphological difference phenomenon from human neuroblastoma cells cultured on Cytodex 3 mircobead scaffolds and

flat surfaces. Similar 3D morphogenesis effects also have been observed by other groups. For example, Wang and Good (2001) reported that culturing PC 12 neuron–like cells and SHSY-5Y neuroblastoma cells in a rotating bioreactor resulted in the formation of cell clusters and inhibition of neural extensions [16]. An important feature of the scaffolds is the inter-connected pores, which can host cell clusters formed by the cells seeded into the same pore. It was confirmed in previous studies that cells in multi-cellular organizations significantly differ from cells on flat 2D surface [17].

3.4.4 Cell-matrix adhesion and gene expression

Cellular development, organization and function in tissues are regulated by interactions with a diverse group of macromolecules that comprise the extra cellular matrix (ECM). Focal adhesion kinase (FAK) has been proposed to function as a central mechano-sensing transducer in cells [18]. In particular, phosphorylation of FAK at tyrosine 397 (FAK PY^{397}) in fibroblasts and breast epithelial cells has been demonstrated to be a key signaling event [19]. We utilized an antibody specific for FAK PY^{397} to examine its distribution in undifferentiated NS cells 48 hours after seeding. As observed in Figure 3.5 c, cells cultured on 2D surface demonstrated a streaky pattern of labeling while the localization of FAK PY^{397} for cells on 3D scaffolds was more punctuated and less well-defined (Figure 3.5 d). The FAK PY^{397} labeling observed on 2D conditions is characteristic of localizations at focal adhesions [19]. Loss of FAK PY^{397} localization at focal adhesions has been correlated with morphogenesis and differentiation in 3D

breast epithelial cells [20]. Most notably, Cukierman et al. (2001) reported a loss of FAK PY^{397} staining at adhesion sites and a decrease in the amount of phosphorylated FAK for fibroblasts cultured on cell-free 3D matrices derived either from mouse embryo sections or from naturally deposited 3D ECMs of fibroblast cells [19]. We also utilized microarray gene analysis to analyze the gene expression levels of FAK (gene name: PTK2), and found that the FAK gene in both 3D and neural sphere cultures was down-regulated in comparison to 2D culture (Figure 3.5 i). This was consistent with our immuno-staining results in Figure 3.5 c&d.

Based on our interest in voltage gated calcium channels (VGCC) functionality of NS cells, we also utilized an antibody for L-type calcium channels to examine its expression in 2D and 3D cultures. Both the immuno-staining (Figure 3.5 a & b) and Western Blot results (Figure 3.5 g) showed a decrease in the amount of L-type calcium channels for cells on 3D scaffolds in comparison to their 2D counterparts. These gene and protein expression differences are consistent with voltage calcium channel response magnitude in 3D cultures discussed in the next section. We also utilized microarray to examine the gene expression levels of Interleukin-8 (IL-8) and vascular endothelial growth factor (VEGF) in 3D, 2D and neural sphere cultures as these two genes have been widely reported to be up-regulated in 3D cultures of various cell types [21]. Our results showed an up-regulation of both IL-8 (Figure 3.5 j) and VEGF (Figure 3.5 h) for 3D and neural sphere cultures in comparison to their 2D counterparts.

Structurally VEGF belongs to the VEGF-PDGF (platelet-derived growth factor) super-family [22]. Palmer et al. [23] and Leventhal et al. [24] were some of the first studies to demonstrate the coupling of neurogenesis and angiogenesis. Furthermore, Kaibullina et al. [25]

has provided conclusive evidence suggesting that VEGF affects neural cultures via VEGF receptors (VEGFR1 and VEGFR2).   More recently, Meng et al. [26] has reported that exogenous VEGF has a biphasic effect on expression of endogenous VEGFR1 and VEGFR2 receptors; high doses (500 ng/ml) enhanced neural progenitor cell differentiation while low doses (50 ng/ml) enhanced cell proliferation. This finding is consistent with the gene expression profile reported in Figure 3.5 h as well as the lower proliferation observed in 3D cultures versus 2D cultures (Figures 3.3 m and n). Further studies are needed to explore the differences in VEGF concentration and related receptor expression among 2D, 3D and in vitro or their in vivo surrogate cultures.

3.4.5 Voltage gated calcium channels (VGCC) functionality

To further test the value of using these 3D cell culture vessels in drug discovery programs, we extended our studies to the functionality validation level. VGCC functionality on 2D substrates and 3D scaffolds were compared. VGCC was chosen because it is an emerging drug target — there is a strong link between diseases of the nervous and cardiovascular systems and channel dysfunction [5]. Previous studies done by our group and others have shown differences in calcium currents between intact and dissociated adult mouse SCG cells [27], and differences in voltage gated calcium channel (VGCC) function between 2-D and 3-D cultured human neuroblastoma cells on collagen hydrogels and Cytodex microbead scaffolds [5,6,15]. We simulated the effect of an agonist (drug) by using high K^+ (50 mM) depolarization.

For 3D Petri dishes, single cell bodies were selected as the region of interest (ROI) and the intracellular calcium concentration was recorded continuously in time by the membrane permeable dye Calcium Green-1 acetoxymethyl ester (AM), with a confocal laser scanning microscope. Figures 3.6 a-c and d show typical changes and the time course in terms of Calcium Green-1 AM fluorescence intensity for a responsive NS cell after 2 days' culture in 3D polystyrene scaffolds. A cell was considered responsive only when it showed an increase in fluorescence intensity of 15% or higher over the basal fluorescence intensity level. To extend the study to the HTS level, we utilized Fluo-4 as a calcium indicator and scanned both the 3D and standard 2D 96-well vessels on a FlexStation® fluorescence multi-well plate reader. In this case, each well in the plate comprised of the ROI and a time course of fluorescence changes were recorded (Figure 3.6 e). In both cases, the magnitudes of the response from each cell/well were expressed as a peak fractional increase over basal fluorescence intensity ($F\text{-}Fo)/Fo$, where F is the peak fluorescence intensity and Fo is the basal fluorescence intensity.

For NS cells on 3D dishes, VGCC functionality was characterized before differentiation, one week into differentiation and two weeks into differentiation. Before differentiation, 87.1% and 50.4% of the NP cells on 2D and 3D substrates were responsive to high K^+ buffer, respectively. As shown in Figure 3.6 f, the response magnitude of 3D cultured cells (0.63±0.08) was much lower than that of 2D cultured cells (2.37±0.44) with a p value of 5.33e-7. After one week into differentiation, the percentage of responsive cells on 2D substrates increased to 90.2% with no significant difference in response magnitude of 2.29±0.39 at a 0.05 p level, while 70.2% of cells on 3D were responsive with an average response magnitude increased to 0.72±0.07 ($p = 0.042$).

The 3D cultured cells' response magnitude was still much lower than that of 2D cultured cells (p = 4.88e-6). After two weeks into differentiation, 99.1% of the 2D cultured cells were responsive to high K^+ buffer with a response magnitude decrease to 1.63±0.24 (p = 0.024). Meanwhile, 60.3% of the 3D cultured cells were responsive with the response magnitude of 0.6±0.032. The 3D cultured cells' response magnitude was still much lower than that of 2D cultured cells (p = 5.17e-4). In sum, the 3D culture's VGCC response magnitudes were significantly lower than those from 2D culture at all the three time points. This finding was consistent with previous studies done by our group [5,6,15] as well as by others [19], suggesting that cellular responses observed in 2D are probably exaggerations of in vivo functionality. In other words, NS cells in 3D vessels more closely emulated cells in vivo with respect to the VGCC functionality.

IL-8 is a chemokine that belongs to a group of more than 50 relatively small proteins, 8 - 15 kDa [28] and it achieves its biological action by binding to seven-transmembrane G-coupled receptors named CXCR1 and CXCR2. Puma et al. [29] showed that IL-8 acutely reduces Ca^{2+} currents in identified cholinergic septal neurons expressing CXCR1 and CXCR2 receptors mRNA. As presented in Figure 3 5j, IL-8 gene expression was significantly upregulated in 3D and neural sphere cultures and these cultures also exhibited lower VGCC activity at both the protein and functional levels (Figure 3s. 5g, 6f and g). These results offer a possible explanation for the difference in VGCC function between 2D and 3D cultures. However, further detailed studies are needed to establish profiles of IL-8 concentrations in culture supernatants, related receptors expression, and specific VGCC expression and function.

To further establish the suitability of the 3D 96-well plates for a Calcium FLIPR® Assay

(a popular HTS assay format used in the pharmaceutical industry), we seeded undifferentiated

NS cells onto 3D plates, loaded with calcium indicator Fluo-4 and performed the assay on a

FlexStation® I. Figure 3.6e shows typical time courses for a group of wells of traditional 2D and

3D 96-well plates. A similar pattern of calcium dynamic courses within 3D dishes was observed.

The differences in response magnitude between 2D and 3D plates were consistent with those

between 2D and 3D dishes (Figure 3. 6g). The average response magnitude of cells on 3D

scaffolds was 0.23 ± 0.025, which is lower than that of 2D plates 0.49 ± 0.19 (p=0.00443). It is also

notable that the standard deviation of 3D plates was in an acceptable range (10% of the mean).

This suggested that with further optimization, the quality of HTS assays performed on this new

3D cell-based platform will feasibly meet acceptable industrial standards.

3.5 Conclusion

By integrating 3D polymer scaffolds with standard cell culture vessels, we created a

ready-to-use, robust and highly compatible 3D cell-based assay platform for HTS cell-based

drug discovery programs. The large-scale production of these novel 3D vessels can be achieved

with the standard laboratory automation workstation (liquid handlers such as Beckman Coulter's

Biomek®). Extensive characterization showed that the 3D scaffolds in our vessels exhibited

optical and mechanical properties suitable for current HTS cell-based assay systems. To the best

of our knowledge, it was also the first systematic study to survey the potential applications of 3D

synthetic polymer scaffolds as a more in vivo relevant cell culture/cell-based assay format. Our

results showed that the 3D scaffolds created a proper in vivo-like and biomimetic milieu for NS cells to attach, proliferate and develop in vivo-like functionalities. Compared to cells cultured on standard 2D substrates, cells on 3D scaffolds more closely emulated in vivo surrogates such as neural spheres, with respect to proliferation, morphogenesis, cell-matrix adhesion, and calcium channel activity. Detailed comparisons of those various parameters are summarized in Table 3.1.

The results in this study provide evidence in support of the speculation that cellular responses observed on 2D substrates are probably an exaggeration of in vivo function [19]. Given that many drugs achieve their efficacy by interacting with membrane-integrated ion channels or their associated receptors [30], this result brings attention to the potential importance of introducing the 3D cell-based assay formats into current drug discovery programs. In addition to drug discovery, these 3D vessels also provide an excellent solution for research fields such as toxicology, cancer and stem cell research, development and morphogenesis, and tissue/organ engineering.

Compared to commercially available 3D cell culture systems such as PuraMatrix™ (self assembling nano-fiber scaffolds/hydrogel), AlgiMatrix™ (micro-porous alginate scaffolds) and UltraWeb™ (synthetic nano-fiber scaffolds) cell culture systems, our 3D vessels offer the flowing advantages: First, compared to PuraMatrix™ and UltraWeb™ systems, our 3D vessels offer the necessary spatial dimension (micro-scale pores) to allow formation of cellular aggregates [31]. Second, compared to AlgiMatrix™, our 3D vessels made with synthetic materials (polystyrene) as opposed natural materials offer minimal batch-to-batch variability. Third, the fabrication process for our 3D vessels is amenable to automation with liquid handlers

for fast and precise manufacturing of 3D 96-well or higher density (e.g., 384-well plates). Fourth, use of polystyrene, a common polymer for standard 2D cell culture vessels, is expected to offer material cost advantages. In follow-up studies, similar to those previously conducted with cancer drugs [32,33], we will demonstrate the potential for these vessels to improve clinical efficacy prediction in early stages of drug discovery programs. The cancer drug studies rely on drugs that failed in clinical trials as well as with 3D cell-based systems, but were considered viable hits when initially tested with a 2D cell-based system. We are also extending the current 3D vessels by forming micro/nano hybrid structures expected to better emulate the in vivo micro/nano combination dimensions.

3.6 Acknowledgements

3.7 References

1. Kunz-Schughart LA, Freyer JP, Hofstaedter F, Ebner R. The Use of 3-D Cultures for High-Throughput Screening: The Multicellular Spheroid Model. Journal of Biomolecular Screening. 2004;9:273-285.

2. Bousse L. Whole cell biosensors. Sensors and Actuators. 1996;34:270-275.

3. Abbott A. Biology's new dimension. Nature. 2003;424:870–872.

4. Jessup LM, Godowin TJ, Spaulding GF. Prospects for use of microgravity-based bioreactors to study three dimensional host-tumor interactions in human neoplasia. Journal Cellular Biochemistry. 1993;51:290-300.

5. Desai A, Kisaalita WS, Keith C, Wu ZZ. Human neuroblastoma (SH-SY5Y) cell culture and differentiation in 3-D collagen hydrogels for cell-based biosensing. Biosensors and Bioelectronics. 2006;21:1483–1492.

6. Mao C, Kisaalita WS. Characterization of 3-D collagen gels for functional cell-based biosensing. Biosensors and Bioelectronics. 2004;19:1075-1088.

7. Albrecht DR,Underhill GH, Wassermann TB, Sah RL, Bhatia SN. Probing the role of multicellular organization in three-dimensional microenvironments. Nature Methods.2006;3:369-375.

8. Freed LE, Vunjak-Novakovic G, Biron RJ, Eagles DB, Lesnoy DC, Barlow SK, Langer R. Biodegradable Polymer Scaffolds for Tissue Engineering. Nature Biotechnology. 1994;12:689 – 693.

9. Simon Jr CG, Stephens JS, Dorsey SM, Becker ML. Fabrication of combinatorial polymer scaffold libraries. Review of Scientific Instruments. 2007;78, 0722071-0722077.

10. Zhang S. Beyond the Petri dish. Nature Biotechnology. 2004;22:151-152.

11. Powers MJ, Domansky K, Kaazempur-Mofrad MR, Kalezi A, Capitano A, Upadhyaya A et al. A microfabricated array bioreactor for perfused 3D liver culture. Biotechnology and Bioengineering. 2002;78:257-69.

12. Xu T, Gregory CA, Molnar P, Cui X, Jalota S, Bhaduri SB, Boland T. Viability and electrophysiology of neural cell structures generated by the inkjet printing method. Biomaterials. 2006;27(19):3580-8.

13. Freyman TM, Yannas IV, Gibson LJ. Cellular materials as porous scaffolds for tissue engineering. Progress in Material Science. 2001;46:273-282.

14. Zhang R, Ma PX. Poly (alpha-hydroxyl acids)/hydroxyapatite porous composites for bone-tissue engineering. I. Preparation and morphology. Journal of Biomedical Materials Research. 1999;44:446-455.

15. Wu ZZ, Zhao YP, Kisaalita WS. A packed Cytodex microbead array for three-dimensional cell-based biosensing. Biosensors and Bioelectronics. 2006;22(5): 685-693.

16. Wang SS, Good TA. Effect of culture in a rotating wall bioreactor on the physiology of differentiated neuron-like PC12 and SH-SY5Y cells. Journal Cellular Biochemistry.2001;83:574-84.

17. Kunz-Schughart LA, Kreutz M, Knuechel R. Multicellular spheroids: a three-dimensional in vitro culture system to study tumor biology. International Journal of Experimental Pathology.1998;79:1-23.

18. Wang HB, Dembo M, Hanks SK, Wang Y. Focal adhesion kinase is involved in mechanosensing during fibroblast migration. Proceedings of National Academy of Sciences USA. 2001;98(20):11295-300.

19. Cukierman E, Pankov R, Stevens DR, Yamada KM. Taking cell-matrix adhesions to the third dimension. Science. 2001;294:1708-383.

20. Wozniak MA, Desai R, Solski PA, Der CJ, Keely PJ. Rock generated contractility regulates beast epithelial cell differentiation in response to the physical properties of a three-dimensional collagen matrix. Journal of Cell Biology. 2003;163(3):583-95.

21. Klapperich CM and Bertozzi CR. Global gene expression of cells attached to a tissue engineering scaffold. Biomaterials. 2004;25:5631-5641.

22. Shibuya M. Structure and function of VEGF/VEGF-receptor system involved in angiogenesis. Cell Structure and Function. 2001;26:25-35.

23. Palmer TD, Willhoite AR, Gage FH. Vascular nich for adult hip-pocampal neurogenesis. Journal of Comparative Neurology. 2000;425:479-494.

24. Leventhal C, Rafii D, Shahar A, Goldman SA. Endothelial trophic support of neuronal production and recruitment from the adult mammalian subependyma. Molecular Cell Neuroscience.1999;13:450-464.

25. Khaibullina AA, Rosenstein JM, Krum JM. Vascular endothelia growth factor promotes neurite maturation in primary CNS neuronal cultures. 2004;148:59-68.

26. Meng H, Zhang Z, Zhang R, Liu X, Wang L, Robin AM, Chopp M. Biphasic effects of exogenous VEGF on VEGF expression of adult neural progenitors. Neuroscience Letter. 2006;393(2-3):97-101.

27. Martinez-Pinna J, Lamas JA, Gallego R. Calcium current components in intact and dissociated adult mouse sympathetic neurons. Brain Research.2002;951, 227-36.

28. Matsukawa A, Lukacs NW, Hogaboam CM, Chensue SW, Kunkel SL. III. Chemokines and other mediators, 8. Chemokines and tgeir receptors in cell-mediated immune responses in the lung. Microscopy Research and Technique. 2001;53:298-306.

29. Puma C, Danik M, Quirion R, Ramon F, Williams S. The chemokine interleukin-8 acutely reduces Ca(2+) currents in identified cholinergic septal neurons expressing CXCR1 and CXCR2 receptor mRNAs. Journal of Neurochemistry. 2001;78(5): 960-71.

30. Denyer J, Worley J, Cox B, Allenby G, Banks M. HTS approaches to voltage-gated ion channel drug discovery. Drug Discovery Today. 1998;3:323–332.

31. Angelo-Green J,Yamada KM. Three dimensional microenvironments modulate fibroblast signaling responses. Advance Drug Delivery Review*s* 2007; in press.

32. Anders M, Hansen R, Ding RX, Rauen KA, Bissell MJ, Michael-Korn W. Disruption of 3D tissue integrity facilitates adenovirus infection by deregulating the coxsackievirus and adenovirus receptor. Proceedings of National Academy Sciences USA.2003;100(4):1943-1948.

33. Weaver VM, Petersen OW, Wang F, Larabell CA, Briand P, Damsky C, Bissell MJ.

Reversion of the Malignant Phenotype of Human Breast Cells in Three-Dimensional

Culture and In Vivo by Integrin Blocking Antibodies. Journal of Cell

Biology.1997;137:231-245.
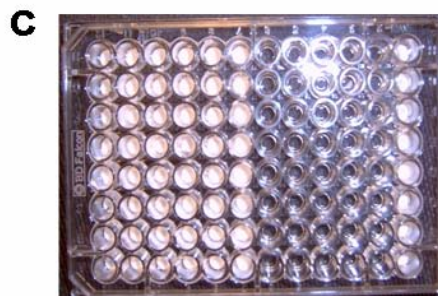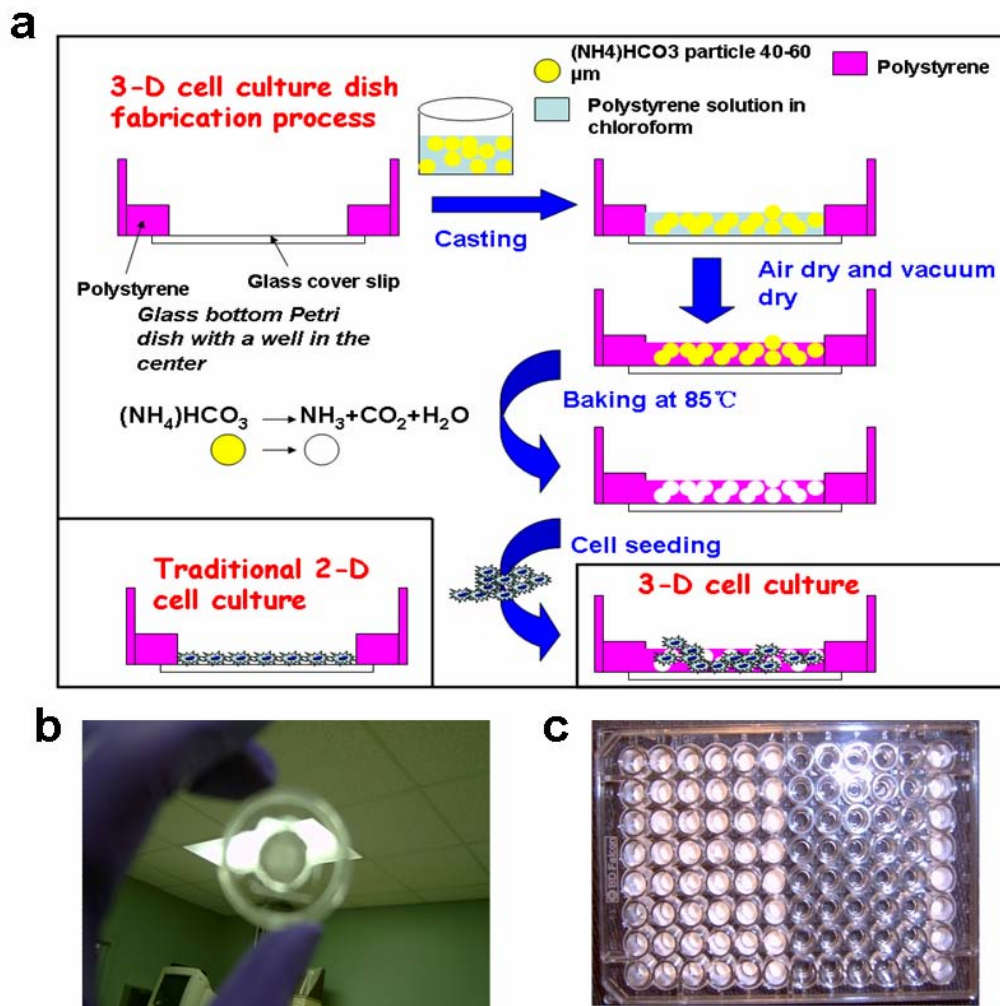
Figure 3.1. Fabrication and characterization of 3D cell culture vessels. (a): Schematic of the

fabrication process. (b): Outlook of a 3D cell culture dish with a 3D polystyrene scaffold in the

center. (c): Outlook of a 3D cell culture 96-well plates with 3D polystyrene scaffolds in the left

half of the columns.
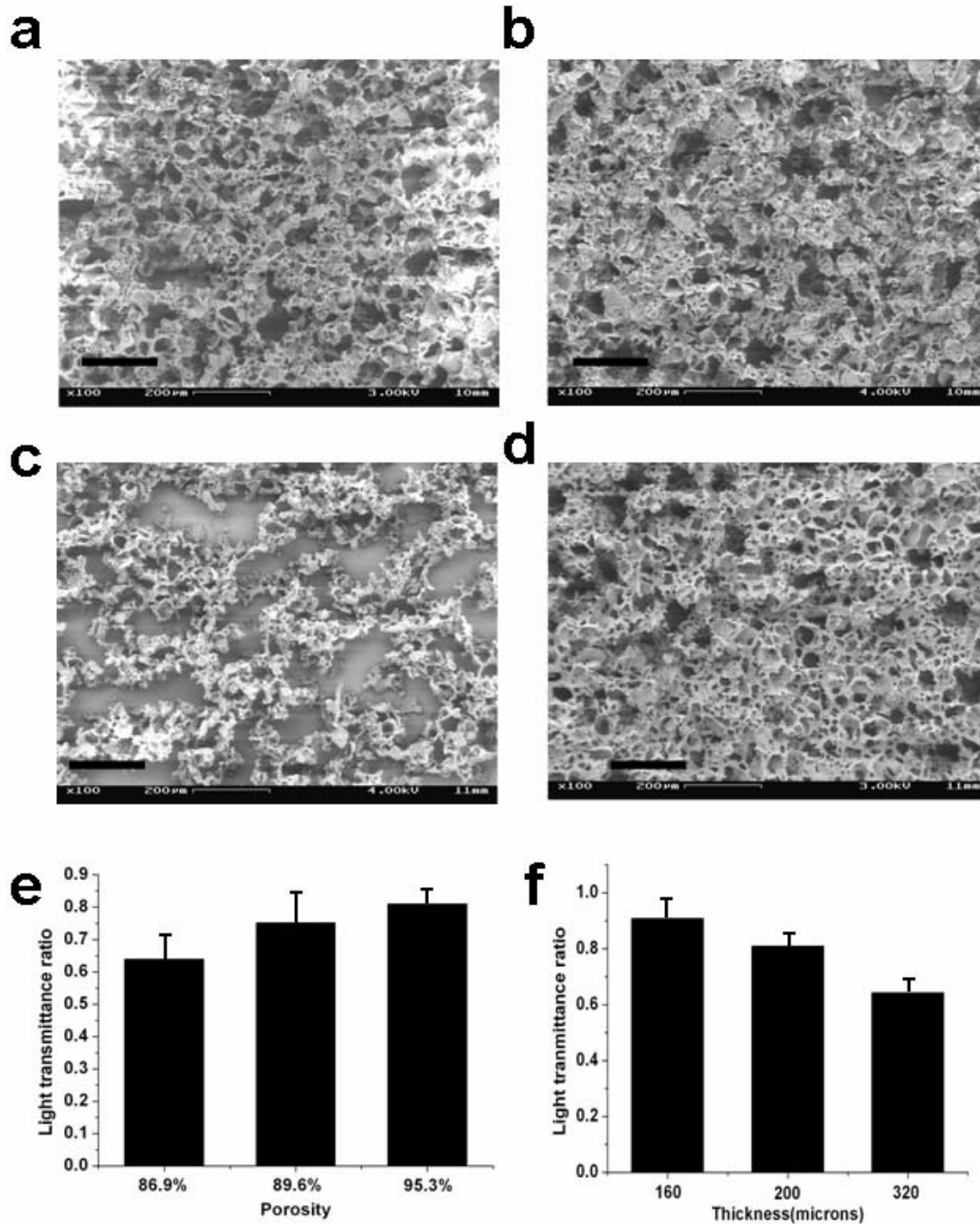
Figure 3.2. Characterization of 3D cell culture Petri dishes. (a) & (b): SEM micrographs of

polystyrene scaffolds with average thickness of 200 µm but different porosities of 95.3% (a) and

86.9% (b). (c) & (d): SEM micrographs of polystyrene scaffolds with average porosity of 95.3%

but different thicknesses of 70 µm (c) and 320 µm (d). (e) & (f): Light transmittance profile of

polystyrene scaffolds with various porosities (thickness = 200 µm) and thicknesses (porosity = 95.3%). All measurements were taken in triplicate from samples prepared independently. Bars represent 200 µm in (a), (b), (c) and (d).

	Day 0	*Day 5*	*Day 10*
3D SEM	a	b	c
3D Fluo.	d	e	f
2D light	g	h	i
Nerual sphere light	j	k	l

m — 2D & 3D Growth Profile

2D cell
3D cell

Total area cover by the cells (a.u.)

dt =4.1
dt =7.7

Day 0   Day 5   Day 10

n — Neural Sphere Growth Profile

sphere volumme (a.u.)

dt =7.9

Day 0   Day 5   Day 10

104
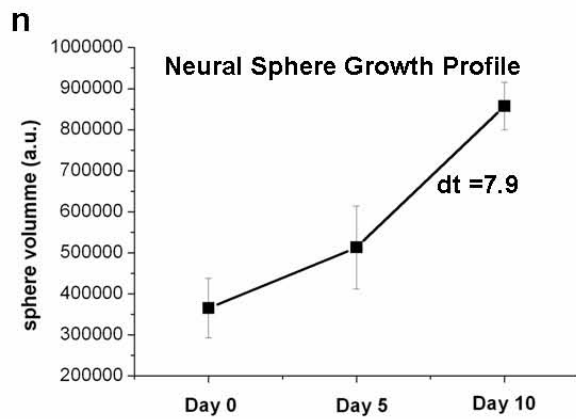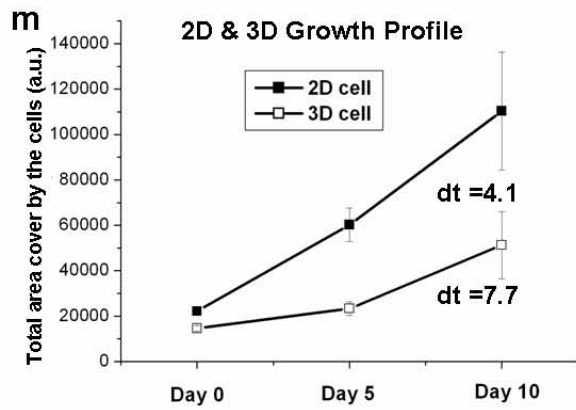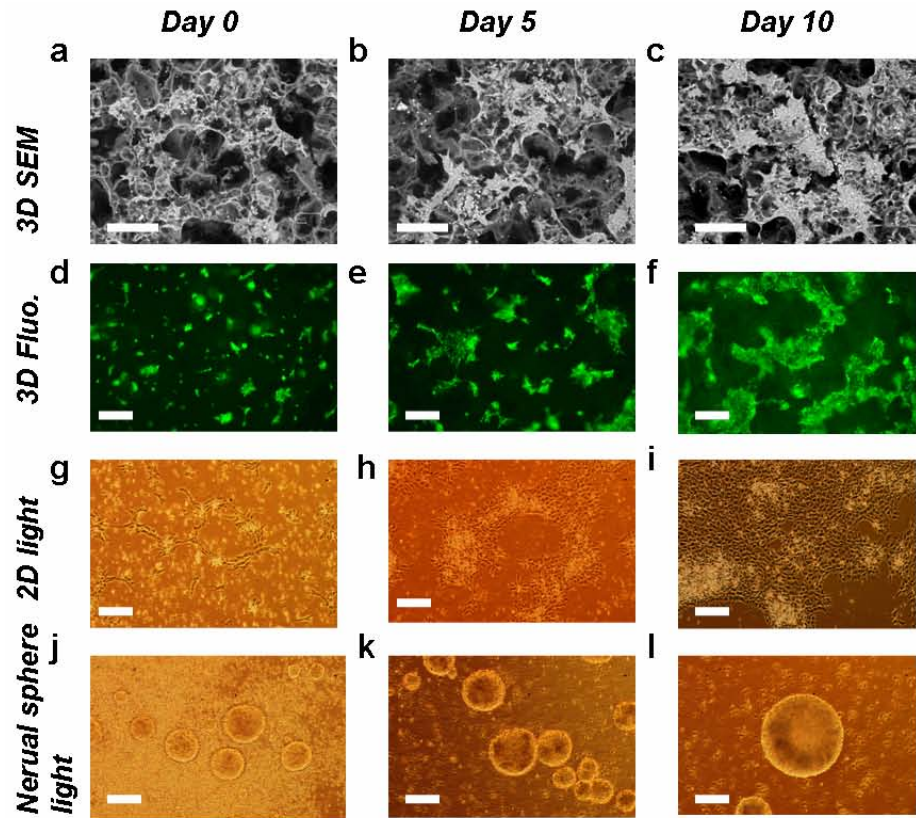
Figure 3.3. Undifferentiated NS cell growth profile. (a), (b), and (c): SEM micrographs of NS cells in 3D scaffolds within Petri dishes on Day 0, Day 5 and Day 10. (d), (e), and (f): Calcein-AM fluorescence images of live NS cells in 3D scaffolds within Petri dishes on Day 0, Day 5 and Day 10. (g) (h) and (i): Phase contrast microscopy images of NS cells on 2D surfaces on Day 0, Day 5 and Day 10. (j), (k) and (l): Phase contrast microscopy images of NS neural spheres on Day 0, Day 5 and Day 10. (m): NS cell growth (proliferation) profile in 3D and 2D cultures. The total area covered by cells in one field was used to estimate the number of cells by assuming a standard spreading area for an individual cell in each culture condition. The total area covered by cells was measured by the SimplePCI 2000 software integrated with the confocal microscope. Eight fields from each specimen across two separate experiments ($n = 16$) were randomly picked and measured. (n): NS cell proliferation profile in neural sphere cultures. Sphere volume was used to estimate the number of cells by assuming a standard volume for an individual cell presented in the spheres. The volume of a neural sphere was calculated by measuring the diameters of spheres with SimplePCI 2000 software. Twenty spheres from one specimen across two experiments were randomly picked and sized for generating one data point ($n = 40$). "dt" stands for doubling time of each condition. Bars represent 20 µm in (a), (b), and (c); and 100 µm in (d) – (l). Error bars are standard deviations.
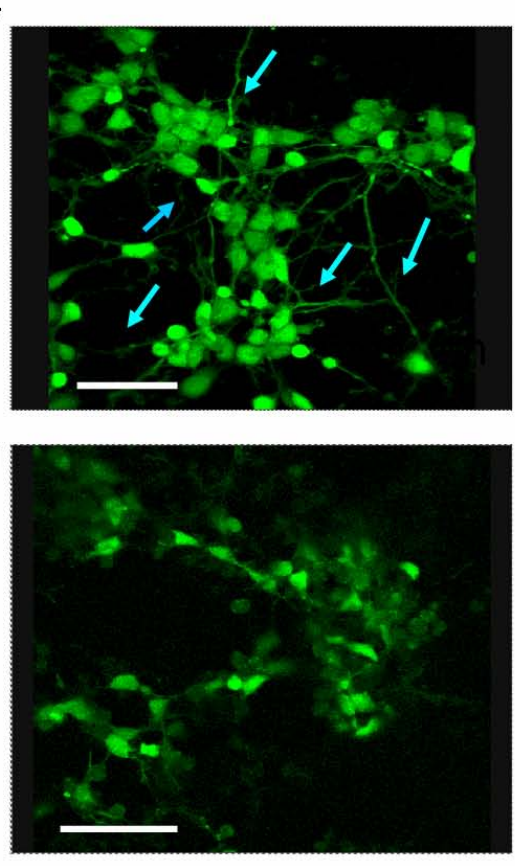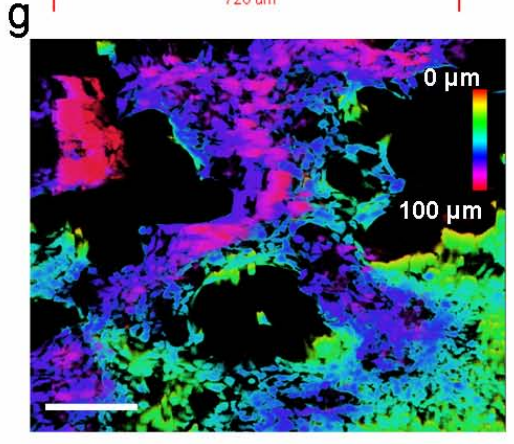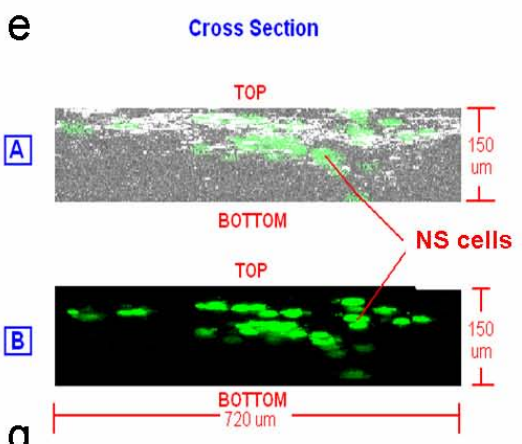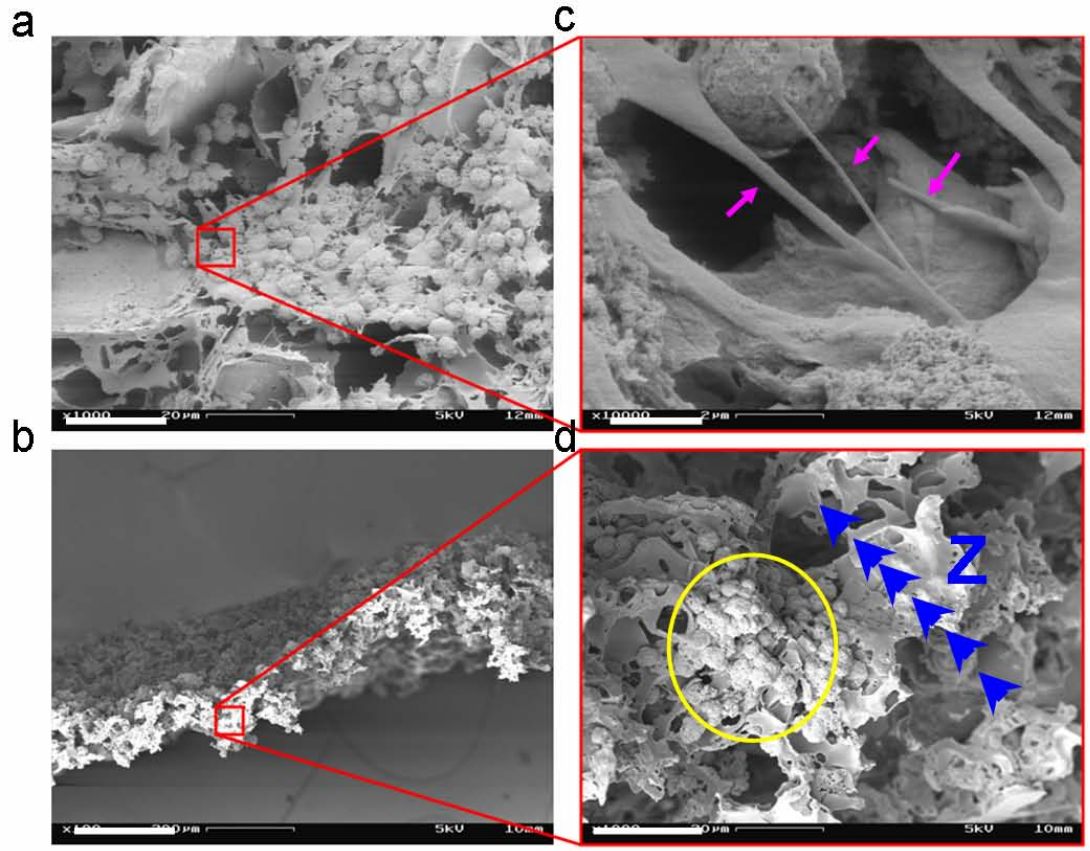
Figure 3.4.   NS cell morphology in 3D scaffolds within Petri dishes. (a), (b), (c) & (d): SEM micrographs of NS cells in 3D scaffolds after 14 days into differentiation. Cells developed well-defined neurites (pink arrows) and formed multi-cellular organizations vertically (yellow circles). (e): Confocal 3D reconstructed micrograph showing the cross section view of a z-scan image montage of NS cells cultured in scaffolds on day 2 after plating. (g). Confocal depth projection micrograph of neural progenitor cells on 3D scaffolds on day 2 after plating. 30 images taken in row by a z-scan were volume rendered. Color corresponds to the depth from the polymer surface, with orange being closest to the surface and red being at 100 µm from the surface. Cells were stained with 5 µM Calcein-AM. (f): & (h): Cells on 2D substrate and 3D scaffolds after 14 days into differentiation. Cells on 2D substrate developed longer neurites (blue arrows) than cells on 3D scaffolds did. Bars represent 20 µm in (a) & (d), 200 µm in (b), 2 µm in (c), 50 µm in (f) & (h), and 100 µm in (g).
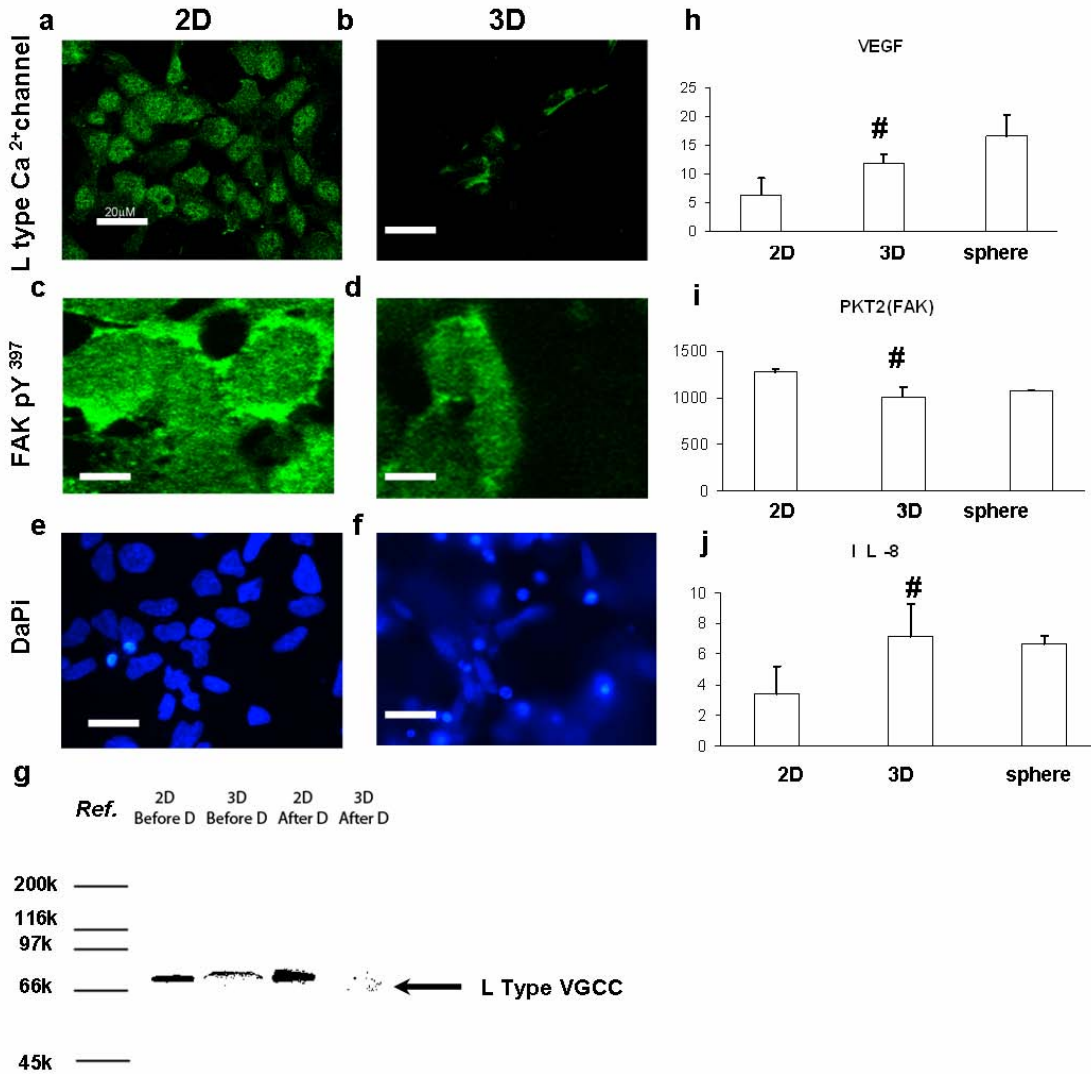
Figure 3.5. Cell-matrix adhesion molecule, growth factor, chemokine, and ion channel expressions. (a) & (b): confocal images of L-type calcium channel staining of NS cells cultured on 2D surface (a) and 3D scaffolds for 2 days. (b). (c) & (d): confocal images of FAK PY^{397} staining of NS cells cultured on 2D surface (c) and 3D scaffolds (d) for 2 days. (e) & (f): fluorescence images of DaPi staining of NS cells on 2D surface (e) and 3D scaffolds (f). (h), (i) and (j) are microarray gene analysis results. Whole genome analysis was performed for NS cells in 2D, 3D and neural sphere after 5 days in culture. Gene expression levels of VEGF (f), PTK2

(FAK) (h) and IL-8 (j) are presented here. The final gene expression levels were averaged from analysis of 4 biological replicates in each culture condition ($n = 4$). Error bars represent the standard deviation. (g): Western Blot of L-type calcium channel protein from NS cells in 2D and 3D cultures before and after introduction into differentiation. # indicates the mean of expression level from 3D cultures was significantly different from that of 2D cultures with $p < 0.05$. Bars represent 20 µm in (a), (b), (e), (f) and 5 µm in (c) & (d).
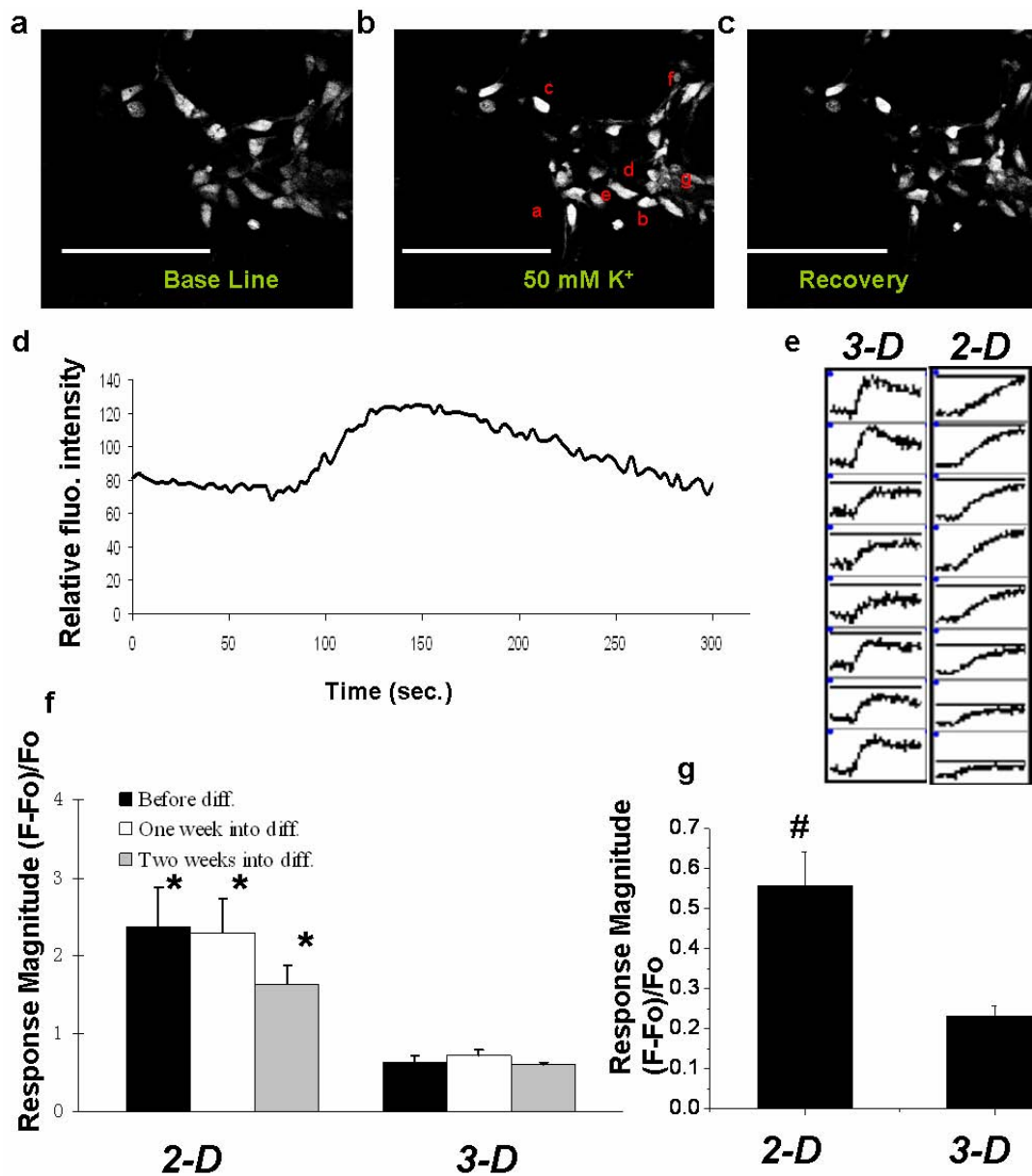
Figure 3.6. VGCC functionality. Cells on 2D/3D Petri dishes and 2D/3D 96-well plates were loaded with calcium indicator Calcium Green-AM and Fluo-4, respectively. The cells were exposed to 50 mM high K^+ depolarization for calcium imaging. (a)–(c): Confocal micrographs of cells on a 3D scaffolds within a Petri dish showing changes in $[Ca^{2+}]$ levels following addition of high K^+ buffer. The elapsed time between (a), (b) and (c) was 30 seconds and 150 seconds. (d) Plot of relative fluorescent intensity versus recording time for a cell labeled "d" in (b). The

increase in fluorescence intensity is proportional to the increase in intracellular $[Ca^{2+}]$ concentration. (e): Typical $[Ca^{2+}]$ time courses of cells from 8 wells in both 2D and 3D culture 96-well plates. (f): High K^+ buffer stimulated VGCC response magnitudes from NS cells cultured on 2D surface and in 3D vessels. Single cell body was selected as the region of interest (ROI) and fluorescence changes were recorded by a time course of laser confocal scanning microscopy. Fifty cells from each specimen across two experiments were selected for calcium imaging ($n = 100$). (g): High K^+ buffer stimulated VGCC response magnitudes from NS cells cultured in 2D and 3D 96-well plates. Time course of fluorescence changes were recorded on a FlexStation®. Assays were performed in triplicate for both 2D and 3D plates ($n = 3$). * indicates that the 2D and 3D response magnitude means compared were significantly different at $p<0.00001$. # indicates that the 2D and 3D response magnitude means compared were significantly different at $p<0.01$. Error bars are standard deviations.

Table 3.1. Summary of differences between 2D, 3D and in vivo surrogate cells.

"+" denotes up-regulated genes, highly-expressed proteins, or higher cellular activities in comparison to the groups marked with "-".

	2D Cells	3D Cells	In vivo surrogates
Proliferation	+	-	-
FAK gene expression	+	-	-
IL-8 gene expression	-	+	+
VEGF gene expression	-	+	+
L-type Calcium Channel protein	+	-	n/a
VGCC activity	+	-	n/a

CHAPTER 4

THREE DIMENSIONAL NEURONAL CELL CULTURE MODEL CALCIUM

CHANNEL FUNCTIONALITY*

4.1 Abstract

Three-dimensional (3-D) cell-based assay systems are desirable in accelerated drug

discovery for high throughput screening (HTS) applications because of their potential similarity

to in vivo environment [1]. Many whole-cell-based assays in use today rely on flat,

two-dimensional (2-D) glass or plastic substrates that may not produce results characteristic of in

vivo conditions. Although numerous studies have compared cells from 2-D and 3-D

microenvironments, to the authors' knowledge, none has attempted to answer the question

whether 3-D cellular responses are identical to in vivo responses at the functional level. The

purpose of this study was to investigate how well neuronal cells in vitro model in vivo

functionality with respect to voltage gated calcium channels (VGCC). VGCC were chosen

because they are emerging drug targets — there is a link between diseases of the nervous and

cardiovascular systems and channel dysfunction [2]. Mouse superior cervical ganglion (SCG)

cells were harvested and cultured on the 3-D scaffolds [3] made from poly-l-lactic-acid (PLLA)

and 2-D glass substrates, both coated with collagen. We found that the cell morphology and

VGCC function from cells on 3-D scaffolds more closely modeled intact SCG tissues in

comparison to cells on 2-D cover slips. Intracellular calcium increase in response to high

potassium depolarization was identical between 3-D cultured and intact SCG tissue cells, but

significantly different between 3-D and 2-D cultured cells. This result provides the first evidence

in support of the hypothesis that some cellular responses under traditional 2-D environment may

be exaggerated [4].

4.2 Introduction

A key goal in cell-based assay technology today is to achieve cellular responses to external

stimuli that are physiologically relevant or mirror what happens in vivo as closely as possible.

Three dimensional (3-D) cell culture provides cells with characteristic topographical cues and

thus enables cells to differentiate into specific phenotype and maintain specific functions that are

usually impossible under two dimensional (2-D) cell culture conditions [5, 6]. Ideal cell-based

assay systems call for research efforts to create three-dimensionality so that cellular responses

will be more representative of those under in vivo conditions.

Various methods and materials have been studied for creating three dimensionality. Among

them are microgravity bioreactors [7, 8], natural polymers especially collagen hydrogels [9-11],

photopolymerized hydrogels [12], synthetic polymer scaffolds [3, 13], self-assembling peptide

scaffolds [14], and micro/nano patterned substrates [15].

Synthetic polymer scaffolds offer several comparative advantages. First, in comparison to microgravity bioreactors and patterned substrates, polymer scaffolds are easier and faster to prepare and can be scaled down for incorporation into HTS systems. Second, in comparison to most hydrogels, polymer scaffolds offer less resistance to diffusion of nutrients and wastes to and from cells deeper in scaffold [10]. Third, in comparison to nano-scale pores and fibers associated with self-assembling peptide scaffolds, micro-scale pores on polymer scaffolds are large enough to host multi-cellular organisms which are observed in tissue engineering studies [16].

The purpose of this study was to investigate how well neuronal cells cultured in vitro model in vivo functionality with respect to voltage gated calcium channels (VGCC). Mouse SCG cells were harvested and cultured on the 3-D scaffolds made from poly-l-lactic-acid (PLLA) and 2-D glass substrates, both coated with collagen. The morphology and VGCC functionality from cells cultured on 3-D were compared with that from 2-D cultured cells. As an *in vivo* surrogate, intact SCG tissue was used as the golden standard to be compared with.

4.3 Materials and methods

4.3.1 Scaffold fabrication

3-D Scaffolds were fabricated by the gaseous salt leaching method [25]. Briefly, a highly viscous polymer solution was prepared by dissolving PLLA polymer particles in chloroform. Ammonium bicarbonate salt particles were added to the PLLA solution and mixed thoroughly. Sieved ammonium bicarbonate particles in the range of 40-60 µm in diameter were used. Salt

particles in this size range generated pores with an average diameter range of 60-100 µm. The

paste mixture of polymer/salt/solvent was cast into a glass Petri dish. After chloroform was

partially evaporated under atmospheric pressure, the semi-solidified samples were immersed into

boiling water until no gas bubbles were generated. The samples were vacuum dried for 24 h and

kept in desiccators until use. Before cell plating, the scaffolds were pre-wetted and sterilized in

70% ethanol under UV over night and then rinsed with PBS three times. The scaffolds were

coated with collagen by incubating in 0.1 mg/ml collagen solution for 2 h, followed by air drying

at room temperature.

4.3.2 Scaffold characterization

The porosities of the polymer scaffolds were measured by a modified liquid displacement

method [26] with ethanol as the displacement liquid. Scaffold mechanical strength was evaluated

by determining the capacity to absorb fluid-mechanical energy without damage [10]. A syringe

pump (Orion, Boston, MA), connected to a standard 200 µl pipette tip, was used. De-ionized

water was perpendicularly pumped onto the surface of polymer scaffolds for 5 s through the tip.

The flow rate inducing scaffolds rupture was recorded. The force, F, experienced by the

scaffolds was calculated as follows:

$F = \rho \cdot A \cdot v^2$

where ρ is the density of the de-ionized water, A the area of the opening of the pipette tip

and v is the fluid flow rate just before impact, which depends on the rate of the syringe piston

movement and the diameter of the nozzle tip. Light transmittances of polymer scaffolds were measured by an inverted microscope (TE3000, Nikon) coupled to a digital camera (D100, Nikon). Images taken with the same lamp power and exposure time were processed with SimplePCI 2000 software. The light transmittance ratio was calculated by dividing the sample mean grey level from three different spots by the control grey level (flat cover slips).

4.3.3 Scanning electron microscopy (SEM)

Cells on scaffolds were fixed with 2% glutaraldehyde in 0.1 M sodium cacodylate buffer (pH 7.2) for 1 h and then rinsed in cacodylate buffer three times (15 min each). This was followed by post-fixing with 1% OsO_4 in 0.1 M sodium cacodylate buffer for 1 h and rinsing in cacodylate buffer three times (5 min each). The samples were then dehydrated in 35, 50, 70, 80, 95 and 100% ethanol successively for 10 min each and dried in a SAMDRI-780A critical point drier (Tousimis Research Corporation, MD). Scaffolds were sputter-coated with gold for 60 s to achieve a thickness of about 15.3 nm. SEM images were captured with LEO 982 scanning electron microscope (LEO Electronenmikroskopie GmbH Korporation, Germany) with an acceleration voltage of 4 kV. A similar protocol was followed for scaffold samples without cells, with the exception that the preparation started with sputter coating.

4.3.4 SCG cell harvesting and plating

Neonatal mice (CD1) were used as the sources of SCG nerve cells. A mice SCG dissection protocol [27] described elsewhere was followed. All the animals received the standard care in compliance with the Animal Welfare Act and under the University of Georgia Animal Usage Proposal. After dissection, the ganglions were enzymatically digested in 1 mg/ml type IA collagenase for 1 hour. After gentle mechanical disruption with a Pasteur pipette, dissociated cells and cell chunks were plated into glass bottom Petri dishes (MatTek, MD) and PLLA scaffolds, both of which were coated with 0.1 mg/ml type I collagen. On the average, cells from two ganglions were plated to each dish or scaffold. Cells were maintained in Eagle's Minimum Essential Medium supplemented with 2 mM L-Glutamine, 1 mM Sodium Bicarbonate, 10% FBS, and 50 ng/ml NGF. The cells were incubated at 37 °C in a 10% CO_2 humidified atmosphere. To prepare intact SCG tissue samples to facilitate the staining process, the outer sheath covering the freshly dissected ganglions was broken with fine forceps.

4.3.5 VGCC functionality characterization

Calcium imaging experiments were performed after 2-day and 7-day incubation for both the 2-D and 3-D cultured cell samples. To best represent the in vivo condition, intact SCG tissues were stained right after the dissection which was followed by the calcium imaging. The time between dissection and recording was around one hour. Intracellular calcium dynamics were recorded using the membrane permeable dye Calcium Green-1 AM coupled with confocal laser

scanning microscopy. 2-D cultured cells on the Petri dish were washed twice with HEPES

buffered saline (HBS) and loaded with 5µM dye in 1 ml of HBS containing 3% FBS and 0.02%

Pluronic F-127. The Petri dishes were incubated at 37 °C for 30 min. After dye loading, cells

were rinsed with HBS twice and retuned to the incubator for another 30 min to allow complete

dye de-esterification. A similar protocol was followed for 3-D and intact SCG tissue samples.

However, the dye concentration was increased to 10 µM to facilitate dye loading. Both the

scaffold and intact SCG tissue were fixed by a small cover slip in the solution during the calcium

imaging. Calcium Green-1 was excited with 488 nm argon laser and the fluorescence intensity

was recorded through a 515 nm long Pass filter. Cells were depolarized by adding 100 µl of high

potassium buffer to a final concentration of 50 mM K^+ while imaging. The intracellular calcium

dynamics were reflected by changes in intracellular Calcium Green-1 fluorescence intensity.

4.3.6 Statistical analysis

Neurite length, soma section area, soma section roundness and calcium response magnitude

values were expressed as mean ± standard deviation (S.D.). The unpaired Student's *t*-test was

used to compare the means of two samples. The *p* values are indicated in the text and decisions

regarding significant difference were based on level of 0.05.

4.4 Results and discussion

4.4.1 PLLA scaffolds

In this study, Poly-l-lactic-acid (PLLA) porous scaffolds with equivalent average pore sizes of 60-100 µm in diameter were fabricated. Through trial and error, this pore size range was found to be ideal for mouse SCG cells, which are approximately 10 µm in diameter. Smaller pores prevented cell intrusion, while larger pores made cell-matrix interaction identical to 2-D conditions. Similar observations have been reported by others [16].The porosity of resulting scaffolds ranged between 88.4% and 95.6%, and the pores were inter-connected to each other (Figure 4.1 a & b). For cell-based assay applications, ideal scaffolds should have both acceptable light transmittance and mechanical strength.   The light transmittance and mechanical strength under different scaffold porosity and thickness were characterized (Figure 4.1 c & d). As expected, scaffolds with higher porosity and lower thickness exhibited better light transmittance but poorer mechanical strength. In addition, all the scaffolds exhibited around 30% increases in light transmittance after wetting with PBS. All the four samples' mechanical strength was higher than the maximum possible force a typical fluid transfer workstation (e.g. FLEXstation, Molecular Devices, Sunnyvale, CA) could generate (0.11 mN). The "20:1 thin" scaffold exhibited the highest light transmittance in both dry and wet conditions. However, because of its thinness, it tended to lose shape on removal from solution. This problem might be addressed by fixing the scaffold on a rigid glass surface in the future. Considering the factors above, we chose

the 20:1 scaffolds as our samples for cell seeding because they exhibited nearly 80% light transmittance in wet condition, in addition to reasonable mechanical strength.

4.4.2 SCG cell morphology

We chose neuronal cells from superior cervical ganglion (SCG) because in our previous studies [9, 10, 17] we have used neuroblastoma cells which were considered as a model for peripheral sympathetic cells. The CD1 mouse strain was chosen because this strain has been extensively used in toxicological and functional studies as an acceptable model for human medicine applications. SCG cells were harvested from the animals on postnatal day 7 and seeded onto the 3-D scaffolds and 2-D substrates (cover slips) both coated with 0.1mg/ml Type I collagen from rat tail, to rule out any differences caused by the material itself. Cell viability and spatial distribution was examined by Calcein acetoxymethyl ester (AM) live cell staining, coupled with confocal microscopy, on day 7 after plating (Figure 4.2 c). Cells were viable with well developed neurites, and intruded as deep as 150µm from the top of the scaffold, which further confirmed that the pores inside the scaffolds were interconnected and had formed open channels to allow cell migration in all directions. SEM images also showed that cells formed multi-cellular clusters inside the pores on the scaffold (Figure 4.2 a) and had developed neurite inter-connections between adjacent cells (Figure 4.2 b).

Cell morphology was further investigated by confocal microscopy images taken with higher magnification (64X) oil lens and quantitative cell morphology measurements were processed by

SimplePCI 2000 software. Detailed results are presented in Table 4.1.   We used neurite density

(the number of neurites per cell), neurite length, cell soma section area & roundness to

characterize the cell morphology. Roundness was an estimated circularity shape factor calculated

as: 4*Pi*area/perimeter^2. On day 2 after plating, a few cells on 3-D scaffolds had already

developed short neurites and most cells were still round (Figure 4. 3d). Compared to the cells on

2-D substrates (Figure 4. 3a), 3-D cell neurite density was lower (0.7 v.s. 2.4), and the neurites

were shorter ($10.9\pm3.2\mu$m v.s. $38.9\pm17.7\mu$m, p=7.88e-7). In comparison to that on 2-D substrates,

cells on 3-D scaffolds spread poorly with smaller cell soma section area ($90.0\pm22.3\mu$m^2

v.s.$149.8\pm59.3\mu$m^2, p=4.56e-6) and larger soma section roundness (0.81 ± 0.05 v.s. 0.51 ± 0.11,

p=1.16e-15). In addition, a number of cells were found forming clusters which was not observed

in 2-D cells. On day 7 after plating, more neurites were observed among both 2-D and 3-D cells

(Figure 4. 3b and 3e), with increased neurite lengths of $63.6\pm36.1\mu$m (p=5.75e-10) and

$25.2\pm13.8\mu$m (p=0.001) respectively. The spreading condition for cells on 2-D remained

unchanged with comparable cell soma section area and roundness to the day 2 cells. However,

the cells on 3-D scaffolds were more spread with larger soma section area ($144.5\pm56.9\mu$m^2,

p=1.03e-4) and had lower roundness (0.64 ± 0.15, p=7.89e-6). The significant morphological

difference between 2-D and 3-D cells observed on day 2 still existed among day 7 cells.

From the above observations, it can be concluded that cells on 3-D scaffolds developed

shorter neurites and were less spread than the 2-D cultured cells. The 3-D cultured cell

morphology more closely mimicked the cell morphology found in freshly dissected intact SCG

tissue (Figure 4. 3g). The above differences between 2-D versus 3-D cultured cells suggest that

polymer scaffolds are a unique substrate that promotes cell attachment and differentiation that differs from what was observed with 2-D substrates, which are consistent with conclusions from our previous studies [9, 10, 17].

Similar 3-D effects have been observed in other studies. Wang and Good reported that culturing PC 12 neuron–like cells and SHSY-5Y neurablastoma cells in a rotating bioreactor resulted in formations of cell clusters and inhibition of neural extensions [18]. Wu and others observed the similar phenomenon from SHSY-5Y cells cultured on Cytodex 3 mircobead scaffolds [17]. Furthermore, Webb and others found changes in extra-cellular matrix (ECM)-related gene expression consistent with decreasing cell migration and increasing tissue formation when fibroblast cells were transferred from 2-D to 3-D culture on porous Tecoflex-derived biomaterials [19], which is similar to the PLLA scaffolds we used in this study.

Some topography features of the PLLA scaffolds may contribute to the differences between 2-D and 3-D cultures. One major feature is the pore surface curvature which plays an important role in cell spreading and adhesion. Curvature radius less than 100 µm compromises cell spreading and attachment along the bending direction and form the basis of contact guidance along the cylindrical substrata [20]. In our case, the pore curvature radius was less than 50 µm which is small enough to produce topographical effects. Another important feature is the inter-connected pores, which can host cell clusters formed by the cells seeded into the same pore. Cells in multi-cellular organizations significantly differ from cells on flat 2-D surface [21]. To further confirm the value of PLLA scaffold in modeling in vivo conditions, we extended our comparative investigation to the functional level.

4.4.3 VGCC functionality comparison

Previous studies done by our group and others have shown differences in calcium currents between intact and dissociated adult mouse SCG cells [22], and difference in voltage gated calcium channels (VGCC) function between 2-D and 3-D cultured human neuroblastoma cells on collagen hydrogels and cytodex microbead scaffolds [9, 10, 17]. We reasoned that comparing VGCC functionality as reflected by calcium influx in response to high K^+ (50 mM) depolarization is a convenient first step in addressing 3-D and in vivo similarities. The intracellular calcium concentration was recorded continuously in a time course by the membrane permeable dye Calcium Green-1 acetoxymethyl ester (AM) coupled with a confocal laser scanning microscope. Figure 4.3 shows the typical time course changes in Calcium Green-1 AM fluorescence intensity for a responsive cell upon stimulation with high K^+ on 2-D substrates (c), 3-D scaffolds (e) and intact SCG tissue (h). A cell was considered responsive only when it showed an increase in fluorescence intensity of 15% or higher over the basal fluorescence intensity level. The magnitudes of the response from each cell were expressed as a peak fractional increase over basal fluorescence intensity (*F-Fo)/Fo*, where *F* is the peak fluorescence intensity and *Fo* is the basal fluorescence intensity. The percentage and magnitude of cellular VGCC responses to high K^+ depolarization within cells on 2-D substrates, 3-D scaffolds and intact SCG tissues are summarized in Figure 4. 4.

On day 2 after plating, 62.3% and 47.9% of cells on 2-D substrates and 3-D scaffolds respectively, were responsive to high K^+ HBS buffer. The 3-D cultured cells' response magnitude was 0.26±0.08, which is much lower than the 2-D cultured cells' response magnitude of 0.75±0.54 (p=0.0012). On day 7 after plating, the percentage of responsive 2-D cultured cells increased to 100% as all the 28 cells measured had response to high K^+ buffer, with the response magnitude increasing to 0.84±0.32 although the difference was not statistically significant (p=0.43). The percentage of responsive cells on 3-D scaffolds increased to 75.8% with the response magnitude increasing to 0.34±0.14 (p=0.01). As with results on day 2, the response magnitude of cells on 3-D scaffolds on day 7 was still significantly lower than that of cells on 2-D substrates (p= 7.40e-7). It was interesting to observe that both the response magnitudes of 3-D cells on day 2 and day 7 were not significantly different from that of cells in intact SCG tissue, which was 0.30±0.11 from 25 responsive cells from a pool of 41 cells (p=0.88 and 0.80 respectively). Assuming that the cells in intact SCG tissue were not very different from cells in vivo, this observation provides the first evidence in support of the speculation that cellular responses observed in 2-D is probably an exaggeration of in vivo function [4]. We are comfortable with the above assumption for several reasons. First, we made every effort to minimize the time between dissection and recording (below 60 min) and we maintained the tissue under physiological conditions (HEPES Buffer Saline with 3% Fetal Bovine Serum). Second, our approach is similar to investigations that utilize brain slices [23] and other peripheral nerve tissues [24], where in vivo similarity is well accepted.

4.5 Conclusion

In conclusion, porous PLLA scaffolds created a proper three dimensionity for cells to attach and differentiate. The neonatal mouse SCG cells cultured on 3-D scaffolds more closely mimicked the cells in intact SCG tissue than those cultures on 2-D substrates. Given that many drugs achieve their efficacy by interacting with membrane-integrated ion channels or their associated receptor-ligand behavior [2], this result brings attention to the potential importance of introducing three dimensional cell-based assays in drug discovery programs. In addition to the large diversity of physiological parameters as well as drug induced responses that need to be characterized with 3-D cultured cells, future work may involve the exploration of other types of biocompatible polymers and their composites for scaffold fabrication. While primary cultured neurons are ideal for confirming in vivo-in vitro similarities, unfortunately, their preparation is time consuming and is not suitable for HTS due to the limited quantities available. Embryonic stem cells and neural progenitor cells are better substitutes, as they are normal cells which can be cultured to meet the large scale application in an HTS cell-based assay.

4.6 Acknowledgements

4.7 References

1. Abbott A. Biology's new dimension. Nature. 2003:424:870-872.

2. Denyer J, Worley J, Cox B, Allenby G, Banks M. HTS approaches to voltage-gated ion channel drug discovery. Drug Discovery Today. 1998;3: 323-332.

3. Mikos AG, Sarakinos G, Leite SM, Vacanti JP, Langer R. Laminated three dimensional biodegradable foams for use in tissue engineering. Biomaterials. 1993;14:323-330.

4. Cukierman E, Pankov R, Stevens DR, Yamada KM. Taking cell-matrix adhesions to the third dimension. Science. 2001;294:1708-1712.

5. Mueller-Klieser W. Three-dimensional cell cultures: from molecular mechanisms to clinical applications. AJP - Cell Physiology. 1997;273:C1109-C1123.

6. Weaver VM, Petersen OW, Wang F, Larabell CA, Briand P, Damsky C, Bissell MJ. Reversion of the malignant phenotype of human breast cells in three-dimensional culture and in vivo by integrin blocking antibodies. Journal of Cell Biology.1997;137:231-245.

7. Lewis ML, Moriarity DM, Campbell PS. Use of microgravity bioreactors for development of an in vitro rat salivary gland cell culture modal. Journal Cellular Biochemistry. 1993;51:265-273.

8. Jessup LM, Godowin TJ, Spaulding GF. Prospects for use of microgravity-based bioreactors to study three dimensional host-tumor interactions in human neoplasia. Journal Cellular Biochemistry. 1993;51:290-300.

9. Desai A, Kisaalita WS, Keith C, Wu ZZ. Human neuroblastoma (SH-SY5Y) cell culture and differentiation in 3-D collagen hydrogels for cell-based biosensing. Biosensors and Bioelectronics. 2006;21:1483–1492.

10. Mao C, Kiaalita WS. Characterization of 3-D collagen gels for functional cell-based biosensing. Biosensors and Bioelectronics. 2004;19:1075-1088.

11. O'Connor, S.M. et al. Immoblizaiotn of neural cells in three-dimensional matrices for biosensor application. Biosensors and Bioelectronics. 2000;14: 871-881.

12. Albrecht DR,Underhill GH, Wassermann TB, Sah RL, Bhatia SN. Probing the role of multicellular organization in three-dimensional microenvironments. Nature Methods. 2006;3:369-375.

13. Freed LE et al. Biodegradable Polymer Scaffolds for Tissue Engineering. Nature Biotechnology. 1994;12:689-693.

14. Zhang S. Beyond the Petri dish. Nature Biotechnology. 2004;22:151-2.

15. Powers MJ, Domansky K, Kaazempur-Mofrad MR, Kalezi A, Capitano A, Upadhyaya A, Kurzawski P, Wack KE, Beer Stolz D, Kamm R, Griffith LG. A microfabricated array bioreactor for perfused 3D liver culture. Biotechnology and Bioengineering. 2002;78(3):257-269.

16. Freyman TM, Yannas IV, Gibson LJ. Cellular materials as porous scaffolds for tissue engineering. Progress in Material Science. 2001;46:273-282.

17. Wu ZZ, Zhao YP, Kisaalita WS. A packed Cytodex microbead array for three-dimensional cell-based biosensing. Biosensors and Bioelectronics.2006;22:685-693.

18. Wang SS, Good TA. Effect of culture in a rotating wall bioreactor on the physiology of differentiated neuron-like PC12 and SH-SY5Y cells. Journal Cellular Biochemistry. 2001;83:574-84.

19. Webb K et al. Comparison of human fibroblast ECM-related gene expression on elastic three-dimensional substrates relative to two-dimensional films of the same material. Biomaterials. 2003;24(25):4681-90.

20. Dunn GA, Heath JP. A new hypothesis of contact guidance in tissue cells. Experimental Cell Research. 1976;101:1-14.

21. Kunz-Schughart LA, Kreutz M, Knuechel R. Multicellular spheroids: a three-dimensional in vitro culture system to study tumor biology. International Journal of Experimental Pathology. 1998;79:1-23.

22. Martinez-Pinna J, Lamas JA, Gallego R. Calcium current components in intact and dissociated adult mouse sympathetic neurons. Brain Research. 2002;951:227-36.

23. Steriade M. The Intact and Sliced Brain. MIT Press, Cambridge, MA (2001).

24. Saino T, Satoh Y. Application of real-time confocal laser scanning microscopy to observe living cells in tissue specimens. Journal of Electron Microscopy. 2004;53:49-56.

25. Nam YS, Yoon JJ, Park TG. A novel fabrication method of macroporous biodegradable polymer scaffolds using gas foaming salt as a porogen additive. Journal of Biomedical Materials Research. 2000;53:1-7.

26. Zhang R, Ma PX. Poly (alpha-hydroxyl acids)/hydroxyapatite porous composites for bone-tissue engineering. I. Preparation and morphology. Journal of Biomedical Materials Research. 1999;44:446-455.

27. Mains RE, Patterson PH. Primary Cultures of dissociated sympathetic neurons: I. Establishment of long-term growth in culture and studies of differentiated properties. The Journal of Cell Biology. 1973;59:329-345.
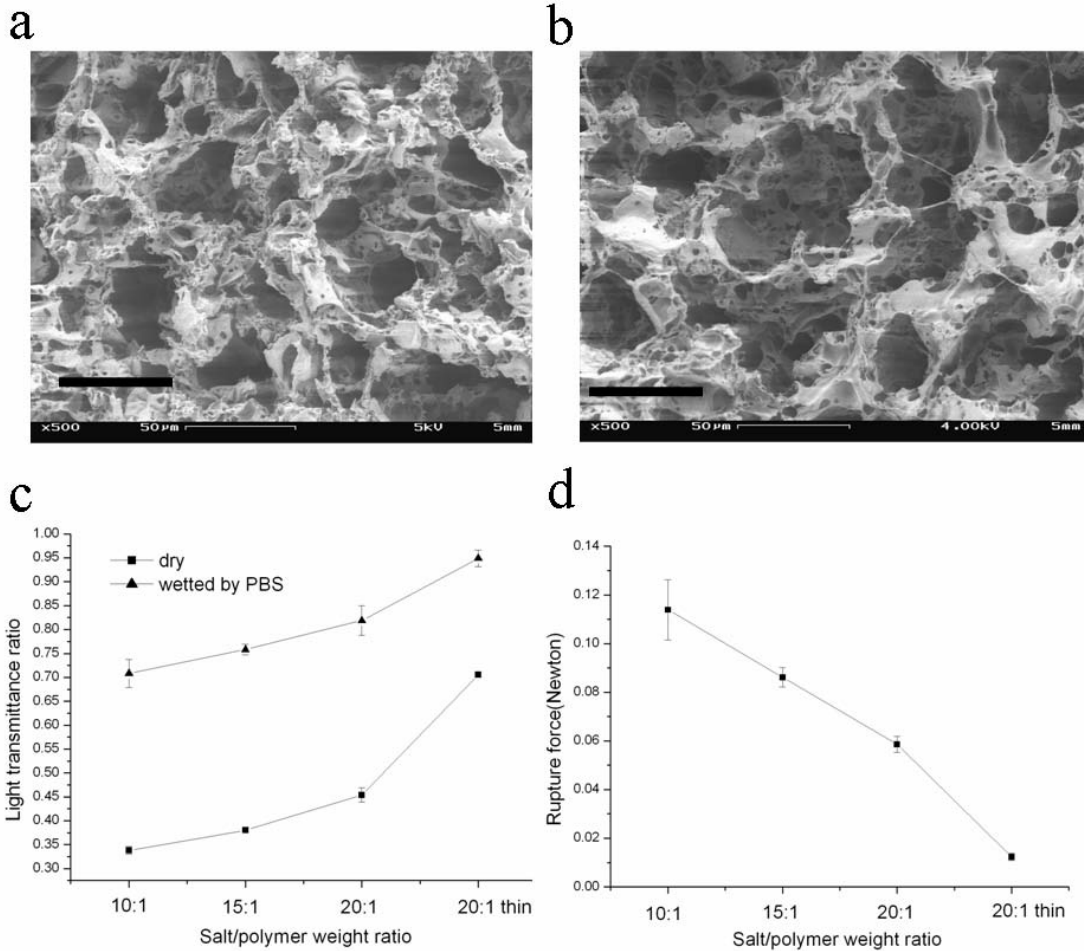
Figure 4.1. (a) & (b): PLLA scaffold SEM micrographs with 88.4% (a) and 95.6% (b) porosity.

Bar represents 50µm in both two images. (c) & (d): Light transmittance and mechanical strength

of PLLA scaffolds. The ratios 10:1, 15:1 and 20:1 represent the weight of pore forming salt to

PLLA, which resulted in average porosity of 88.4%, 92.8% and 95.6% respectively. The scaffold

thicknesses were 400µm for all scaffolds with the exception of "20:1 thin" which was 150 µm.

The rupture force in d represents the fluid impact force which caused the rupture of the scaffolds.

All measurements were taken in triplicate from samples prepared at different times.
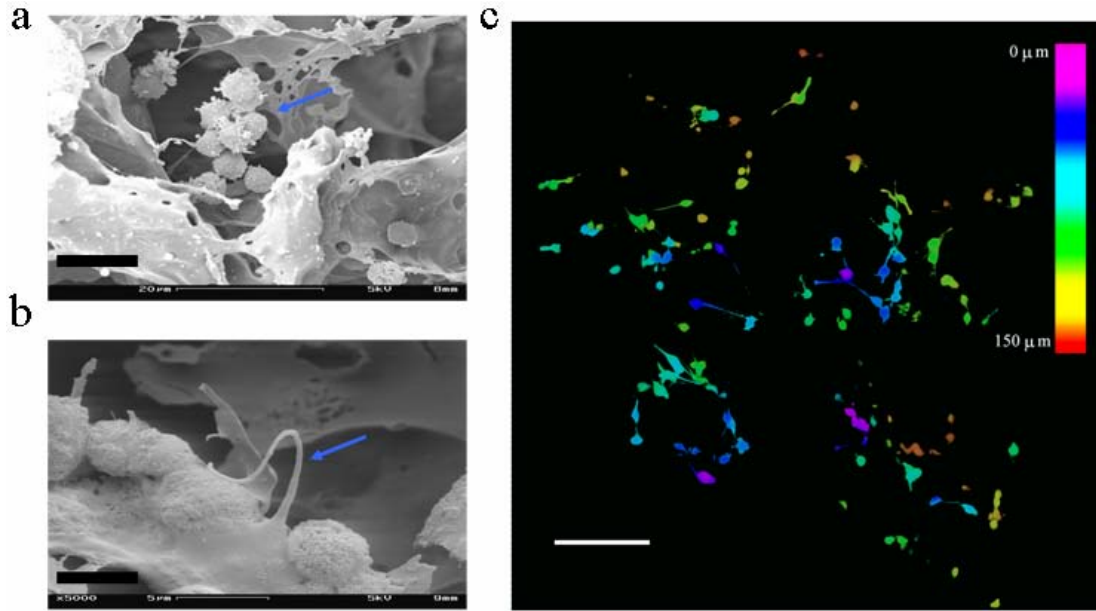
Figure 4.2. Polymer scaffolds seeded with SCG cells. (a) SEM image of a SCG cell cluster (indicated by arrow) inside a pore on day 2 after plating. (d): SEM image showing a neurite (indicated by arrow) from one cell to another on day 7 after plating (c): Confocal depth projection micrograph of a 20:1 polymer scaffold with 60-100 µm pores, seeded with SCG cells. Picture was taken after 7 days in culture. Color corresponds to the depth from the polymer surface, with pink being closest to the surface and red being at 150 µm from the surface. Bars represent 10 µm in (a), 5 µm in (b), and 100 µm in (c).
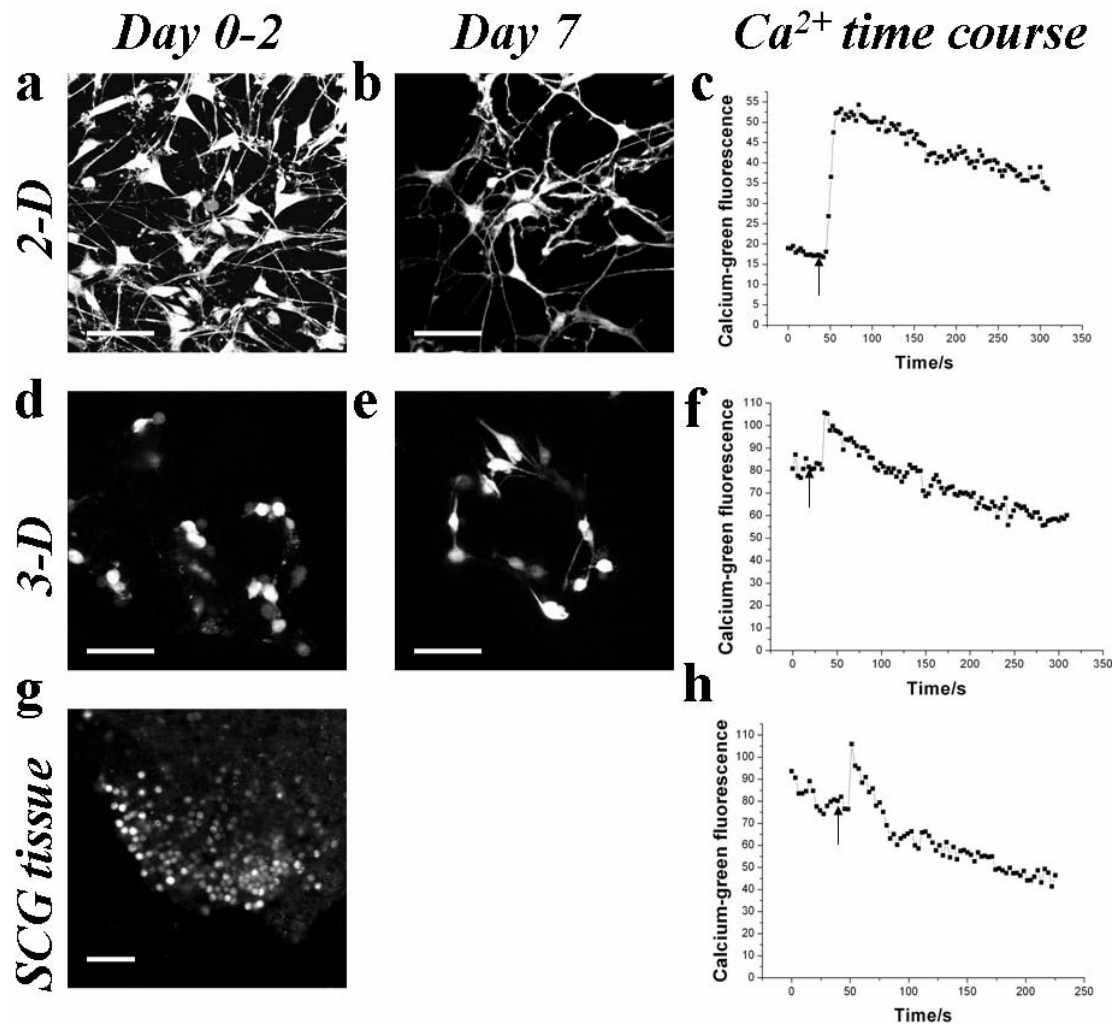
Figure 4.3. Cell morphology and high K$^+$ depolarization induced intracellular calcium changes. SCG cells were stained with a live cell indicator, 5μM Calcein AM, for 30min and captured by laser scanning confocal microscopy. (a) and (b) are confocal images of cells on 2-D substrates on day 2 and day 7 after plating, respectively. (d) and (e) are volume rendered confocal depth projection images of cells on 3-D scaffolds on day 2 and day 7 after plating respectively. (g) is a volume rendered confocal image of the cells in a intact SCG tissue. Bars represent 50μm in all these 5 images. (c) and (f) show the typical calcium time course in response to high K$^+$ (50mM) depolarization on 2-D substrates and 3-D scaffolds respectively for day 2 cultures. (h) shows

calcium time course from a typical responsive cell in an intact SCG tissue after dissection.

Arrows show the times points when high K$^+$ buffer was added.
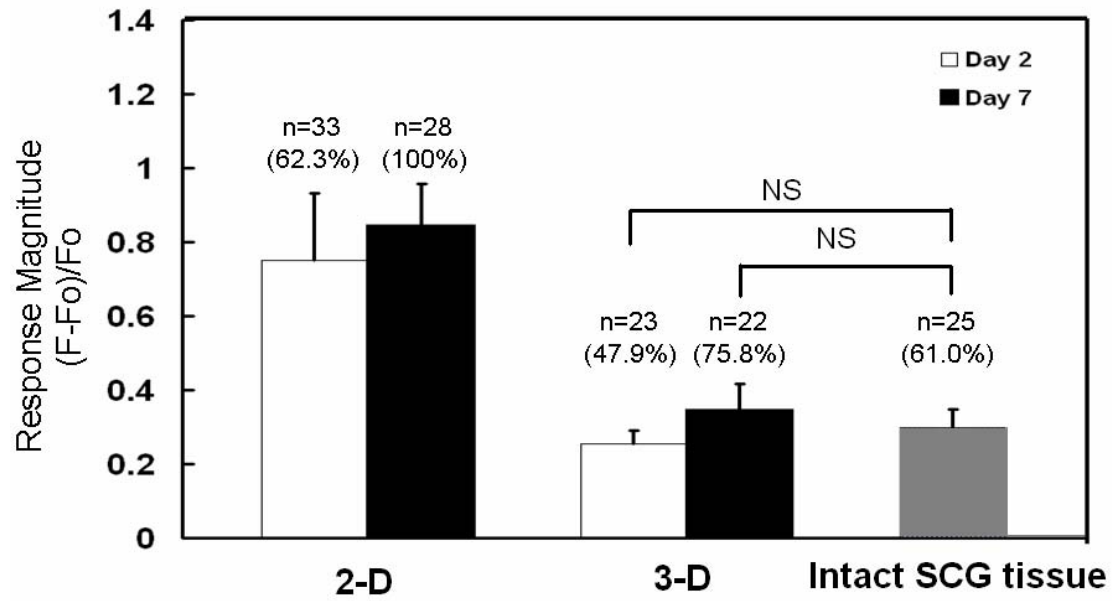
Figure 4.4. Cellular VGCC functionality. "NS" indicates that the means of the two samples compared are not significantly different with a level of $p>0.8$. "n" is the number of responsive cells. The percentage of responsive cells from the total cell pool is indicated in parenthesis. Error bars are the 95% confidence intervals.

Table 4.1. Cell morphology on 2-D substrates and 3-D scaffolds.

* value was significantly different from that on the previous measuring date ($p<0.05$)

Value was significantly different from that for 2-D substrates ($p<0.05$)

2-D substrates			
Neurite density	Neurite length	Soma section area	Soma section roundness
Day 2	121/50=2.4	38.9±17.7µm (n=121)	149.8 ± 59.3µm^2 (n=50)	0.51± 0.11(n=50)
Day 7	88/11=8.0	3.6 ± 36.1µm (n=88)*	34.5 ±72.1µm^2 (n=11)	0.54 ± 0.11(n=11)

3-D scaffolds			
Neurite density	Neurite length	Soma section area	Soma section roundness
Day 2	11/16=0.7	10.9± 3.2µm (n=11) [#]	90.0± 22.3µm^2(n=16) [#]	0.81± 0.05(n=16) [#]
Day 7	60/14=4.3	25.2± 13.8µm (n=60)*[#]	144.5± 56.9µm^2(n=14)*	0.64± 0.15(n=14)*[#]

CHAPTER 5

A NANO-FIBROUS AND MICRO-POROUS COMBINATION POLYMER SCAFFOLD

FOR THREE DIMENSIONAL CELL CULTURE*

5.1 Abstract

Polymer scaffolds play an important role in three dimensional (3-D) cell culture as well as

tissue engineering. To best mimic the architecture of the natural extracellular matrix (ECM), a

nano-fibrous/micro-porous combination (NFMP) scaffold was fabricated by phase separation

and particulate leaching techniques. The resulting scaffold possesses architectural features at two

levels, including the micro-scale pores (60-300 microns) and nano-scale fibers (around 500 nm).

Our results indicated that the NFMP scaffold inherited the advantages of micro and nano

scaffolds and was indeed superior to both of them. The nano-fibers of NFMP scaffolds were able

to promote neural differentiation of neural stem cells and induced a "3-D matrix adhesion" in

human fibroblast cells. The micro-pores of NFMP scaffolds were able to create more surface

area for cell growth. To the best of our knowledge, this is the first study to systematically

---

compare micro, nano and micro/nano combination scaffolds, and demonstrates the advantages of the micro/nano combination for tissue engineering 3-D cell culture applications.

5.2 Introduction

Cells *in vivo* are embedded in three dimensional (3-D) microenvironments. However, almost all studies in cell biology are conducted on 2-D substrates, such as Petri dishes, multi-well plates and glass slides. The architecture of the *in vivo* microenvironment is 3-D, where cells are surrounded by other cells as well as the extracellular matrix (ECM). Conventional 2-D cell cultures are unlike *in vivo* systems where cellular communication, transport of oxygen and nutrients, removal of wastes and metabolism take place in a 3-D microenvironment. Attempts have been made to culture cells in 3-D by using porous or fibrous scaffolds made from synthetic polymers and their copolymers [1]. Typically, polymer scaffolds are fabricated using particulate leaching [2], textile technologies [3], or 3-D printing [4]. In a previous study, we demonstrated that human neural stem cells cultured on a micro-porous scaffold exhibited more in-vivo-like behaviors than 2-D cultured cells, in terms of morphology, proliferation, cell-matrix adhesion, calcium channel functionality and gene expressions [5]. However, for a true 3-D environment, a scaffold surface's fibers and pores must be substantially smaller than the dimension of cells [6]. While the 3-D scaffolds we used have a porous structure

with diameters of approximately 50 μm, the natural ECM protein sizes range from 50 to 500 nm, which is much smaller than the pores in a conventional tissue engineering scaffold.

The scaffolding foundations of an engineered tissue should possess similar dimensions as the natural ECM [7]. Cells *in vivo* live in a microenvironment consistent with both nano- and micro-scale structures. On a nano-scale, it has been suggested that the nano-fibrous architecture and its high surface area could improve cell adhesion, migration, proliferation, differentiation and other cellular activities [8, 9]. On a micro-scale, it has been suggested that pore topography, size, and interconnectivity are important for cell seeding, mass transport, and 3-D tissue formation [10, 11].

Various studies have attempted to create nano and micro combination scaffolds and to study the cell-matrix interactions in these scaffolds. Zhang and Ma et al. [12-14] reported a 3-D micro-porous architecture built in the nano-fibrous matrices, fabricated by a technique combining phase-separation and particulate leaching. Pham et al. [15] reported a multilayer of nano/microfiber scaffold by using a multiple layers of electrospun poly-caprolactone (PCL) on top of micro-scale scaffolds. Lee et al. [16] introduced another approach combining electrospinning with particulate leaching methods to create a scaffold with both nano- and micro-scale structures. Correa-Duarte et al. [17] demonstrated a unique method to produce wells consisting of aligned carbon nanotubes, with micro-scale pore sizes ranging from 5 to 60 μm [17]. In most of these studies, extensive scaffold morphology and mechanical properties have been characterized. However, the benefits of nano and micro combination scaffolds have not yet been systematically investigated from a cellular phenotypic view point.

In this study, we combined phase separation and particulate leaching techniques to create a nano-fibrous poly(l-lactic acid) (PLLA) scaffolds that also consisted of interconnected micro-scale pores, hereafter referred as nano-fibrous /micro-porous combination (NFMP) scaffold. The NFMP scaffold provides a 3-D space, high porosity with interconnected pores, and nano-fibrous surfaces as the pore walls. To be able to demonstrate the benefits of NFMP scaffolds, we also fabricated PLLA nano-fibrous scaffolds and micro-porous scaffolds, hereafter referred to as Nano and Micro scaffolds, respectively, as controls. After extensive physical characterization, human neural stem and human foreskin fibroblast cells were seeded onto these scaffolds. Various parameters such as cell number, morphology, differentiation, cell-matrix adhesion were compared among these three groups. Our results show that the NFMP scaffold is more advantageous than the other two scaffolds, with respect to maximal cell intrusion, neural differentiation, and "3-D matrix adhesion". The NFMP scaffold offers a better solution for tissue engineering as well as 3-D cell culture research.

5.3 Methods and materials

5.3.1 Scaffold fabrication

Fig. 1 shows the fabrication process of NFMP scaffolds. A protocol similar to one described by Zhang and Ma [12] was followed [12]. PLLA with an inherent viscosity of 0.8-1.6 dl/g was purchased from Sigma-Aldrich (St. Louis, MO). Solutions of PLLA in tetrahydrofuran (THF)

(Fisher Scientific, Waltham, MA) were prepared by dissolving an appropriate amount of PLLA

in the solvent for 1-2 hours at 60℃ or until a homogeneous solution was obtained. Salt (sodium

chloride) particles of the desired size were added into the solutions and mixed thoroughly by

stirring. We used two different salt size groups: 60-100 μm and 100-300 μm for neural stem cell

and fibroblast cell culture, respectively. Through trial and error, these pore sizes were found to be

ideal for human NS and fibroblast cells, which are approximately 10 µm and 30 µm in diameters,

respectively. Smaller pores prevented cell intrusion, while larger pores made cell-matrix

interaction identical to 2-D conditions. Similar observations have been reported by others [18].

After the salt particulates were evenly dispersed, the whole mixture was cast into a glass Petri

dish for phase separation at -80 ℃ overnight. The Petri dish containing the phase-separated

gel/salt composite was immersed into 4 ℃ d.i. water for solvent substitution and particulate

leaching. Water was changed three times a day for 2 days. During this process, THF was

substituted by water and the salt particulates were leached away by the water, leaving a porous

structure. Scaffolds were carefully removed from the Petri dish, air-dried and kept at room

temperature until needed.

5.3.2 Scaffold characterization

The porosities of the polymer scaffolds were measured by a modified liquid displacement

method [19]. In our study, ethanol was used as the displacement liquid. Porosity was determined

for the scaffolds in Petri dishes. The scaffolds were carefully removed from the dishes with an

ultra-sharp blade and then submerged in ethanol. Scaffold mechanical strength was evaluated by determining the capacity to absorb fluid-mechanical energy without damage [20]. A syringe pumps (Orion, Boston, MA), connected to a standard 200 μl pipette tip, was used. De-ionized water was perpendicularly pumped onto the surface of polymer scaffolds for 5 s through the tip. The flow rate inducing scaffold rupture was recorded. The force, F, experienced by the scaffolds was calculated as follows:

$$F = \rho \cdot A \cdot v^2$$

Where ρ is the density of the de-ionized water, A the area of the opening of the pipette tip and v is the fluid flow rate just before impact, which depends on the rate of the syringe piston movement and the diameter of the nozzle tip.

5.3.3 Scanning electron microscopy (SEM)

Cells on scaffolds were fixed with 2% glutaraldehyde in 0.1 M sodium cacodylate buffer (pH 7.2) for 1 h and then rinsed in cacodylate buffer three times (15 min each). This was followed by post-fixing with 1% OsO4 in 0.1 M sodium cacodylate buffer for 1 h and rinsing in cacodylate buffer three times (5 min each). The samples were dehydrated in 35%, 50%, 70%, 80%, 95% and 100% ethanol successively for 10 min each and dried in a SAMDRI-780A critical point drier (Tousimis Research Corporation, MD). Scaffolds were sputter-coated with gold for 60 s to achieve a thickness of about 15.3 nm. SEM images were captured with a LEO 982 scanning electron microscope (LEO Electronenmikroskopie GmbH Korporation, Germany) or an

Inspect^{TM} F scanning electron microscopy (FEI Company, Hillsboro, OR, USA). A similar

protocol was followed for scaffold samples without cells, with the exception that the preparation

started with sputter coating.

5.3.4 NS cell culture

Before all cell seeding, the air-dried scaffolds were pre-wetted and sterilized in 70% ethanol

overnight. A human neural stem (NS) cell line, ENStem-A^{TM} (Millipore, Billerica, MA), was

maintained in neural basal media (Invitrogen, Carlsbad, CA), supplemented with

penicillin/streptomycin, L-glutamine, recombinant human leukemia inhibitory factor (hLIF),

basic fibroblast growth factor (bFGF) and B-27 (a serum-free supplement). The composition of

differentiation media was similar to the subculture media described above but without bFGF.

The NS cells were incubated at 37 °C in a 5% CO_2 humidified atmosphere. To achieve better cell

attachment, the scaffolds were coated with poly-ornithine (Sigma-Aldrich; MW 30,000-70,000

Da) and laminin (Sigma-Aldrich; from Engelbreth-Holm-Swarm murine sarcoma basement

membrane). NS cells were seeded at a uniform density of 50,000 cells/cm^2.

5.3.5 Fibroblast cell culture

Human foreskin fibroblast cells were purchased from ATCC (ATCC#: SCRC-1041). Prior

to cell seeding, the scaffold samples were coated with 0.2% Gelatin (Sigma G1393, 2% solution

from Bovine Skin, diluted with sterile H_2O prior to use) for 1 hour at room temperature. After that, the samples were air-dried for 15-20 min before cell plating. Cells were maintained in DMEM (4.5 g/l glucose, 1.5g/l sodium bicarbonate) with the presence of 15% Fetal Bovine Serum (ATCC#: 30-2020) at 5% CO2 and 37°C. All cell types were grown on either glass flat surfaces or polymer scaffolds. Medium changes were performed every other day. Cells were seeded at a uniform density of 4,000 cells/cm^2.

5.3.6 MTT assay

NS cell population was estimated by determining the amount of viable cells in a sample with measurement of cell mitochondrial dehydrogenase activity. A MTT assay kit (Sigma, St. Louis, MO) was applied and the manufacturer's instructions were followed. All the cell-scaffold construct samples were cut to fit the bottom of 24 well plates. 100 µl of MTT solution (5 mg/ml reconstituted in NS cell culture media) was added to each well. After three hours of incubation at 37ºC, MTT solution was aspirated off and MTT solubalizing solution was added to each well. The plate was shaken at 115 rpm at 25ºC for 30 minutes. Contents of each well were placed in 15 ml conical tubes and spun at 270 x g for 10 minutes at 4ºC. 250 µl of the supernatant was transferred to a 96 well plate and read at 590 nm.

5.3.7 Immuno-fluorescence staining for neural differentiation markers

A standard immuno-fluorescence staining protocol for differentiation markers was followed [21]. For differentiation maker staining, NS cells were washed with PBS (with calcium and magnesium) twice before fixing with 2% paraformaldehyde in PBS for 15 minutes. After that, samples were washed with PBS twice and washing buffer four times for 5 minutes each. The washing buffer was prepared by adding 25 µL Tween 20 (EMD Chemical, Gibbstown, NJ) into 50 mL high salt buffer, which was comprised of 250 mM sodium chloride and 50 mM Tris (Sigma, St. Louis, MO), pH 7.4. Samples were blocked for 45 minutes in blocking buffer, which was comprised of 6% donkey serum (Cat No. 017-000-121, Jackson ImmunoResearch, West Grove, PA) in high salt buffer. Cells were then incubated with mouse anti-human nestin IgG1 (Cat No. MO15012, Neuromics, Northfield, MN) and chicken anti-Tuj IgY (Cat No. AB9354, Chemicon, Temecula, CA) in blocking buffer at dilutions of 1:200, and 1:1000, respectively, for 45 minutes for double staining (nestin + Tuj). Samples were washed with high salt buffer four times for 5 minutes each. Cells were then incubated for 1 hour with blocking buffer containing Alexa Fluor® 488 donkey anti-mouse IgG (H+L) conjugate (Cat No. A21202, Molecular Probes, Eugene, OR) at a dilution of 1:1000 and Texas Red® dye-conjugated AffiniPure Donkey anti-chicken IgY (Cat No. 703-075-155, Jackson ImmunoResearch, West Grove, PA) at a dilution of 1:250. Samples were then washed with PBS four times for 5 minutes each. Cells were contrast stained with 4',6-diamidino-2-phenylindole (DAPI, Cat No. 80051-386, VWR, West Chester, PA) at a 1:10,000 dilution in distilled water for 5 minutes. After three washes with PBS,

the samples were mounted on a coverslip. Fluorescent images were viewed with a Nikon

ECLIPSE TE2000-S inverted microscope with a fluorescent attachment using a $40 \times$ objective.

5.3.8 Immuno-fluorescence staining for FAK PY^{397}

Rabbit (polyclonal) anti-FAK PY^{397} antibody was purchased from Biosource International,

CA, USA. Secondary antibody Alexa Fluor® 488 chicken anti-rabbit (H+L) were purchased

from Molecular Probes, OR, USA. Normal chicken serum was purchased from Zymed

Laboratories, CA. Cells were rinsed once with PBS, fixed with 4% paraformaldehye in PBS

(15 min), washed with PBS, treated with 0.5% Triton X-100 (5 min). After that, cells were

washed with PBS, blocked with normal chicken serum (2% diluted with PBS/0.3% Tween-20)

for 30 min at room temperature, washed with PBS (3 ×, 5 min per wash), incubated overnight

with primary antibody (1:100), washed with PBS (3 ×, 5 min per wash) followed by incubation

for 1 h with the secondary antibody (1:500), washed with PBS (3×, 5 min per wash), and then

loaded with Dapi (1:5000) for 5 min at room temperature. After PBS wash, cells were ready for

microscopy observation. Epi-fluorescence images were taken with a Nikon ECLIPSE TE3000

inverted microscope with a fluorescent attachment using a $60 \times$ objective. Negative controls for

staining were routinely performed.

5.4 Results and discussion

5.4.1 Scaffold characterization

Porous morphologies of the scaffolds were examined with scanning electron microscopy (SEM). SEM micrographs clearly show that the NFMP scaffold has two levels of structures: a nano-fibrous scaffold body and an interconnected micro-porous structure inside the scaffold body (Fig. 2a). A snapshot of a single pore (Fig. 2b) shows that the pore size is around 80 μm, which is precisely controlled by the salt particulate size we used (60-100 μm). The pore walls have a well-defined nano-fibrous morphology which is desirable for cell adhesion inside the pores. The whole body of the scaffold is composed of nano-fibrous structures (Fig. 2c) which emulate the morphology of natural ECM. Average fiber size is around 500 nm (insert of Fig. 2c). A cross-section view of the scaffold indicates that the micro-pores are interconnected with each other and the two levels of structures are uniformly distributed from the surface to deep inside the scaffolds (Fig. 2d). For a comparative study, we also fabricate micro-porous scaffolds (Fig. 2e) and nano-fibrous scaffolds (Fig. 2f) by using salt particulate leaching and phase separation methods.

A series of NFMP scaffolds were fabricated with PLLA dissolved in THF solution. The matrices were fabricated with varying polymer concentrations and pore sizes, and mechanical strength (rupture force) and porosity were measured and the results are summarized in Table 1. Similar to results reported by other groups [13, 14], these scaffolds had very high porosities, and exhibited increased mechanical strength and decreased porosity with increasing polymer

concentration. Using different particle sizes, one can readily control the pore sizes. A particular pore size is chosen according to the size of the cells in use. We observed that at the same polymer concentration, the mechanical strength increased and the porosity decreased with increased pore size from 60-100 μm to 100-300 μm.

We also compared the porosities and mechanical strengths of Micro, Nano and NFMP scaffolds fabricated with the same polymer concentration (4%) and pore size (60-100μm). The results summarized in Fig. 3 show that the Nano scaffolds' porosity (95.4%±0.35) was lower than that of Micro and NFMP scaffolds, which were 97.0%±0.49 and 97.4%±0.36 ($p < 0.05$), respectively. On the contrary, the rupture force of Nano scaffolds (0.331±0.039 N) was significantly higher than that of Micro and NFMP scaffolds, which were 0.068±0.012 N and 0.061±0.003 N, respectively ($p < 0.001$). It is worth noting that at the same polymer concentration and pore size, the NFMP scaffolds exhibited the highest porosity and lowest mechanical strength among the three preparations. A high porosity is good for cell migration as well as for nutrients/wastes transportation in the media. Although the mechanical strength of NFMP scaffolds was much lower than that of Nano scaffolds, it was comparable to the Micro scaffolds, which are the standard tissue engineering scaffolds in use today. As for 3D cell culture and cell-based assay applications, the NFMP scaffold's mechanical strength is still much higher than the maximum possible force a typical fluid transfer workstation (e.g. Flexstation®, Molecular Devices, Sunnyvale, CA) could generate (0.11 mN).

5.4.2 Neural stem cell growth and morphology

As the NS cells play a unique and important role in nerve repair, their growth, and morphology on the PLLA scaffolds are critical to tissue engineering as well as 3D cell-based assay applications. Particularly, a large population of cells is favorable for both cell-based assay or tissue regeneration applications. The NS cell population after 7 days' culture in growth media was assessed by a standard MTT assay and the results are presented in Fig 4. With the same initial seeding density and culture period, the Micro scaffold and the NFMP scaffold exhibited a significantly larger cell population than the Nano scaffold. This is reasonable since Micro and NFMP scaffolds have more spatial volume for cell to spread. On Nano scaffolds, the pores were too small for cells to migrate into the body thus the cells could only grow on the top surface of the scaffold. In other words, cells cultured on nano-scale structures are not "real" 3D cell cultures. It is also worth noting that the micro scaffold had more cells than the NFMP scaffold. This may due to the possibility that nano-structure induced partial neural differentiation which suppressed NS cell proliferation. Evidence in support of partial differentiation is provided in Section 3.3.

Neural stem cell morphology and the outgrowth of neurites usually are indicators of neural differentiation. Successful nerve regeneration relies on the extensive growth of axonal processes. For this reason, the present study also focused on the effect of nanotexture on neurite length. The NS cells were cultured in growth media for 3 days and then changed into differentiation media. After one week into differentiation, SEM images showed that the NS cells on Nano (Fig. 5a) and NFMP scaffolds (Fig. 5b) developed long and well-defined neurites (red arrows), whilst the cells

on Micro scaffolds did not show very long neurites (Fig. 5c). This suggested that the cells on Micro scaffolds were probably still in a proliferative rather than differentiation stage. These findings suggest that the nanofibers help to improve the neurite outgrowth and might promote neural differentiation compared to flat pore walls in Micro scaffolds. It has been suggested that nanotexture can promote both *in vivo* and *in vitro* neurite outgrowth. Ellis-Behnke et al. [22] reported that a designed self-assembling peptide nanofiber scaffold creates a permissive environment for axons to regenerate through the site of an acute injury and to knit the brain tissue together in vivo. Yang et al. [23, 24] reported that aligned nanofibers highly supported the mouse NS cell culture and improved the neurite outgrowth compared to the microfibers. Similar findings reported by Moxon et al. [25] showed increased extension of neurites from pheochromocytoma cells on nano-porous silicon surfaces compared to smooth silicon surfaces [25]. Although the mechanism involved in how nanotexture influences cell morphology and functionality is still unclear, it is reasonable to suggest that nanofiberous structure is favorable for neurite outgrowth in the following ways: first, the nanotexture increases the surface roughness which is favorable for cell attachment and migration; second, the nanofibers can serve as the conduits to guide the neurite outgrowth from the cell body; third, the nano-porous structure might create a diffusion gradient which is favorable for NS cell differentiation and neurite outgrowth.

5.4.3 NS cell differentiation

To further investigate and quantify the differentiation of NS cells in different scaffolds, cells were stained with two well-known markers, beta-tubulin III (Tuj) for neurons (red) and nestin for neural progenitors (green). Fig. 6 shows the immunofluorescent micrographs of the NS cells on Nano (a), NFMP (b) and Micro scaffolds (c). It was found that a large number of cells on all the three scaffolds were stained positive for both Tuj and nestin after 14 days into differentiation. Quantitative differentiation results are expressed as the percentage of Tuj positive cells out of the total cell population (Dapi cell nuclei staining). A summary of the percent of Tuj positive cells on different types of scaffolds is shown in Fig. 6d. Compared to Nano and NFMP scaffolds, the Micro scaffolds exhibited significantly lower percentage for the neural marker Tuj (50.6% ± 2.9 for Micro scaffold, 82.5% ±1.9 for Nano scaffold, and 80.5% ± 2.6 for NFMP scaffold). Also, the same morphological differences found in SEM images were further confirmed in the immuno-fluorescence micrographs. Long Tuj positive neurites were found on Nano and in NFMP scaffolds while shorter neurites were observed in Micro scaffolds. These results showed that the nanofibers in NFMP scaffolds play an important role in promoting neural differentiation as more mature neurons were observed. It is worthy noting that the differentiation of NS cells was controlled and indeed suppressed by a honeycomb micro-structure [26]. The suppression of neural differentiation is not ideal for nerve tissue regeneration purposes, since a successful scaffold should facilitate the differentiation of neural stem cell to into mature neurons for nerve repair purposes. Our results indicated that nano-modification in a traditional micro-porous tissue

engineering scaffolds could promote the differentiation of NS cells into mature neurons. Similar findings on the effect of nanotexture were reported by other groups. Gelain et al. [6] reported that in a designer peptide nano-fiberous scaffold, the NS cell populations with Tug markers are similar to those found in cell populations cultured on Matrigel which is a natural ECM component. In addition, gene expression profiling array experiments showed selective gene expression involved in neural stem cell adhesion and differentiation. Jen and Kotov [27] reported that mouse embryonic NS cells from the cortex can be successfully differentiated to neurons, astrocytes, and oligodendrocytes with clear formation of neurites on layer-by-layer assembled single-walled carbon nanotube-polyelectrolyte multilayer thin films, which is another form of nano-scale pores and fibers [27]. Additionally, up-regulation of neuronal marker expressions was found from nanopatterned human mesenchymal stem cells compared to smooth surfaces. Most recently, Silva et al. [28] reported that an artificial nanofiber scaffold induced very rapid differentiation of NS cells into neurons, while discouraging the development of astrocytes.

The mechanisms of how nano-topographical surfaces affect stem cell differentiation were yet fully understood. However, what is clear is that nano-topography control cell morphology and consequently morphology changes regulate cellular functions such as proliferation and differentiation. It is well known that cell adhesion to the ECM is initiated by clustering of integrins, which leads to the subsequent formation of focal adhesions [29]. By altering the cytoskeleton arrangement, nano-topography induces cell morphology changes. Recently, scientists began to understand how cells translate changes in cell morphology into molecular signals that regulate cell functions. A class of molecules known as the Rho family of GTPases is

thought to play a significant role in relaying structure- and adhesion-mediated signals. It is already know that Rho GTPases have numerous effects on cellular functions including proliferation, migration, and polarity [30]. It appears that cellular organization feeds back to regulate RhoA signaling and this is a key mechanism by which cell shape can regulate function. As an example, in studies of mesenchymal stem cell differentiation, it was found that Rho-mediated contractility is required for differentiation of spread cells into bone [31]. It has been shown that RhoA-generated contractility is required for the high traction forces observed in well spread cells using a micro-fabricated force sensor array [32], and that differentiation into bone required the support of high tensional environments associated with stiff matrices [33]. RhoA signaling appears to be important not only for sensing cell shape, but also for transducing nanotopography of a surface [34] and mechanical stiffness [33]. Thus, it now appears that a feedback system between cellular and ECM structure, RhoA signaling, and adhesion signaling play an important role in nano-topography mediated cellular outcomes..

5.4.4 Fibroblast cell morphology

Fibroblast cell morphology in NFMP, Nano and Micro scaffolds were examined with SEM images. SEM micrographs showed that cells cultured on the Nano (Fig. 7c) and in NFMP (Fig. 7b) scaffolds had significantly smaller areas and perimeters than cells cultured in Micro scaffold and on flat controls (Fig. 7a and d). The results also showed that the cells had a more rounded cell body on nanofiber structures. Similar morphorlogical changes have been reported by others.

Dalby et al. [35] reported that the fibroblast cell perimeter on nano-columns produced by colloidal lithography was reduced compared to fibroblasts grown on flat surfaces control. Berry et al. [36] reported that fibroblasts exhibited much smaller spread area and more circular body in an internal nanotopography than the traditional 3D microtube structure controls. The cells on nanotopography revealed a smaller cell area and were more rounded/circular with stellate cell morphology.

Fibroblasts are anchorage dependent cells and therefore need to spread in order to enter G1 and G2 of the cell cycle [37]. Changes in cell shape, anchorage and motility are all associated with the dynamic reorganization of the filament arrays that make up the cytoskeleton. Cells use contractile actin stress fibers to spread onto material surfaces, and it has been shown in this study that while cells on the planar controls have many stress fibers, and hence are flat, cells on the nano-columns have fewer stress fibers, and are thus less spread and more rounded [35]. It appears that rather than adhering and spreading (as is apparent in cells on the planar controls), fibroblasts on a nanotextured structures were rather more polarized with rounded cell bodies. It was also observed that cells in micro-structures had clearly defined actin fibers, with prominent stress fibers, and tubulin fibers radiating out for the centre of the cell, as opposed to the cells on nano-structures which exhibited poor actin organization. Our results in the following section further confirmed that the differences in focal adhesion contacts between fibroblast cell on Nano and in Micro structures.

5.4.5 Fibroblast cell-matrix adhesion

Cellular development, organization and functionality *in vivo* are regulated by interactions with a diverse group of macromolecules that comprise the ECM. Focal adhesion kinase (FAK) has been proposed to function as a central mechano-sensing transducer in cells [38]. Particularly, phosphorylation of FAK at tyrosine 397 (FAK PY397) in fibroblasts and breast epithelial cells has been demonstrated to be a key signaling event [39, 40]. In a previous work [5], we utilized an antibody specific for FAK PY397 to examine its patterns in human NS cells cultured on micro-porous scaffolds and flat controls. In this work, we performed the same immnuno-staining of FAK PY397 in human fibroblasts, which are a widely-used model for focal adhesion studies [39, 41]. The staining was performed at Day 2 in culture after seeding fibroblast cells on the Nano and in the Micro and NFMP scaffolds as well as on flat controls. As shown in Fig. 8d, cells cultured on glass demonstrated a streaky pattern of labeling. The localization of FAK PY397 for cells on Nano (Fig. 8b) and in NFMP scaffolds (Fig. 8a) was more punctate and less well defined. The observations made from Micro scaffolds (Fig. 8c) revealed that the labeling of FAK PY397 was streaky-like at the peripheral of the cell. However, these streaky patterns were not as well-defined as those from cells on flat-surface controls. Similar findings were made by Schindler et al. [41] who found the fibroblasts on a synthetic nano-fiber scaffold (UltraWeb[TM]) exhibited similar punctate patterns compared to a well-defined streaky pattern on the flat controls. Additionally, Berry et al. [36] reported that fibroblasts cultured in the nano-tubes exhibit punctate actin throughout the cell body, while cells in the micro-tube controls exhibit

dash-shaped adhesions throughout the cell, reflecting their well spread morphology compared to the small adhesions and smaller sized morphology on nano-tubes.

The FAK PY397 labeling patterns observed on flat controls is characteristic of localization at focal adhesion sites [39, 42]. Loss of FAK PY397 localizations at focal adhesions has been correlated with morphogenesis and differentiation in breast epithelial cells cultured in a 3-D microenvironment [40]. It is worth noting that Cukierman et al. [39] reported a loss of FAK PY397 staining at adhesion sites and a decrease in the amount of phosphorylated FAK for fibroblasts cultured in 3-D matrices derived either from detergent-extracted mouse embryo sections or from naturally deposited three-dimensional ECMs of fibroblasts. They named such sites, more characteristic for cells *in vivo*, ''3D-matrix adhesions''.

Our results suggest "3D-matrix adhesions" in NFMP and on Nano scaffolds but not on flat controls. The observations from Micro scaffolds are between flat controls and the two nano-textured scaffolds. As shown in Fig. 8c, the FAK PY397 staining in Micro scaffolds also showed some streaky pattern but much less than what was found on flat controls (Fig. 8d). This might indicate that the topography of a micro scaffold, particularly its pore curvature, might also influence the cell-matrix adhesions and indeed create some "3D adhesions" effect on the cells. The strongest "3D-matrix adhesions" effect observed with NFMP and Nano scaffolds suggests that nano-fibers affect cell-matrix adhesion more than the micro-pores do.

5.5 Conclusion

In this work, two standard fabrication techniques were combined to yield scaffolds with two levels of structures: highly interconnected micro-porous structures and nano-fibrous architecture. The micro-porous architectural design enables cell seeding and distribution in the 3-D nano-fibrous matrices for 3-D cell culture and tissue engineering applications. As discussed in the previous sections, both nano and micro structures have their unique merits in creating a 3-D microenvironment for cells. These advantages are summarized in Table 2. As shown, the micro structures can induce 3-D tissue formation and 3-D cell-cell contact interactions; the nano structures can induce 3-D cell migration, 3-D cell-matrix adhesion and create a 3-D gradient diffusion. As a combination of nano-fibers and micro-pores, the NFMP scaffold exhibits all these merits. The cells in the NFMP scaffolds, in contrast to traditional micro-structure tissue engineering scaffold, will attach on and interact with a nano-fibrous network instead of "solid walls" during the *in vivo* and *in vitro* growth. These new synthetic ECM structures may provide better environments for cell distribution, adhesion, growth, and differentiated function, emulating the *in vivo* conditions better. The architectural design at several size scales gives these novel scaffolds the potential to be tailored for a variety of 3-D cell culture and tissue regeneration applications. To the best of our knowledge, this is the first study to systematically compare micro, nano and micro/nano combination scaffolds, and to demonstrate the advantages of the micro/nano scaffolds for tissue engineering and 3-D cell culture applications at the cellular function level.

5.6 Acknowledgements

5.7 References

1. Langer R, Vacanti JP. Tissue engineering. Science. 1993;260:920-926

2. Mikos AG, Thorsen AJ, Czerwonka LA, Bap Y, Langer R, Winslow DN, Vacanti JP. Preparation and characterization of poly (L-lactic acid) foams. Polymer. 1994;35:1068-77

3. Ma PX, Langer R. Degradation, structure and properties of fibrous nonwoven poly (glycolic acid) scaffolds for tissue engineering. Polymers in medicine and pharmacy. 1995; Pitsburgh, PA: MRS; p.99-104.

4. Giordano RA, Wu BM, Borland SW, Cima LG, Sachs EM, Cima MJ. Mechanical properties of dense poly acid structures fabricated by three-dimensional printing. Journal of Biometerials Science - Polymer Education.2001;8:63-75.

5. Cheng, K, Lai Y, Kisaalita WS. Three dimensional polymer scaffolds for high throughput cell-based assay systems. Biomaterials. 2008;29:2802-12.

6. Gelain F, Bottai D, Vescovi A, Zhang S. Designer self-assembling peptide nanofiber scaffolds for adult mouse neural stem cell 3-dimensional cultures. PLoS ONE. 2006;1(1):e119.

7. Hartgerink JD, Beniash E, and Stupp SI. Self-assembly and mineralization of

peptide-amphiphile nanofibers. Science. 2001;294:1684-8.

8. Kuntz RM, Saltzman WM. Neutrophil motility in extracellular matrix gels: mesh size and adhesion affect effect speed of migration. Biophysics Journal. 1997;72:1472-80.

9. Benya PD, Shaffer JD. Dedifferentiated chondrocytes reexpress the differentiated collagen phenotype when cultured in agarose gels. Cell. 1982;30:215-24.

10. Ma, PX, Zhang RY. Microtubular architecture of biodegradable polymer scaffolds. Journal of Biomedical Materials Research. 2001;56:469-77.

11. Hollister SJ, Maddox RD, Taboas JM. Optimal design and fabrication of scaffolds to mimic tissue properties and satisfy biological constraints. Biomaterials. 2002;23: 4095-103.

12. Zhang RY, Ma PX. Synthetic nano-fibrillar extracellular matrices with predesigned macroporous architectures. Journal of Biomedical Materials Researches 2000;52:430–8.

13. Chen VJ, Ma PX. Nano-fibrous poly(l-lactic acid) scaffolds with interconnected spherical macropores. Biomaterials. 2004;25:2065–2073.

14. Liu X, Won Y, Ma PX. Porogen-induced surface modification of nano-fibrous poly(L-lactic acid) scaffolds for tissue engineering. Biomaterials. 2006;27:3980–3987.

15. Pham QP, Sharma U, Mikos AG. Electrospun poly(-caprolactone) microfiber and multilayer nanofiber/microfiber scaffolds: characterization of scaffolds and measurement of cellular infiltration. Biomacromolecules. 2006;7(10):2796-2805.

16. Lee YH, Lee JH, An I-G, Kim C, Lee DS, Lee YK, Nam J-D. Electrospun dualporosity structure and biodegradation morphology of montmorillonite reinforced PLLA nanocomposite scaffolds. Biomaterials 2004;26(16):3165-3172.

17. Correa-Duarte MA, Wagner N, Rojas-Chapana J, Morsczeck C, Thie M, Giersig M. Fabrication and biocompatibility of carbon nanotube-based 3D networks as scaffolds for cell seeding an growth. Nanoletters. 2004;4:2233-2236.

18. Freyman TM, Yannas IV, Gibson LJ. Cellular materials as porous scaffolds for tissue engineering. Progress in Material Science. 2001;46:273-282.

19. Zhang R, Ma PX. Poly (alpha-hydroxyl acids)/hydroxyapatite porous composites for bone-tissue engineering. I. Preparation and morphology. Journal of Biomedical Materials Research. 1999;44:446-455.

20. Mao C, Kisaalita WS. Characterization of 3-D collagen gels for functional cell-based biosensing. Biosensors and Bioelectronics. 2004;19:1075-1088.

21. Dhara SK, Hasneen K, Machacek DW, Boyd NL, Rao RR, Stice SL. Human neural progenitor cells derived from embryonic stem cells in feeder-free cultures. Differentiation. 2008;76(5):454-464.

22. Ellis-Behnke RG, Liang YX, You SW, Tay DKC, Zhang S, So K, and Schneider GE. Nano neuro knitting: Peptide nanofiber scaffold for brain repair and axon regeneration with functional return of vision. PNAS. 2006;103(13):5054-5059.

23. Yang F, Murugan S, Wang S, Ramakrishna S. Electrospinning of nano/micro scale poly(L-lactic acid) aligned fibers and their potential in neural tissue engineering. Biomaterials. 2005;26:2603–2610.

24. Yang F, Murugan S, Ramakrishna S, Wang X, Ma YX, Wang X. Fabrication of nano-structured porous PLLAscaffold intended for nerve tissue engineering. Biomaterials.

2004;25:1891–1900.

25. Moxon KA, Kalkhoran NM, Markert M, Sambito MA, McKenzie JL, Webster JT. Nanostructured surface modification of ceramic-based microelectrodes to enhance biocompatibility for a direct Brain-Machine Interface. IEEE Transactions on Biomedical Engineering. 2004;51(6):881-889.

26. Tsuruma A, Tanaka M, Yamamoto S, and Shimomura M. Control of neural stem cell differentiation on honeycomb films. Colloids and Surfaces A: Physicochemical and Engineering Aspects. 2008;313-314:536-540.

27. Jan E, Kotov NA. Successful Differentiation of Mouse Neural Stem Cells on Layer-by-Layer Assembled Single-Walled Carbon Nanotube Composite. Nanoletters. 2007;7(5):1123-1128.

28. Silva GA, Czeisler C, Niece KL, Beniash E, Harrington DA, Kessler JA, Stupp SI,. Selective differentiation of neural progenitor cells by high-epitope density nanofibers. Science. 2004;303:1352-1355.

29. Schwartz MA, Ginsberg MH. Networks and crosstalk: integrin signalling spreads, Nature Cell Biology. 2002;4(4):E65-E68.

30. Etienne-Manneville S, Hall A. Rho GTPases in cell biology. Nature 2002;420(6916):629-635.

31. McBeath R, Pirone DM, Nelson CM, Bhadriraju K, Chen CS. Cell shape, cytoskeletal tension, and RhoA regulate stem cell lineage commitment. Developmental Cell. 2004;6(4):483-495.

32. Tan JL, Tien J, Pirone DM, Gray DS, Bhadriraju K, Chen CS. Cells lying on a bed of

microneedles: an approach to isolate mechanical force. PNAS.2003;100(4):1484-1489.

33. Engler AJ, Sen S, Sweeney HL, Discher DE. Matrix elasticity directs stem cell lineage specification. Cell. 2006;126(4):677-689.

34. Teixeira AI, McKie GA, Foley JD, Bertics PJ, Nealey PF, Murphy CJ. The effect of environmental factors on the response of human corneal epithelial cells to nanoscale substrate topography. Biomaterials. 2006;27(21):3945-3954.

35. Dalby M, Riehlea MO, Sutherland DS, Agheli H, Curtis ASG. Changes in fibroblast morphology in response to nano-columns produced by colloidal lithography. Biomaterials. 2004;25:5415-5422.

36. Berry CC, Dalby MJ, McCloy D, Affrossman S. The fibroblast response to tubes exhibiting internal nanotopography. Biomaterials. 2005;26:4985–4992.

37. Folkman J, Moscona A. Role of cell shape in growth control. Nature. 1978;273:345–9.

38. Wang HB, Dembo M, Hanks SK, Wang Y. Focal adhesion kinase is involved in mechanosensing during fibroblast migration. PNAS. 2001;98(20):11295-300.

39. Cukierman E, Pankov R, Stevens DR, Yamada KM. Taking cell-matrix adhesions to the third dimension. Science. 2001;294(5547):1708–12.

40. WozniakMA, Desai R, Solski PA, Der CJ, Keely PJ. ROCK-generated contractility regulates breast epithelial cell differentiation in response to the physical properties of a three-dimensional collagen matrix. Journal of Cell Biology. 2003;163(3):583-95.

41. Schindler M, Ahmed I, Kamal J, Nur-E-Kamal A, Grafe TH, Chung HY, Meiners S. A synthetic nanofibrillar matrix promotes in vivo-like organization and morphogenesis for cells

in culture Biomaterials. 2005;26:5624–5631.

42. Zamir E, Geiger B. Molecular complexity and dynamics of cell–matrix adhesions. Journal of Cell Sciences. 2001;114(Pt 20):3583–90.

Table 5.1. Characterization of NFMP scaffolds.

Polymer Concentration % (w/v)	porogen size (µm)	porosity (%) (mean±sd)	mechanical strength (mN)
2	60-100	98.5±0.40	37.9±5.2
4	60-100	97.4±0.36	60.5±3.3
7	60-100	96.7±0.20	86.1±4.0
10	60-100	96.3±0.21	108.4±4.5
4	100-300	96.5±0.26	90.9±4.1

Table 5.2. Summary of 3-D microenvironments.

	Micro	**Nano**	**Micro-Nano (NFMP)**
3-D tissue formation	√		√
3-D cell migration		√	√
3-D cell-cell contact interactions	√		√
3-D cell-matrix interaction		√	√
3-D gradient diffusion		√	√
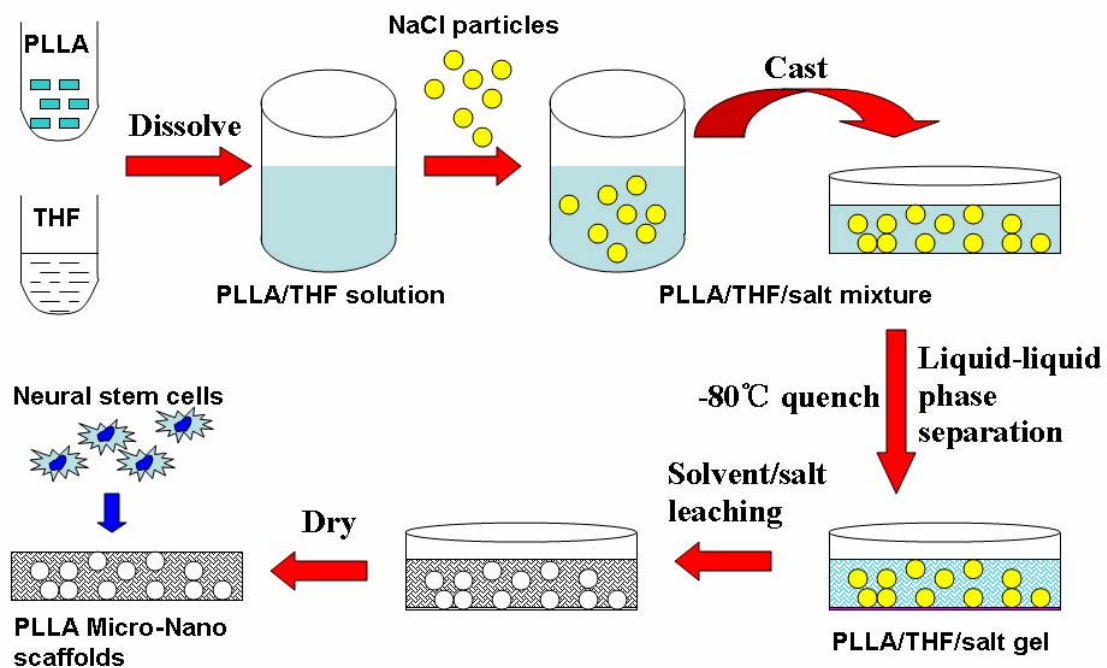
Figure 5.1. Schematic of NFMP scaffold fabrication.
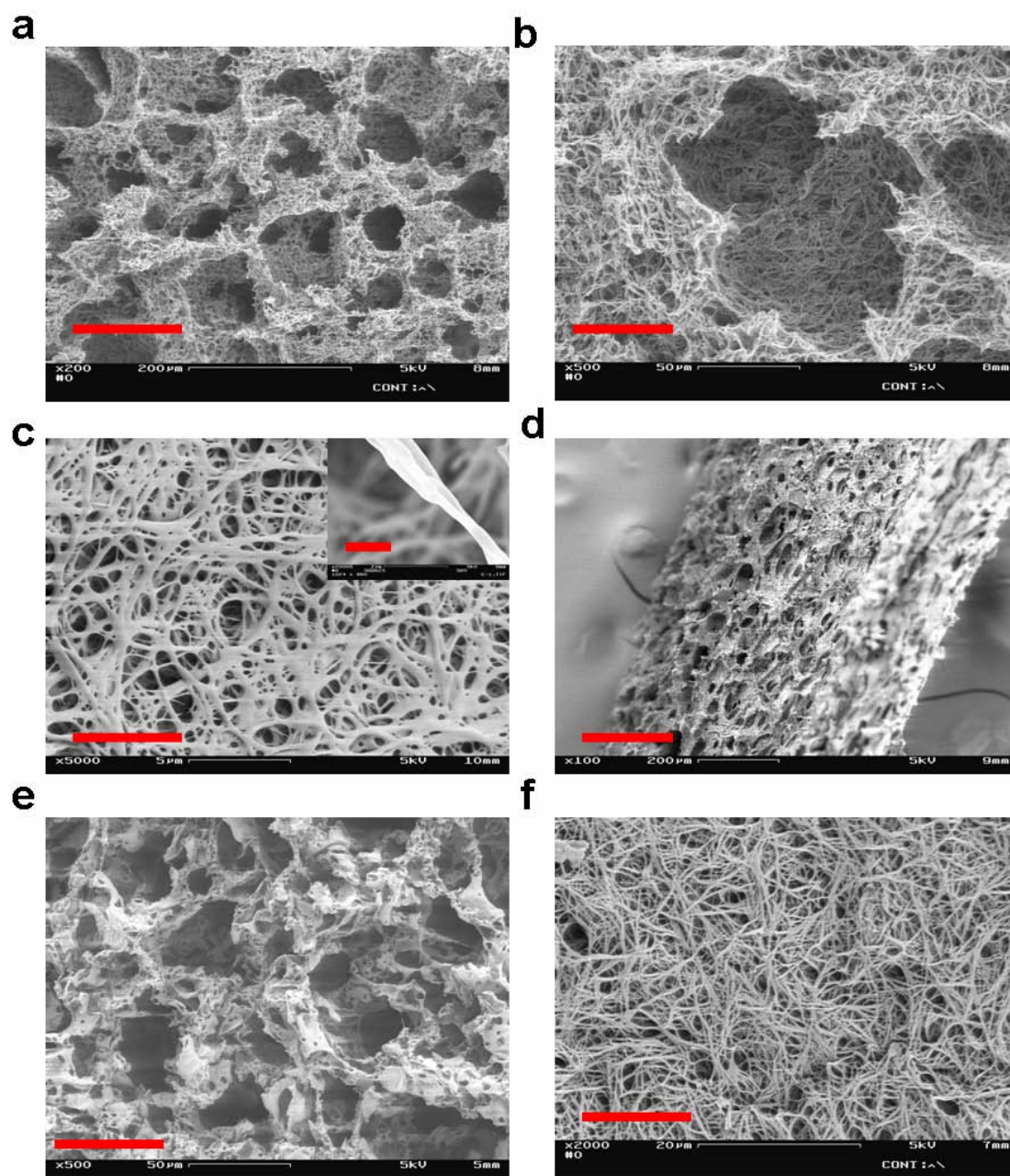
Figure 5.2. SEM micrographs of the NFMP scaffold. SEM micrographs showing the overall topography of the NFMP scaffolds (a) which combine two levels of structures: highly interconnected micro-porous structures (b) embedded in the nano-textured scaffold body (c). A snapshot of nano-fibers is shown (insert of (c)). The cross-section view (d) of the NFMP scaffold shows the two levels of structures, uniformly distributed. (e): A traditional micro-porous scaffold

fabricated by salt-leaching method. (f): A traditional nano-fibrous scaffold fabricated by phase-separation method. Bars represent 100 µm, 50 µm, 5 µm, 200 µm, 50 µm and 10 µm in (a), (b), (c), (d), (e), and (f) respectively.
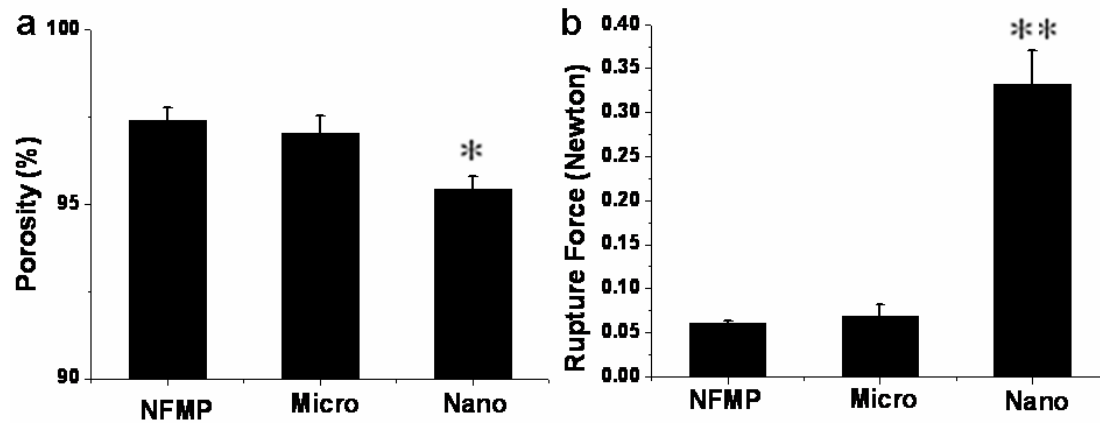
Figure 5.3. Porosity and mechanical strength (rupture force) comparison of NFMP, Micro and

Nano scaffolds. Micro, Nano and NFMP scaffolds were fabricated with the same polymer

concentration (4%) and pore size (60-100 μm). The porosities (a) and rupture forces (b) were

measured. * indicates $P < 0.05$. ** indicates $P < 0.01$. n =3 for each scaffold group. Error bars

are one standard deviation.
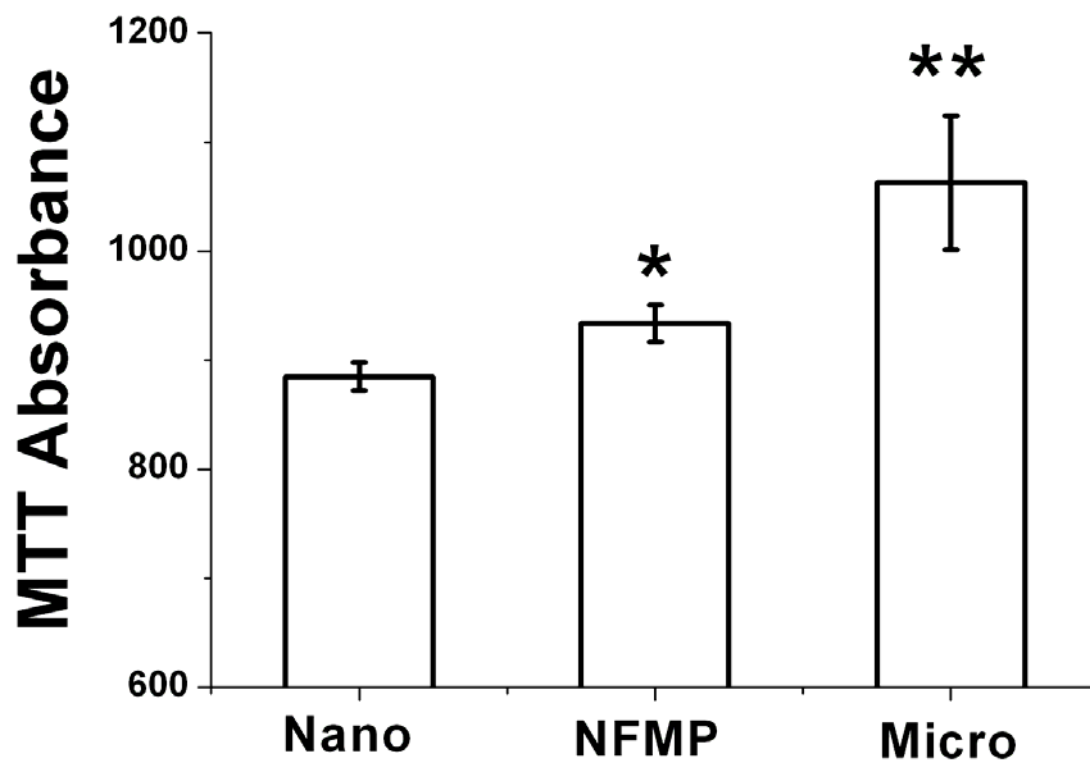
Figure 5.4. MTT assays of human NS cell population after 7 day in culture in NFMP, on Nano

and in Micro scaffolds. * indicates $P < 0.0001$. ** indicates $P < 0.000001$. n = 8 for each groups.

Error bars are one standard deviation.
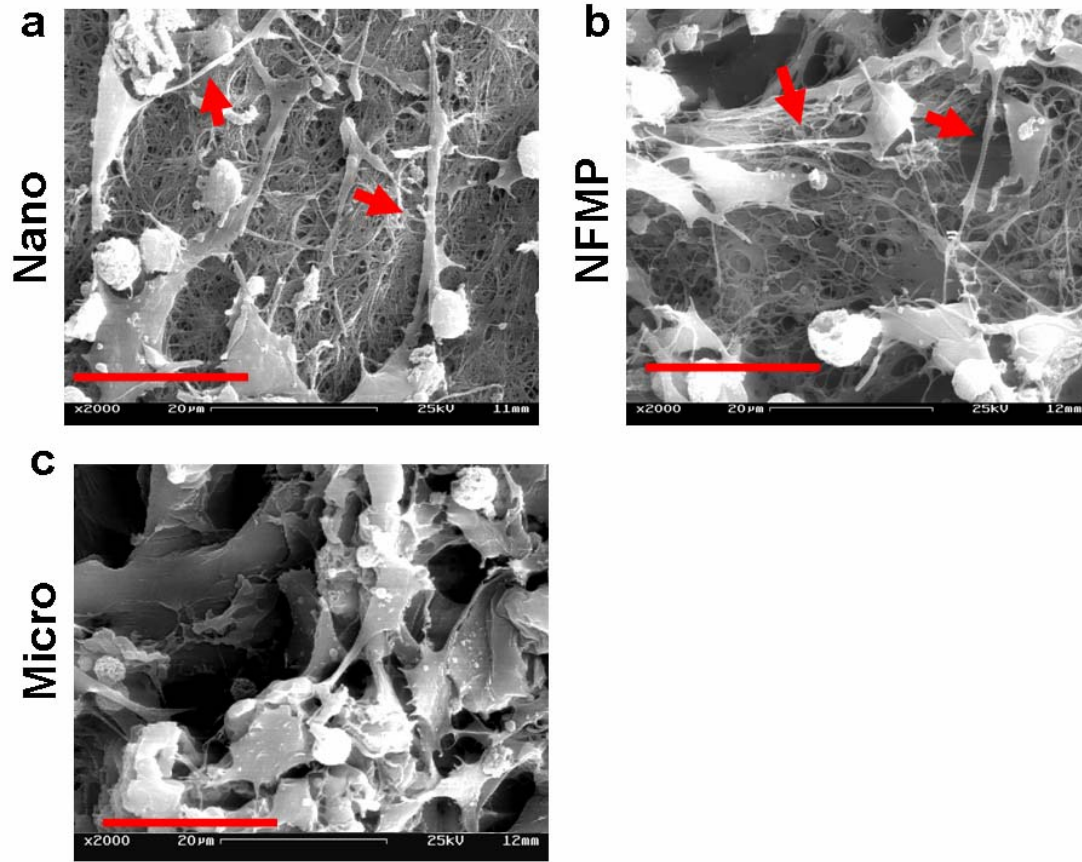
Figure 5.5. Human NS cell morphology on in Micro, on Nano and in NFMP scaffolds. The NS cells were cultured in growth media for 3 days and then changed into differentiation media. After one week into differentiation, SEM images showed that the NS cells on Nano (a) and in NFMP scaffolds (b) developed long and well-defined neurites (red arrows), whilst cells in Micro scaffolds did not show very long neurites (c). Bars represent 20 μm.
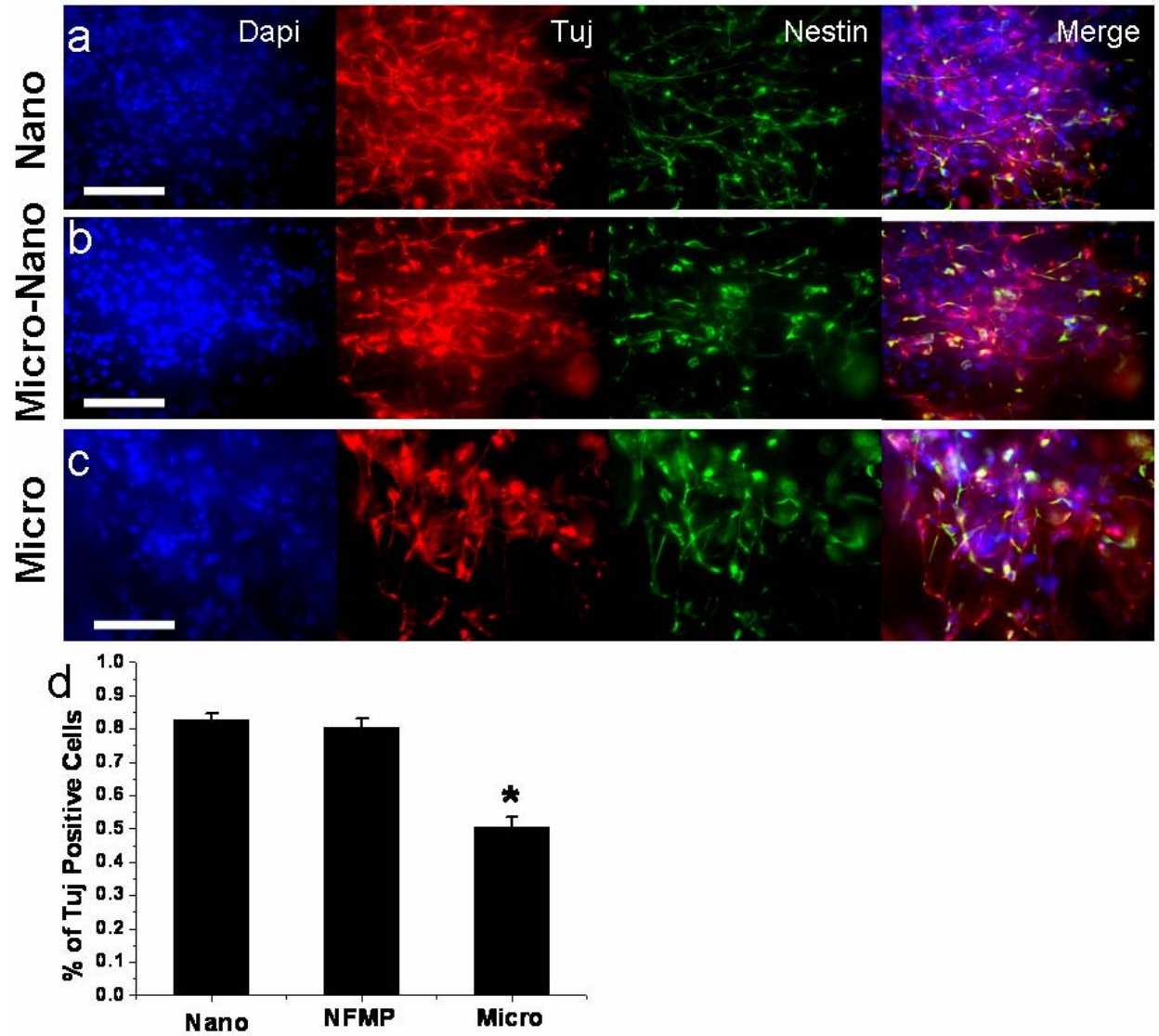
Figure 5.6. Immuno-fluorescence images of NS cells in differentiation assay.   Differentiating

neural stem cells cultured for 14 days in differentiation media on (a) Nano scaffold in , (b)

Micro-Nano (NFMP) scaffold and (c) Micro scaffold were examined with Dapi (cell nuclei in

blue), b-Tubulin+ (Tuj) (neurons in red), and Nestin+ (neural progenitors in green). (d): The

percentages of b-Tubulin+ cells in Micro, on Nano and in NFMP scaffolds. * indicates $P < 0.001$

compared to the other two groups. n = 101-118 for each scaffold group. Bars represent 100 μm.
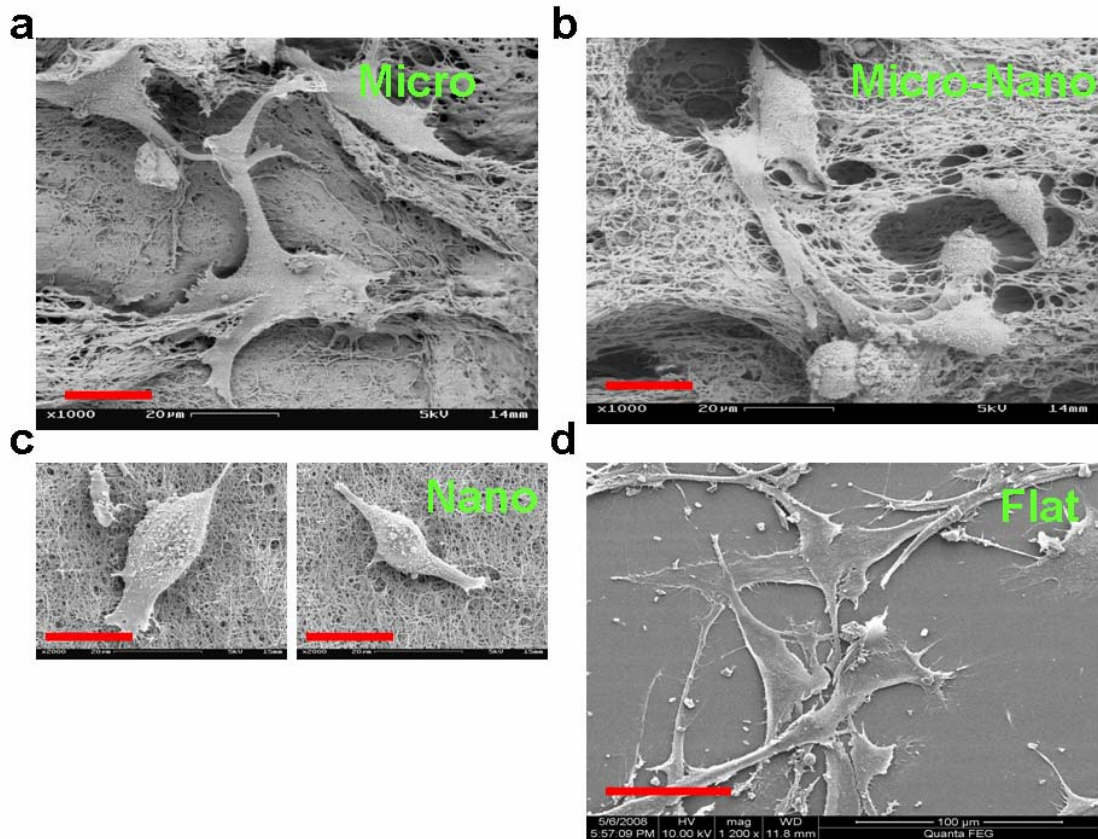
Figure 7. Human fibroblast cell morphology in Micro, on Nano in NFMP scaffolds. SEM micrographs showed that cells cultured on the Nano (c) and in NFMP (b) scaffolds had significantly smaller areas and perimeters than cells cultured in Micro scaffold and on flat controls (a and d). The results also showed that the cells had a more rounded cell body on nanofiber structures. Bars represent 20 µm in (a), (b), and (c) and 50 µm in (d).
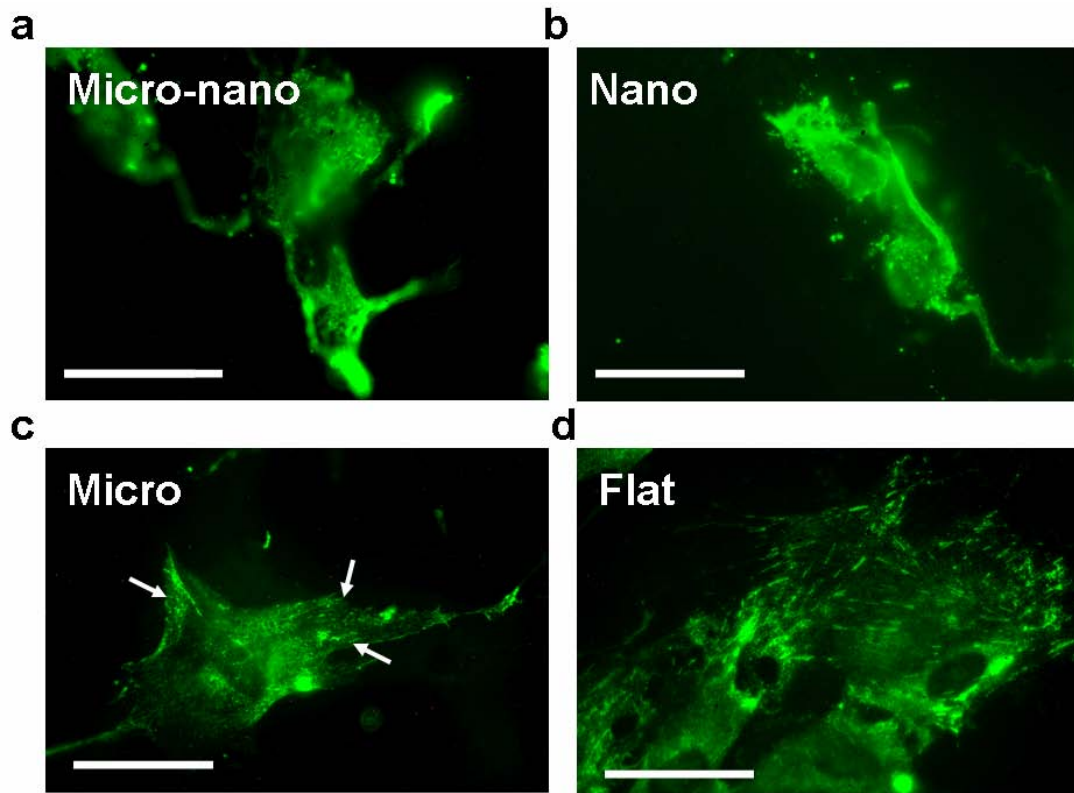
Figure 8. Immuno-fluorescence images of fibroblast cells stained for FAK PY397. We utilized

an antibody specific for FAK PY397 to examine its distribution in fibroblasts, 2 days in culture.

As observed in (d), cells cultured on glass demonstrated a streaky pattern of labeling. The

localization of FAK PY397 for cells on Nano (b) and in NFMP scaffolds (a) was more punctate

and less well defined. The observations made from Micro scaffolds (c) showed that the labeling

of FAK PY397 was streaky-like at the peripheral of the cell (white arrows). However, these

streaky patterns were not as well-defined as those from cells on flat controls. Bars represent 100

µm.

CHAPTER 6

CONCLUSIONSAND RECOMMENDATIONS

6.1 Conclusions

The overall objective in this study is to establish the potential of 3-D polymer scaffolds for high throughput cell-based assay applications. The scope of this study includes designing a process to feasibly integrate 3-D polymer scaffolds with traditional cell culture vessels, understanding how the cells behave on the scaffold in particular the extent to which they emulate the *in vivo* responses, and optimizing the scaffold structures by incorporating nano-texture.

This study demonstrated a technology for integrating 3D synthetic polymer scaffolds with standard cell culture dishes and multi-well plates. This technology created a ready-to-use, robust and highly compatible 3D cell-based assay platform for HTS cell-based drug discovery programs. The large-scale production and quality control of these novel 3D vessels can be achieved with the standard laboratory automation workstation (liquid handlers such as Beckman Coulter's Biomek®). Following studies showed that the 3D scaffolds created a proper in vivo-like and biomimetic milieu for NS cells to attach, proliferate and develop in vivo-like functionalities (e.g. VGCC funtionality). Compared to cells cultured on standard 2D substrates, cells on 3D scaffolds more closely emulated in vivo surrogates such as neural spheres, with respect to proliferation, morphogenesis, cell-matrix adhesion, and calcium channel activity (Chapter 3).

To further confirm the physiological relevance of 3-D cell cultures with polymer scaffolds, mouse sympathetic neurons in vitro (3-D and 2-D) were investigated with respect to how well they modeled *in vivo* VGCC functionality. A more solid *in vivo* surrogate, freshly dissected SCG tissues, was used. Cell morphology and VGCC function from cells on 3-D scaffolds more closely modeled intact SCG tissues in comparison to cells on 2-D cover slips. Intracellular calcium increase in response to high potassium depolarization was identical between 3-D cultured and intact SCG tissue cells, but significantly different between 3-D and 2-D cultured cells. This result provides the evidence in support of the hypothesis that some cellular responses under traditional 2-D environment may be exaggerated [1]. Given that many drugs achieve their efficacy by interacting with membrane-integrated ion channels or their associated receptor-ligand behavior, this result brings attention to the potential importance of introducing three dimensional cell-based assays in drug discovery programs. (Chapter 4)

To best mimic the architecture of the natural extracellular matrix (ECM), a nano-fibrous/micro-porous combination (NFMP) scaffold has been created by a technique combining phase separation and particulate leaching. The NFMP scaffold inherited advantages from the nano-fibrous scaffold and the micro-porous scaffold and was indeed superior to both of them. The NFMP scaffolds were able to accommodate a large cell population, promoted cell differentiation, and induced a more "3-D" morphogenesis and cell-matrix adhesion. To the best of our knowledge, this is the first study to systematically compare micro, nano and micro/nano combination scaffolds and demonstrate the advantages of a micro/nano combination scaffold. These new synthetic extracellular matrices may provide better environment for cell distribution,

adhesion, growth, and differentiated function better emulating the *in vivo* conditions. The

architectural design at several size scales gives these novel scaffolds the potential to be tailored

for a variety of 3-D cell culture and tissue engineering applications. (Chapter 5)

Overall, the influences of this study on a better 3-D cell culture and cell-based assay

system is broad. With the technology developed in our lab (Chapter 3), synthetic polymer

scaffolds can be feasibly adapted to most of the current high throughput cell-based screening

systems. The 3-D assay plates created with this technology exhibit advantages to currently

available 3-D cell culture/assay products, such as PuraMatrix™ (self assembling nano-fiber

scaffolds/hydrogel), AlgiMatrix™ (micro-porous alginate scaffolds) and UltraWeb™ (synthetic

nano-fiber scaffolds). A detailed comparison is shown in the conclusion part of Chapter 3.

Moreover, the cost to manufacture these 3-D assay plates is relatively low so they should be

affordable in a typical HTS facility.

6.2 Recommendations

Although 3-D cell culture systems are known to reflect the *in vivo* behavior of many cell

types and are promising approaches for advanced drug screening, providing an appropriate

environment to culture cells in 3-D is no easy matter. The bio/pharmaceutical industry is

reluctant to accept 3-D cell culture/cell-based assay as a standard protocol. A major reason that

the 3-D culture systems have not entered the drug screening process to date is the lack of strong

evidence of efficacy, as well as the lack of simple, controlled techniques and protocols for rapid, standardized 3-D cell-based assay systems in situ.

In follow-up studies, similar to those previously conducted with cancer drugs [2], one can demonstrate whether these 3-D assay plates are able to improve clinical efficacy prediction in the early stage of drug discovery programs. It is well known that many drug candidates failed in the clinical trials either due to lack of efficacy or high toxicity. However, these candidates were considered viable hits when initially tested with a 2D cell-based system. In this manner, detecting false positive candidates in the early stage means lowering the cost of bringing drugs to market. Thus, a very interesting study will be testing some of these failed drugs in our 3-D assay plates to see whether they will fail because of efficacy or toxicity issues. Such results will definitely capture the attention of bio/pharmaceutical HTS laboratories. The ultimate goal of this study is to provide the pre-clinical trial facilities a better cell-based assay platform with high clinical predictability and physiological relevance. The concepts of this "3-D cell-based assay" platform are demonstrated in Figure 6.1.

Another important application of this technology will be creating combinatorial scaffold libraries for screening tissue regeneration biomaterials. Despite huge investment in tissue engineering research, very few profitable products have come to market [3]. It is well know that combinatorial methods have been proven useful for accelerating researches in the pharmaceutical industry as well as for characterizing biomaterials for tissue engineering applications [3]. However, most of these combinatorial libraries study the cell-biomaterial interaction on 2-D (flat) surfaces. Since it may be preferable to characterize cell-material interactions in a system where

the cells are exposed to the test materials in a 3D scaffold format, this technology can be applied

to fabricating combinatorial libraries of polymer scaffolds. The scaffold libraries can be

integrated with cells and tested for tissue formation performances (Figure 6.2).

6.3 References

1. Cukierman E, Pankov R, Stevens DR, Yamada KM. Taking cell-matrix adhesions to the

    third dimension. Science. 2001;294:1708-383.

2. Weaver VM, Petersen OW, Wang F, Larabell CA, Briand P, Damsky C, Bissell MJ.

    Reversion of the malignant phenotype of human breast cells in three-dimensional culture

    and in vivo by integrin blocking antibodies. Journal of Cell Biology.1997;137:231-245.

3. Simon Jr CG, Stephens JS, Dorsey SM, Becker ML. Fabrication of combinatorial

    polymer scaffold libraries. Review of Scientific Instruments. 2007;78,

    0722071-0722077.
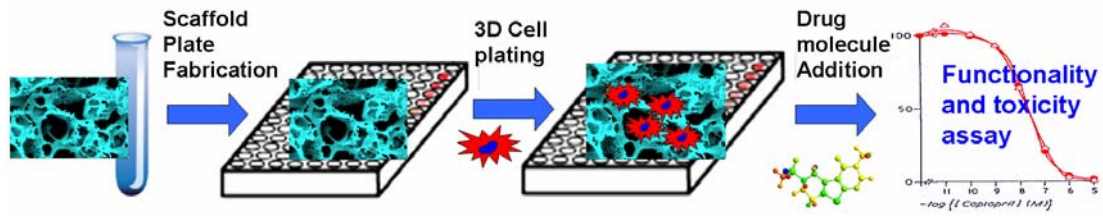
Figure 6.1. 3-D cell-based assay system for high throughout drug testing.
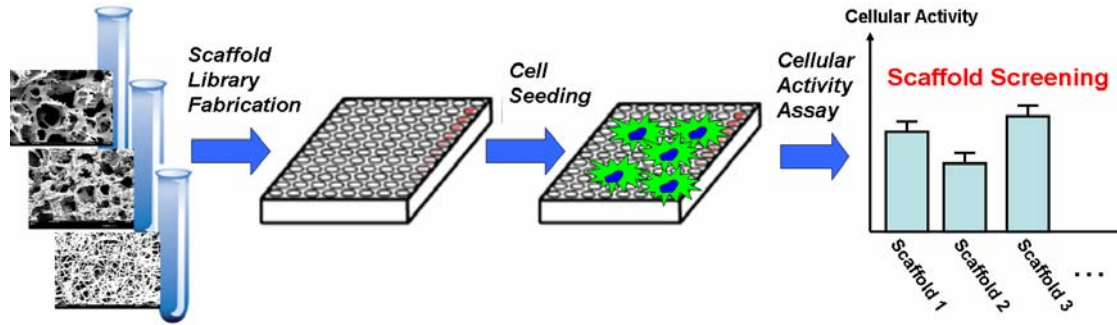
Figure 6.2. High throughput screening of biomaterials.

CHAPTER 7

APPENDIX

7.1 Protocols

7.1.1 Dissection and culture of mouse superior cervical ganglion (SCG) cells

Materials:

- Neonatal mice CD1 (Charles River Breeding Laboratories, Wilmington, Mass.)

- Dissection microscopy

- Dissection forceps and scissors

- Dissection plates

- PBS

- 70% ethanol

Dissection procedure:

1. Sacrifice the pups with CO_2.

2. Rinse the pups with 70% ethanol and then PBS.

3. Fix the pup on a dissection plate.

4. Cut the pup body (entering through the underarm region) with a pair of scissors.

5. Use a pair of scissors to cut the skin open along the midline from the midthorax to mandible

   level and from the lower cervical level to the two upper limbs. At this point, two large

salivary glands should be clearly seen along the midline of the neck under a dissection microscopy.

6. Use a pair of forceps to remove of one of the salivary glands. This should expose the strap muscles covering the vessels beneath.

7. Dissect the strap muscles to expose the carotid artery. At a higher magnification, one should find the nodose ganglion located at the bifurcation of the carotid artery. Do not confuse it with SCG. The SCG sits directly beneath the carotid artery.

8. Use one pair of forceps to lift the tail of ganglion and the carotid artery together and then use another pair of forceps to separate the ganglion and the artery from surrounding tissues.

9. Transfer the ganglion and the artery into a Petri dish with PBS.

10. Under higher magnification, remove the carotid artery from the ganglion with a pair of forceps.

11. Use two pairs of fine-tip forceps to clean the SCG free of blood vessels and covering connective tissues.

12. Store the cleaned ganglion into PBS for following procedures.

13. Repeat the entire procedure on the other side of the animal to obtain the second SCG.

Cell Culture Media:

- Eagle's Minimum Essential Medium with

- 2 mM L-Glutamine

- 1 mM Sodium Bicarbonate

- 10% (v/v) FBS

- 50 ng/ml NGF.

- 0.24μg/ml Ara-C

Cell culture procedure:

1. Before cell plating, all the samples are coated with 0.1 mg/ml type I collagen from rat tail at room temperature for 1 hour.

2. Transfer the PBS containing cleaned ganglions to a 15 ml centrifuge tube and allow the ganglions and any fragment to settle to the bottom.

3. Carefully aspirate the PBS

4. Add 1-2 ml of 1 mg/ml type I A collagenase.

5. Incubate the capped tube for 1 hour at 37.

6. Carefully aspirate the collagenase solution.

7. Rinsed the ganglions twice with complete growth media

8. Triturate the ganglions into single cell suspension with a Pasteur pipette whose tip has been fire polished to obtain a narrow opening. The diameter of the opening should be slightly smaller than that of the ganglions so that the ganglion are squeezed through it and dissociated sufficiently.

9. Plate the cell suspension onto samples.

10. Perform media change every other day.

Reference:

1. Mains RE, Patterson PH. Primary Cultures of dissociated sympathetic neurons: I. Establishment of long-term growth in culture and studies of differentiated properties. The Journal of Cell Biology. 1973;59:329-345.

7.1.2 Measurement of Calcium Influx from Individual Cells

Materials:

- HEPES Buffered Saline (HBS)

- Dimethyl Sulphoxide (DMSO)

- Pluronic F-127

- Fetal Bovine Serum (FBS)

- Calcium-Green-1, Acetoxymethyl (AM) Ester

Procedure:

Stock Preparation:

1. Prepare dye stock. Dissolve Calcium Green-AM in DMSO to obtain a stock solution of 1 mM. Add 39 µl DMSO to 50 µg calcium green AM vial to make 1 mM dye stock.

2. Prepare Pluronic F-127 stock. Weigh 0.2 g Pluronic F-127 in a 1.5 ml microcentrifuge tube and add 1 ml DMSO to make 20% (w/v) stock.

3. Prepare high potassium buffer stock. Dissolve 0.738 g of KCl to 20 ml HBS to get 495 mM potassium buffer.

4. Prepare dye solution for monolayer cell cultures. Mix 5 µl of Calcium Green stock with 1 µl

   pluronic F-127 stock in a 1.5 ml microcentrifuge tube. Then, add 30 µl of FBS and 964 µl of

   HBS. The final concentrations are 5 µM Calcium Green, 0.02% Pluronic F-127, and 3% FBS.

   For cells on scaffolds and cells in the intact SCG tissue, increase the dye concentration to 10

   µM.

5. Incubate the cells in dye solution at 37^0C for 30-60 min.

6. Wash the cells with HBS three times.

7. Incubate with 1 ml HBS for 30-60 min for de-esterification.

8. The fluorescent intensity is measured by a confocal imaging system (PCM-2000, Nikon)

   linked to an inverted (TE300, Nikon) mircroscope and a 60X Apochromat, oil-immersion,

   high numerical aperture (1.40) objective lens.

9. Calcium Green-1 has excitation/emission pak at 510/550 nm.   It can be excited with 488 nm

   argon laser and the emission can be visualized through the green channel.

10. Mount the petri dish on the microscope stage. Find a field of view with cells using the

    bright-field light path. Switch to confocal light path.

11. Select small pinhole setting and with 100% ND filter, fast scan and set black and gain level.

    Make sure the fluorescent intensity in the cells does not exceed one third of the saturation

    level.

12. Capture images with a continuous time scan mode. Add 100 µl high potassium buffer into the

    petri dish during the time scan. Capture and save change in calcium levels as change in grey

    levels.

13. Set ROI for the saved images and measure the grey level. Plot the grey level against time.

Reference:

1. Mao C and Kisaalita WS. Characterization of 3-D collagen hydrogels for functional cell-based biosensing. Biosensors and Bioelectronics.2004;9:1075-1088.

7.1.3 Calcium assay with 96-well plates

Materials:

- Neurobasal Media

- Invitrogen F36206 Fluo-4 no-wash Calcium Assay Kit

  The kit includes:

  Fluo-4 no-wash dye mix (Component A)

  Probenecid, water soluble (Component B)

  Assay buffer (1X HBSS, 20 mM HEPES) (Component C)

Procedure:

1. Add 10 mL of neurobasal media and 100 μL of the probenecid stock solution to one bottle of Component A. This 1X dye loading solution is sufficient for one microplate, and the pro-benecid concentration is 2.5 mM.

2. Shake or vortex the dye loading solution vigorously for 1-2 minutes to ensure that the dye dissolves completely.

3. Remove the growth medium from the adherent cell cultures. It is very important to remove

the growth medium in order to eliminate sources of baseline fluorescence, particularly

esterase activity. Quickly but carefully add 100 µL of the dye loading solution to each well of

the 96-well plate.

4. Incubate the plate(s) for 30-45 minutes at 37°C. The plates are now ready to be used in an

experiment.

5. Measure fluorescence with the Flexstation® with settings appropriate for excitation at 494

nm and emission at 516 nm.

7.1.4 Staining for Neural Differentiation Markers

Materials:

Pre-made solutions:

1. High Salt Buffer

Reagent	Vendor	Catalog Number	Amount per 50 ml	Final Concentration
Sodium Chloride	Sigma	S7653	14.61 g	250 mM
1M Tris (pH 7.4)	Sigma	T-3253	50 ml	50 mM

2. Blocking Solution

Reagent	Amount
High salt buffer	9.4 ml
6% serum from the animal that your secondary antibody is produced in.	600 μl

3. Permeabilization Buffer

Reagent	Vendor	Catalog Number	Amount per 50 ml
High Salt Buffer			50 ml
Tween 20	EMD Chemicals	9480	25 μl

4. Other Pre-made solutions and reagents needed

Reagent	Vendor	Catalog Number
PBS (with Ca^{++} and Mg^{++})	HyClone	SH30264.02
DAPI	VWR	80051-386
Prolong Gold	Invitrogen	P36930

Procedure:

1. Carefully remove spent media with a pipetteman or transfer pipette being careful not to dislodge cells.

2. Wash cells 1 time in PBS with Ca^{++} and Mg^{++} (PBS++).

3. Working in a fume hood, add 2% paraformaldehyde solution to just more than cover the bottom of slide wells.

4. Keep at room temperature for 15-20 min.

5. Wash wells 2 times with PBS++.

6. Wash with Permeablization Buffer 3 times for 5 minutes each.

7. Add enough Blocking Solution to completely cover the cells in each well (we recommend 250 µl/well).

8. Incubate at room temperature for 45 minutes.

9. Prepare primary antibody (1° Ab) in 1 ml of Blocking Solution at the recommended dilution (Nestin: 1:200; Tuj: 1:1000).

10. Aspirate Blocking Solution out of slide wells.

11. Add enough 1° Ab solution to completely cover the cells in each well.

12. Cover and incubate 1 hour at room temperature. This can be extended to over night at 4°C if necessary.

13. Wash wells 4 times with High Salt Buffer for 5 minutes each wash.

14. Prepare secondary antibody (2° Ab) in 1 ml of Blocking Solution at recommended dilution (Alexa Fluor® 488: 1:1000; Texas Red®: 1:250).

15. Aspirate off last wash.

16. Add enough 2° Ab solution to completely cover the cells in each well.

17. Incubate for 1 hour at room temperature. During incubation, cover sample with foil to

    prevent fluorescence bleaching

18. Wash cells 3 times with PBS++.

19. While completing washes, prepare DAPI solution at a 1:5000 dilution in PBS++.

20. Add enough DAPI solution to completely cover the cells in each well.

21. Incubate for 5 minutes at room temperature. Cover with foil during incubation.

22. Wash cells 3 times in PBS++.

23. Aspirate off PBS++.

24. Tilt slide to one side and allow excess surrounding PBS++ to run off onto paper towel.

25. Place one drop of mounting media (Invitrogen's Prolong Gold) directly in center of each well

    area.

26. At an angle gently lower a cover slip onto the slide trying to avoid air bubbles where

    possible.

27. Remove excess mounting media from slide and cure in the dark for 24 hours.

28. Seal with nail varnish on all four sides.

29. Keep in dark storage until results are observed and documented

Note: The staining procedure for scaffold samples is the same as that of cover slip samples until

Step 23. From Step 24, the procedure is:

24. Place a scaffold into the well of a MatTek® glass bottom Petri dish (Figure 7.1).

25. Place drops of mounting media directly onto the scaffold and make sure the mounting media fill the entire well area

26. Gently lower a cover slip onto the center of the dish trying to avoid air bubbles where possible.

27. Remove excess mounting media and cure in the dark for 24 hours.

28. Seal with nail varnish on all four sides.

29. Keep in dark storage until results are observed and documented

    Figure demonstrates the outlook of a "scaffold slide" for microscopy observation. One can observe the cells in the scaffold with a microscopy from either side of the dish.
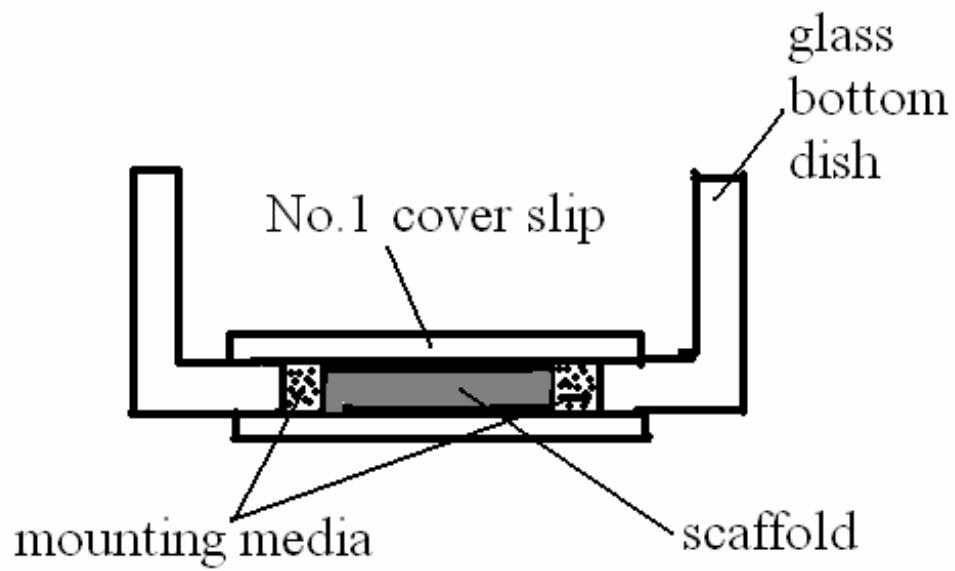
Figure 7.1. A "scaffold slide" for microscopy observation.

7.2 Raw Data

7.2.1 Figure 3.3 m. Total area covered by cells (a.u.)

Field	2D Day 0	2D Day 5	2D Day 10	3D Day 0	3D Day 5	3D Day 10
1	21512.83	55124.98	109746.81	14906.03	25269.32	39713.91
2	22409.81	52646.68	84709.55	15637.34	19839.71	46174.54
3	22519.34	67340.93	136175.97	13241.11	24919.06	68005.65
4	22148.47	52997.24	83526.88	14521.43	25333.86	53211.42
5	22144.46	68675.38	121563.22	13987.76	20320.93	61701.11
6	22984.58	67324.78	132998.11	15442.99	21015.58	32964.03
7	23124.97	52110.04	90462.82	13344.89	19519.38	33736.30
8	21647.23	67340.93	107533.37	15903.23	21594.77	51061.61
9	23296.80	61356.91	113847.47	14556.87	21305.05	61062.18
10	17298.56	59180.34	97433.87	13987.55	21114.95	40755.21
11	22345.23	60389.12	113346.10	14642.01	20405.78	42505.59
12	22148.47	60407.94	98765.55	15111.91	20105.74	51006.63
13	22144.46	59184.11	85826.74	14504.32	22277.07	54980.86
14	22984.58	58180.34	104567.87	13865.73	20239.42	50496.76
15	23124.97	62738.76	132341.77	15274.03	21296.08	56817.71
16	22647.23	53145.78	82341.99	14528.91	18736.99	59482.86

7.2.2 Figure 3.3 n. Neural sphere volume (a.u.)

Neural Sphere	Volume Day 0	Volume Day 5	Volume Day 10
1	367394.61	490421.72	911863.89
2	414409.28	623230.45	777297.09
3	319073.47	425310.05	883602.16
4	434929.08	510059.36	857295.60
5	243647.04	431384.86	798919.22
6	444483.05	602194.15	802999.76
7	334041.83	512434.06	913017.03
8	325582.90	411673.47	848774.95
9	456273.10	621398.25	812186.25
10	417203.25	500322.68	780175.61
11	337525.26	551596.18	920280.57
12	413463.66	413236.25	913103.04
13	423402.40	598239.87	852121.83
14	337329.31	611661.72	852063.24
15	351160.04	498763.10	820172.16
16	373564.10	501345.09	889335.26
17	356723.46	498232.71	792836.78
18	323847.34	523719.83	883246.29
19	378163.98	601837.44	872192.01
20	356721.87	451345.66	878176.26

7.2.3 Figure 3.5 h,i,j. Gene expression levels of VEGF, IL-8, and PKT2.

(Four biological replicates for each condition)

Sample	VEGF MEAN	SD
	VEGF	
Sample	**MEAN**	**SD**
2-D	6.27	3.44
3-D	11.85	1.59
Sphere	16.38	3.72
	IL-8	
Sample	**MEAN**	**SD**
2-D	3.37	1.84
3-D	7.14	2.18
Sphere	6.68	0.49
	PKT2(FAK)	
Sample	**MEAN**	**SD**
2-D	1274.648	34.84
3-D	1004.56	30.98
Sphere	1070.646	10.35

7.2.4 Table 4.1. Neurite Length (μm)

Cell	2D Day 2	2D Day 7	3D Day 2	3D Day 7
1	37.9711	37.14329	12.62321	52.01974
2	82.2704	45.49743	13.99106	30.59761
3	67.98217	21.02269	13.48377	17.8701
4	62.78413	30.62876	6.68522	11.6357
5	22.75155	21.2278	8.83021	8.74259
6	45.18768	17.14462	9.84486	10.57143
7	26.21591	93.17143	16.55508	6.96745
8	31.94678	149.2569	10.32628	22.18829
9	38.12951	53.14291	12.36891	13.21194
10	30.16516	92.35834	7.94321	6.26285
11	33.32939	87.5401	6.79869	9.96823
12	25.48157	53.50878		24.19386
13	44.078	101.6309		15.70335
14	30.10222	23.91652		17.48009
15	20.65094	66.52243		54.04182
16	20.55459	61.05516		10.34674
17	23.10072	64.43603		12.38158
18	11.29615	72.74746		21.05845
19	38.65871	125.0743		9.19974
20	16.3312	53.03347		19.59967
21	46.34934	46.02118		18.49123
22	37.3111	36.30938		48.38862
23	20.52319	45.62132		86.45962
24	24.98199	70.48264		27.93031
25	39.58386	65.06691		13.16876
26	27.7352	94.93633		29.8071
27	14.24036	48.16185		33.55528
28	45.72068	48.30358		17.35164
29	62.20647	42.20164		24.75724
30	43.60362	212.941		20.24515
31	20.06813	133.9009		19.13084
32	55.76659	100.6774		18.98987
33	53.38463	59.93227		10.87502
34	32.51722	48.9804		17.29375
35	33.07034	80.04318		40.73865
36	40.84665	64.85018		23.06743
37	41.27344	39.53654		31.25732

38	43.3328	41.5766		24.65034
39	29.2741	35.35102		46.32648
40	42.58891	34.78178		31.64314
41	22.41705	73.3653		32.75374
42	61.01741	78.94808		32.93307
43	27.67174	102.5582		31.27443
44	16.67406	90.75484		17.53503
45	35.65778	101.4178		26.57352
46	42.74292	35.66186		34.58015
47	27.91962	27.28094		32.65897
48	22.47836	85.81284		35.39411
49	6.52373	55.72229		25.1178
50	35.1401	21.40166		20.15657
51	41.17125	68.64077		27.7471
52	3.64984	65.95039		26.16782
53	33.50353	90.09548		35.89011
54	27.19423	64.44574		21.32616
55	63.76429	47.33342		13.9591
56	22.49285	23.84407		27.26263
57	37.84308	45.89917		13.18807
58	14.93294	170.6509		29.86382
59	28.57582	32.98071		44.84209
60	20.49882	48.50189		23.09727
61	29.85792	26.71126		
62	22.99173	29.25259		
63	52.54635	123.9688		
64	33.69134	49.08196		
65	54.69393	66.76236		
66	40.9376	50.33241		
67	32.24027	53.31864		
68	22.23677	24.10267		
69	47.56649	75.71216		
70	50.63887	31.51831		
71	33.88777	61.44525		
72	38.49243	115.5387		
73	49.53639	32.22219		
74	33.10526	143.06		
75	18.1623	51.26556		
76	37.1088	69.0526		
77	21.52251	38.57935		

78	56.87618	85.68942		
79	21.36671	122.7038		
80	35.51216	51.62227		
81	58.81499	42.86679		
82	22.06808	56.38987		
83	29.37166	14.95865		
84	30.47835	41.44489		
85	28.66905	57.44798		
86	41.54283	58.44975		
87	118.2495	22.01941		
88	84.52742	51.68241		
89	66.68092			
90	69.80236			
91	55.19536			
92	44.11215			
93	59.41242			
94	39.4204			
95	62.56781			
96	49.40818			
97	69.52225			
98	69.40289			
99	42.10976			
100	34.68195			
101	48.26779			
102	30.62238			
103	50.80361			
104	61.41411			
105	59.64568			
106	64.84284			
107	63.64531			
108	56.40749			
109	32.56118			
110	26.80671			
111	28.78042			
112	49.85816			
113	41.55574			
114	45.62322			
115	17.71889			
116	26.80671			
117	51.28599			

118	39.46338			
119	19.08314			
120	20.79501			
121	11.83607			

7.2.5 Table 4.1.Cell Spread Area (μm^2)

Cell	2D Day 2	2D Day 7	3D Day 2	3D Day 7
1	201.5059	271.443	87.61663	267.4137
2	236.2483	200.6836	72.19841	92.63269
3	191.2271	123.3869	95.96303	139.0929
4	86.83544	239.2909	108.5032	121.619
5	160.3084	104.515	92.67381	90.37135
6	98.67664	123.4691	75.56986	97.93656
7	185.9644	92.71492	66.23669	236.9884
8	132.3912	74.41863	111.9569	143.7801
9	193.3651	131.2399	103.8572	220.2134
10	144.7669	62.61855	153.031	107.2697
11	363.459	55.54672	102.7882	107.0642
12	197.3944		139.3808	139.9564
13	93.37277		76.92666	105.2962
14	161.213		90.37135	153.9356
15	272.0186		86.25983	
16	183.2096		68.08688	
17	227.203		61.17952	
18	152.9077		64.96212	
19	163.022		77.8312	
20	182.0584		89.26124	
21	160.144		71.12941	
22	46.25467		77.37893	
23	161.0896		89.09678	
24	117.9597		106.4063	
25	136.7494		68.08688	
26	208.5777		104.3505	
27	55.71119			
28	135.1459			
29	140.4909			
30	188.5546			
31	204.9596			
32	107.4342			
33	112.6558			
34	165.5712			
35	104.0627			
36	100.2801			
37	145.7536			

38	209.6467			
39	130.2943			
40	123.8803			
41	164.3788			
42	141.601			
43	186.9922			
44	128.6497			
45	120.8378			
46	62.04294			
47	65.08547			
48	51.88747			
49	96.99091			
50	90.16578			

7.2.6 Table 4.1.Cell Body Roundness. Cell body roundness was investigated by confocal microscopy images taken with higher magnification (64X) oil lens and quantitative cell morphology measurements were processed by SimplePCI 2000 software. Roundness was an estimated circularity shape factor calculated as: 4*Pi*area/perimeter^2.

Cell	2D Day 2	2D Day 7	3D Day 2	3D Day 7
1	0.49853	0.2524	0.86566	0.56286
2	0.52092	0.55315	0.80525	0.73092
3	0.34082	0.63079	0.82661	0.54925
4	0.61296	0.47677	0.75602	0.83801
5	0.50371	0.49851	0.8155	0.62618
6	0.39823	0.53936	0.82187	0.7573
7	0.4477	0.54404	0.85381	0.77547
8	0.69103	0.64699	0.82123	0.42756
9	0.61528	0.53363	0.76226	0.43627
10	0.3937	0.55162	0.83244	0.73405
11	0.52198	0.67434	0.79288	0.60941
12	0.50648		0.76001	0.73565
13	0.59419		0.76601	0.81586
14	0.50186		0.86719	0.42697
15	0.73569		0.69266	
16	0.59392		0.81759	
17	0.48232		0.86469	
18	0.61169		0.64613	
19	0.43039		0.7921	
20	0.38464		0.84313	
21			0.79005	
22			0.83569	
23			0.84157	
24			0.86174	
25			0.84628	
26			0.83585	

7.2.7 Fig 4.4. VGCC Response Magnitudes of SCG Cells in 2-D, 3-D and SCG tissue.

Response Magnitudes (RM) = (Fmax-Fo)/Fo.

2D Day 2				2D Day 7			
Cell	Fmax	Fo	RM	Cell	Fmax	Fo	RM
1	52.31176	45.36807	0.153052	1	42.93825	30.64392	0.4012
2	72.7234	61.95479	0.173814	2	47.86815	33.51469	0.428274
3	55.48015	45.98246	0.20655	3	57.45479	38.10206	0.507918
4	70	57.54013	0.216542	4	64.55263	42.41813	0.521817
5	38.79866	31.84733	0.21827	5	53.62224	34.43025	0.557417
6	108.6495	88.34538	0.229826	6	54.51344	34.72312	0.569946
7	73.86258	59.83075	0.234525	7	81.75534	51.54751	0.586019
8	13.95238	10.95238	0.273913	8	38.78378	23.92919	0.620773
9	78.91737	55.92903	0.411027	9	59.23898	35.80077	0.654685
10	79.73541	54.06841	0.474713	10	40.32498	24.31151	0.658679
11	82.6121	55.84579	0.47929	11	59.63228	35.80238	0.665595
12	96.8892	64.69832	0.497554	12	40.63011	24.34261	0.669094
13	99.45158	65.22826	0.52467	13	51.55628	30.42814	0.694362
14	46.57105	29.6753	0.569354	14	82.10341	45.17727	0.817361
15	92.41426	57.71775	0.601141	15	57.85472	31.62923	0.829154
16	96.3125	59.33979	0.623068	16	50.72788	27.27163	0.860097
17	80.29765	48.55012	0.653912	17	34.62704	18.4281	0.879035
18	77.10227	45.71023	0.686762	18	91.43369	47.03846	0.943807
19	81.43879	46.37853	0.755959	19	63.41491	32.52796	0.949551
20	86.93967	48.95387	0.775951	20	59.55815	29.40329	1.025561
21	109.9918	60.96531	0.804171	21	46.14123	22.2488	1.073875
22	84.33152	46.3913	0.81783	22	65.18136	31.02877	1.100675
23	60.2989	32.28326	0.867807	23	61.13015	29.06066	1.103536
24	69.67836	36.68637	0.899298	24	70.29277	33.31641	1.109854
25	104.4594	54.36672	0.921386	25	48.8779	23.12567	1.113578
26	45.98581	23.31938	0.972	26	66.72091	31.18245	1.139694
27	92.90273	45.33581	1.049213	27	55.71912	25.01069	1.227812
28	68.34942	31.58494	1.163988	28	66.02351	22.80832	1.894712
29	94.877	43.78674	1.166798				
30	95.10339	42.60659	1.232129				
31	123.1731	51.79077	1.378282				
32	70.15198	21.85772	2.209483				
33	98.4922	27.69191	2.556714				

3D day 2				3D Day 7			
Cell	Fmax	Fo	RM	Cell	Fmax	Fo	RM
1	9.32542	8.09153	0.152492	1	21234.2	18415.08	0.153088
2	86.44344	74.84615	0.154948	2	27829.09	23992.66	0.1599
3	43.16505	36.95146	0.168155	3	28959.6	24797.19	0.167858
4	71.01818	60.52727	0.173325	4	5606.615	4593.093	0.220662
5	38.51111	32.80741	0.173854	5	15654.48	12771.57	0.225728
6	98.71895	82.56863	0.195599	6	29539.68	24017.15	0.229941
7	203.3088	168.8971	0.203744	7	37969.71	30635.84	0.239388
8	63.73377	52.88312	0.205182	8	33487.81	26744.5	0.252138
9	11.6553	9.55682	0.219579	9	22202.67	17632.81	0.259168
10	231.9485	190.165	0.219722	10	8349.52	6620.916	0.261082
11	48.77419	39.8172	0.224953	11	21284.37	16733.4	0.271969
12	211.8403	172.3333	0.229247	12	34860.29	26655.89	0.307789
13	60.16541	48.15789	0.249337	13	20302.31	14602.22	0.390358
14	74.38889	59.52381	0.249733	14	27458	19630.53	0.39874
15	102.7875	82	0.253506	15	35270.36	25076.99	0.406483
16	61.58333	47.45455	0.297733	16	29120.22	20208.99	0.440954
17	63.11111	47.92593	0.316847	17	25882.31	17577.14	0.472498
18	65.25694	49.31944	0.323148	18	44112.33	29747.59	0.482887
19	73.77976	54.94048	0.342903	19	35908.28	23838.24	0.506331
20	49.74272	36.84466	0.350066	20	32336.57	21192.95	0.525817
21	75.185	54.65	0.375755	21	18641.13	11820.27	0.577047
22	105.7273	76.83838	0.37597	22	13452.38	8216.277	0.637285
23	59.30769	41.73504	0.421053				

Intact SCG tissue (In vivo surrogate)			
Cell	Fmax	Fo	RM
1	9370.03	8136.43	0.151614
2	17386.05	15072.19	0.153518
3	11089.9	9608.028	0.154233
4	17849.13	15282.3	0.167961
5	23068.46	19416.57	0.188081
6	16137.95	13552.62	0.190762
7	16609.26	13759.03	0.207154
8	18712.38	15078.58	0.240991
9	10034.46	8005.849	0.253391
10	12416.26	9881.766	0.256482
11	16417.62	12936.66	0.269077
12	25177.43	19750.45	0.274778
13	18151.87	14169.37	0.281064
14	12780.91	9952.532	0.284187
15	13118.75	10083.91	0.300959
16	20786.54	15639.6	0.329097
17	22256.95	16544.71	0.345261
18	18556.07	13620.25	0.362389
19	17034.13	12394.77	0.3743
20	18392.93	13304.23	0.382487
21	10582.53	7424.444	0.425364
22	18203.67	12528.25	0.453009
23	16881.32	11610.95	0.453914
24	36806.96	24718.29	0.489058
25	14605.78	9774.489	0.494276

7.2.8 Figure 5.4. MTT result summary. Final Value = Reading Average – Background

Nano					
Sample	**Reading 1**	**Reading 2**	**Reading 3**	**Average**	**Background**	**Final Value**
1	951	964	954	956.3333	3	953.3333
2	935	957	949	947	4	943
3	911	926	920	919	3	915
4	964	971	964	966.3333	7	959.3333
5	935	947	939	940.3333	4	936.3333
6	923	939	926	929.3333	8.33	921
7	918	940	930	929.3333	2	927.3333
8	903	928	920	917	2	915
NFMP						
Sample	**Reading 1**	**Reading 2**	**Reading 3**	**Average**	**Background**	**Final Value**
1	914	908	900	907.3333	7	900.3333
2	894	890	894	892.6667	5	887.6667
3	910	903	897	903.3333	12.33	891
4	884	879	873	878.6667	5.33	873.3333
5	888	885	877	883.3333	5.33	878
6	871	867	864	867.3333	6	861.3333
7	909	907	898	904.6667	8.33	896.3333
8	904	902	892	899.3333	8	891.3333
Micro						
Sample	**Reading 1**	**Reading 2**	**Reading 3**	**Average**	**Background**	**Final Value**
1	1222	1314	1288	1274.667	128	1146.667
2	1146	1108	1159	1137.667	96.33	1041.333
3	1117	1079	1113	1103	118	985
4	1353	1270	1330	1317.667	182	1135.333
5	1202	1190	1220	1204	117	1086.667
6	1100	1094	1112	1102	83.33	1018.667
7	1084	1106	1099	1096.333	71.33	1025

7.2.9 Figure 5.6 d. Tuj+ and Dapi+ counts in Nano, Micro, and NFMP scaffolds

Sample 1	Nano	Micro	NFMP
Tuj+ counts	85	55	84
Dapi+ counts	101	111	105
Tuj+ percentage (%)	84.16	49.55	0.80
Sample 2	Nano	Micro	NFMP
Tuj+ counts	86	50	90
Dapi+ counts	107	103	108
Tuj+ percentage (%)	80.37	48.54	83.33
Sample 3	Nano	Micro	NFMP
Tuj+ counts	98	55	90
Dapi+ counts	118	102	115
Tuj+ percentage (%)	83.05	53.92	78.26